Reactivity and Characterization of Supported Noble Metal Catalysts

By

Keishla R. Rivera-Dones

A dissertation submitted in partial fulfillment of
the requirements for the degree of

Doctor of Philosophy
(Chemical & Biological Engineering)

at the
UNIVERSITY OF WISCONSIN-MADISON
2020

Date of final oral examination: July 27, 2020

The dissertation is approved by the following members of the Final Oral Committee:

James A. Dumesic, Professor, Chemical and Biological Engineering
George W. Huber, Professor, Chemical and Biological Engineering
Manos Mavrikakis, Professor, Chemical and Biological Engineering
Brian F. Pfleger, Professor, Chemical and Biological Engineering
Ive Hermans, Professor, Chemistry

Reactivity and Characterization of Supported Noble Metal Catalysts

Keishla R. Rivera Dones
Under the supervision of Prof. James A. Dumesic and Prof. George W. Huber at the University of Wisconsin - Madison

Abstract

Catalytically driven processes account for over ninety percent of industrial chemical manufacturing today. Developments in manufacturing processes are largely driven by continued improvements in catalytic materials, which aim to increase production volumes while minimizing costs along with safety and environmental hazards. In order to achieve these goals, however, a rational approach in catalyst design must be pursued that aims to understand and build upon the fundamental structural, electronic, and chemical properties governing catalytic performance. To that purpose, the work presented in this dissertation makes use of kinetic experiments, theoretical models, and advanced characterization techniques to generate a fundamental understanding of noble metal surfaces employed in a variety of catalytic reaction systems.

In Chapter 2, we discuss the use of N_2 physisorption, CO chemisorption, and NH_3 temperature programed desorption to evaluate the effect of support acidity on the reactivity profiles of various zeolite-supported Pt and Pt-Sn catalysts for the non-oxidative coupling of methane to ethylene and aromatics. Reactivity studies for Pt-Sn/H-ZSM-5 catalysts at 973 K showed that, while all catalysts produced ethylene as the primary product, increasing support acidity led to an increase in naphthalene selectivity at the expense of benzene selectivity. Volcano-shaped profiles observed for the generation of aromatic products suggest that the formation of a reactive hydrocarbon pool on acidic support surfaces could be responsible for the oligomerization of ethylene. Notably, the Pt-Sn/H-ZSM-5 (SiO_2:Al_2O_3 = 50) catalyst was found to be comparable to the state-of-the-art Mo/H-ZSM-5 catalysts in terms of carbon product generation and resistance to coke formation.

In Chapter 3, x-ray absorption spectroscopy (XAS) was used to highlight the effect of local electronic and structural environments in specially synthesized metallic catalysts. The local coordination and nearest-neighbor distance of Pd species were evaluated to understand metal dispersion and the effect of catalyst support on the extent of bimetallic particle formation in Pd, AgPd, CuPd, and AuPd catalysts synthesized by controlled surface reactions (CSR) for a variety of amination, hydrodechlorination, and hydrogenation reactions. Near-edge structure analyses were also used on these Pd catalysts, as well as on a set of Mo-containing multi-metallic catalysts prepared by atomic layer deposition (ALD) for synthesis gas conversion, to understand catalyst reducibility along with potential support and hydrogen spillover effects on the extent of metal reduction.

Chapter 4 evaluates the effects of catalyst support and pretreatment conditions on the hydrogenation of acetone over SiO_2-, Al_2O_3-, and ZSM-5-supported platinum catalysts. Pt/ZSM-5 catalysts were found to have specific conversion rates and turnover frequencies that were 2 – 3 orders of magnitude higher than those observed over Pt/SiO_2 and Pt/Al_2O_3 catalysts, regardless of zeolite acidity or pretreatment conditions. For Pt/ZSM-5 catalysts, the higher activity was achieved by increasing calcination and decreasing reduction temperatures, likely due to the effects of these treatments on the morphology of the platinum particles. CO-FTIR measurements showed a shift to higher frequencies of the Pt-CO band in Pt/ZSM-5 catalysts compared to Pt/SiO_2, which alluded to the interactions between Pt and the porous zeolite structure as a source of the activity enhancements observed.

Chapter 5 introduces the use of transient kinetics studies and theoretical modeling to explore the importance of surface coverage effects in the hydrogenation of acetone over platinum. Transient models based on steady-state microkinetics using static and dynamic inclusion of surface coverage via the Langmuir and Bragg-Williams approximations, respectively, predicted notable differences in the decay profiles of the most abundant reactive intermediate (MARI) from the catalytic surface. Experimental studies using steady-state isotopic transient kinetic analysis (SSITKA) methods served to validate the theoretical predictions for transients induced by complete acetone removal from or its substitution in the reactant feed and provided tangible evidence for the importance of surface coverage effects in understanding the reactivity of platinum catalysts for acetone hydrogenation. Lastly, Chapter 6 addresses possible future research directions in the field of transient kinetics studies.

Acknowledgements

I would like to express my deepest gratitude to my research advisors, without whom these last few years would not have been possible. To Prof. James Dumesic – I am indebted to your guidance and mentorship throughout this journey. Your commitment to excellence and the thirst for fundamental understanding of catalytic systems is unparalleled, as are your care and interest in the multi-faceted well-being of your students. To Prof. George Huber, thank you for your unwavering support towards the development of my professional career. Your continued partnership with academic and industrial entities has helped provide your students with insight into the applications of catalytic work and how the scientific community contributes to help solve real-word challenges.

I would also like to thank Prof. Thatcher Root, Prof. Ive Hermans, Prof. Brian Pfleger, and Prof. Manos Mavrikakis for their continued support throughout the various PhD milestones and their participation in my research committees. Thanks are in order to Prof. Jim Miller for providing research training and career guidance in the early stages of my PhD journey, and for always providing a welcoming and cheerful environment to those around him. I am also immensely grateful to Prof. Jeff Miller at Purdue University for his continuous support with the planning and execution of XAS experiments and associated data analysis. Additional thanks are in order to Kathy Heinzen and Kate Fanis for their guidance through graduate program logistics and their support in recruitment activities, and well as to the rest of the CBE department staff for their continuous support of research activities.

To Mrs. Judy Lewison – you truly are the behind-the-scenes queen of the Dumesic group. Words will always fall short to describe how incredibly grateful I am for all the administrative and culinary support you provided us 4th floor residents. Our main office conversations about anything and everything have helped us stay grounded with the facts of life while simultaneously allowing us to dream about moving the labs to Hawaii.

To Ms. Kelly Burton – thank you for every single thing you do. Your undevoted commitment to the GERS program and every one of its students is unmatched. Thank you for treating us all like family, for encouraging and facilitating our well-being in all aspects of our academic, career, and personal lives. Thank you for always keeping your door open for us, for providing a judgement-free safe space when the weight on our shoulders overwhelmed us, and for always speaking up and standing by our side.

The research life is nothing if not for the graduate students that sustain it, and I have had the pleasure of spending these past few years alongside many wonderful researchers. I would particularly like to thank Dr. Insoo Ro for his training in hydrogenation reactions and catalyst synthesis, as well as the numerous scientific and mentoring conversations we sustained throughout the years. I would also like to thank Dr. Joe Chada for his invaluable teachings regarding the XAS and SSITKA techniques and for establishing what will forever be known as the Argonne trip anthem. The road trip and long days working around the clock at the synchrotron were made so much better by the awesome company of Dr. Maddie Ball, Dr. Siddarth Krishna, Dr. Lifeng Zhang, Hochan, Elise, and Alvin. Every day at the lab was made better by the personal and professional interactions with these wonderful researchers as well as the rest of all current and previous 1st & 4th floor catalysis group members: Dr. Dan McClelland, Dr. Yifei Liu, Dr. Nat Eagan, Bengi, Jake, Saurabh, Peter, Mark, Anthony, Paolo, Kevin, Raka, Min Soo, Edgard, and everyone else I likely missed. It's been fun and enriching spending these years with you all.

To the wonderful friends I have made along the way, thank you for making these past years a truly memorable experience – I hope our friendships continue to thrive in the years to come.

Hector, Coogan, and Taylor, thanks for the amazingly fun times we have spent together, for introducing me to British baking shows, and for the fun summer trip to Nashville (when's the next one?!). Leida, ¡*mamisonga!*, you have been an invaluable lifeline these last few years and I am so grateful our paths crossed in this journey. I look forward to our next international destination and hope that one day we get to finish that painting. Emmanuel, you have been an unexpected blessing during tough times, and I want to thank you again for your support, openness, and honesty. To everyone else I bave met along the way, both in and out of Engineering Hall, thank you for helping make Madison feel like home.

To Ángel – We did it! While the journey has been nothing short of a rollercoaster ride, I am forever grateful that you have been a fundamental part of it. Thank you for your unwavering support throughout the brightest and darkest of days. You have lifted me up in more ways than I ever thought possible or even necessary, and I hope that I have at least been able to provide some fraction of that to you as well. I look forward to discovering what the future has in store for us.

To my family, words could never fully express the immense amount of gratitude I feel for all the love and support you have always provided. *A mis KACKs – ¡son las mejores! Gracias por todos estos años de apoyo y amistad, y todos los que están por venir.* To my Houstonians, thank you for always leaving your doors open for me and for always believing and trusting in my decisions. I admire the dedication and commitment you have always shown towards your family, and I truly appreciate having been welcomed into that circle time and time again. *A toda mi familia cialeña - gracias por siempre hacerme sentir como la niña consentida de la familia. Sus gestos de apoyo, la satisfacción en gustitos culinarios y los abrazos de oso siempre me han brindado gran paz y alegría. Los amo un mundo.* Finally, to my parents – I would not be where I am today if not for your sacrifice, your bravery, your persistence, and your commitment, not only to each other, but to my future as well. I still remember your shock when, after months of consideration, I finally told you of my decision to take on this challenge. More importantly, however, was how your short-lived apprehension turned ever so quickly into supporting words and actions of encouragement. I can only hope to have made you proud. *Sé que no se los digo lo suficiente, pero más fuerte no los podría amar. Ha sido un honor tenerlos de mi lado durante este recorrido y espero que sepan que sin ustedes, no hubiera sido posible. ¡Habemus doctora!*

Table of Contents

List of Figures

List of Tables

Chapter 1. Introduction

1.1 Industrial Impact of Catalytic Materials

Catalysts have been at the forefront of commodity and specialty chemical manufacturing processes since the late 18th century and today contribute to the production of over 90% of all industrial chemicals.[1] Catalytic processes such as the Haber-Bosch process for ammonia synthesis and the Fischer-Tropsch synthesis for hydrocarbon generation changed the history of the world's food and fuel production.[2,3] Since then, catalytic processes have continued to shape the way we generate fuels, food, medicine, plastics, clothing, and many other consumer and commodity products.

While necessary to sustain current ways of life, industrial manufacturing processes for fuel, plastic and other essential items often produce undesired byproducts that can pose health and environmental hazards. Improvements in catalytic materials can help mitigate such negative impacts by enabling reductions in the number and overall quantity of undesired byproducts. Besides providing safer pathways for chemical production, catalytic materials can also improve energy utilization, minimize greenhouse emissions, and facilitate chemical, fuel, and energy generation from renewable resources such as solar power and biomass feedstocks.

In general, process improvements are industrially achieved by designing catalysts that can increase production volumes while minimizing additional energy consumption, along with production or material costs. Economically, technological improvements at manufacturing sites generally give consumers the benefits of readily available and high-quality products at reasonable prices.[3] In developing processes, such benefits could be attained, for example, by operating at lower temperatures or pressures in smaller reactors that do not require exotic construction materials.[3] While achieving these and many other economic and processing improvements requires macroscopic studies of catalytic materials, an atomic or nanoscale level understanding of these materials and their role in the promotion of chemical reactions is ultimately at the heart of catalyst design and development.

1.2 Understanding the Performance of Catalytic Materials

While the activity findings obtained via reactivity studies are the chief motive behind the promotion and scaling up of catalytic systems for industrial applications, characterization studies are indispensable for the fundamental understanding of catalytic performance. The large variety of characterization techniques currently available, along with those continuously under development, allows for the potential to develop detailed narratives explaining the driving force behind catalyst activity, selectivity, and lifetime.[2] Characterization techniques range from rudimentary molecular adsorption methods for which experimental setups can be easily assembled in-house to sophisticated imaging and spectroscopic methods requiring expensive and specialized equipment that is sometimes available only at national research laboratories or private sectors. Due to the large number of techniques used in the characterization of catalytic materials, this chapter introduces only a select subset of the more commonly used methods, with special attention to those implemented in the various studies performed and discussed within this dissertation.

In general, the characterization techniques employed for heterogeneous catalysts focus on the physical and chemical properties of the catalytic surface under study in an attempt to link synthesis outcomes with reactivity performance. A compilation of the synthesis and characterization methods employed within this dissertation is shown below in Figure 1.1.

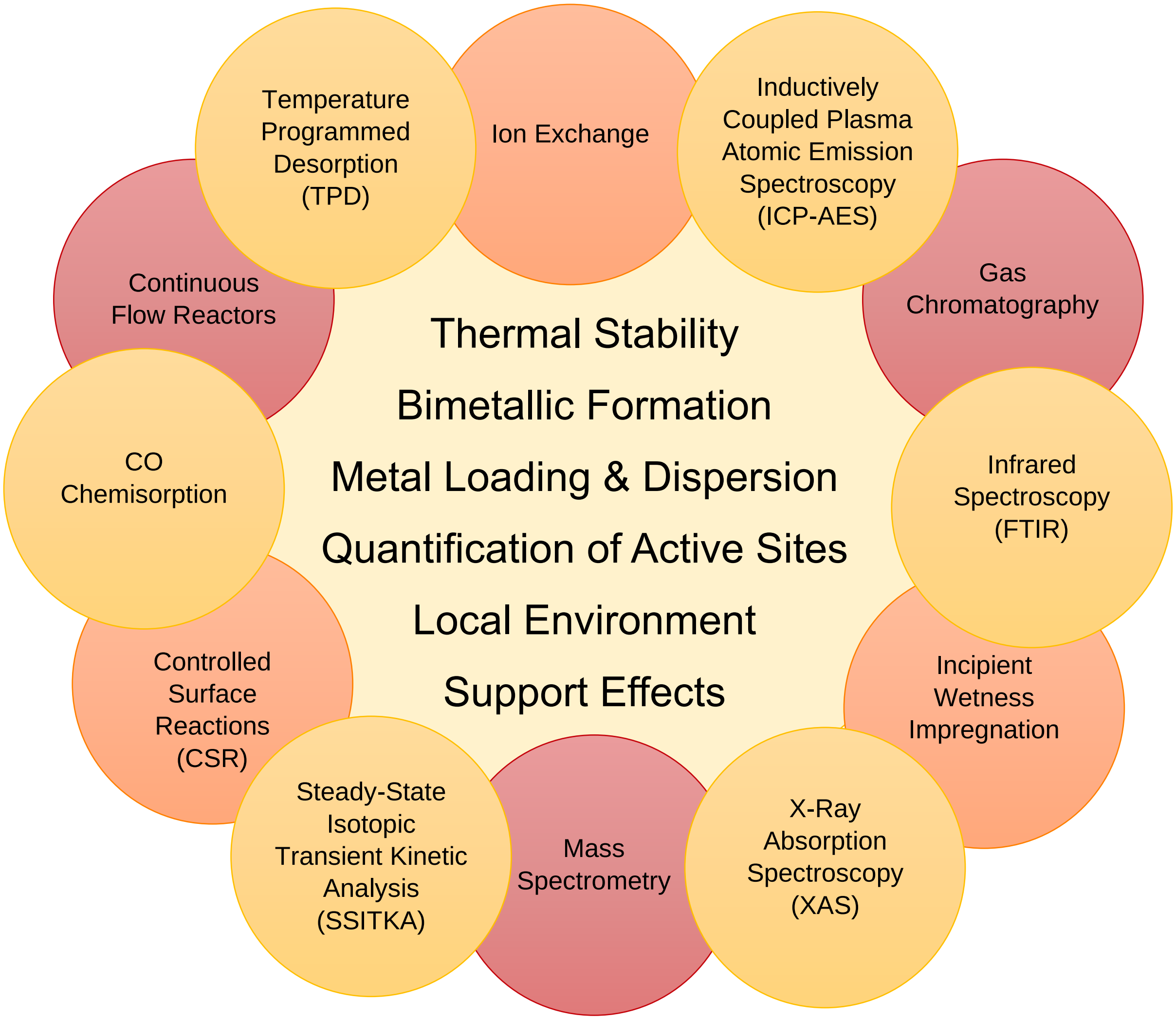

Figure 1.1. Summary of synthesis (orange), characterization (gold), and reactivity (red) techniques used within the scope of this dissertation to study the properties listed in the center.

Physical characterization of catalytic materials generally involves evaluating the morphology, porosity, and texture of surfaces by measuring parameters such as surface topology and metal dispersion as well as pore shape, volume, and size distribution.[2] Gas adsorption techniques are widely used for this purpose. The Brunauer-Emmett-Teller (BET) method using nitrogen as the adsorbate is probably one of the most widely used approaches for the determination of surface area in catalysts and their supports.[4–6] In this method, the surface under study is cooled using liquid nitrogen and known amounts of nitrogen gas at relatively low pressures in near-vacuum conditions are pulsed into the sample cell until the saturation pressure is achieved. Afterwards, the sample is heated to force nitrogen desorption, followed by quantification as a function of relative pressure (p/p_0 = pressure/saturation pressure) in the form of a nitrogen adsorption isotherm.

However, it must be noted that while bulk surface area is an important parameter of heterogeneous catalysts, there may not be a direct relationship between it and catalyst activity. This is particularly true for supported catalysts where the reaction occurs on specific types of active sites, including metal and/or support sites. Therefore, chemisorption measurements to quantify the number of catalytically active sites are widely used. These measurements generally involve gaseous adsorbates such as H_2, CO, O_2, NO, and N_2O at temperatures at or above room temperature, and the choice of adsorbate will depend primarily on the metal under study.[2] Other surface properties that could be conducive to catalytic activity, such as the surface concentration of acidic or basic sites, can be evaluated using temperature-programmed desorption (TPD) techniques. In this case, adsorbates are selected based on the property of interest, with NH_3, CO_2, H_2, and CO being the most common. The desorption rate from a saturated surface is then monitored as a function of temperature and can be used to quantify the amount of desorbed molecules along with the relative strengths of the adsorption sites. Additionally, TPD studies can be used to evaluate desorption kinetics and even the determination of relative coverages of an adsorbate layer.

Techniques similar to TPD methods can be used to evaluate chemical properties of catalysts by monitoring reactive processes such as catalyst reductions (TPR) and oxidations (TPO).[5] The extent of metal reduction can be determined by TPR methods, which help define the necessary temperature and reduction conditions for catalyst treatment by monitoring H_2 consumption as a function of temperature using online mass spectrometry. Similarly, the amount of reduced species present in a sample can be evaluated via TPO. Additionally, TPO can also be used to identify proper calcination conditions for catalyst pretreatment or regeneration following coke deposition. To the latter purpose, thermogravimetric analyses (TGA), where the weight of the catalyst is monitored as a function of temperature in an oxidative environment, are also performed to quantify carbonaceous deposits.

While the techniques previously mentioned are relatively easy to implement in typical laboratory settings, imaging and spectroscopic techniques capable of identifying atomic level structure and electronic configurations typically require more advanced instrumentation. Microscopic techniques, including transmission electron microscopy (TEM) and scanning transmission electron microscopy (STEM), allow researchers to visually analyze the size distribution and shape of metal particles in both supported and un-supported catalysts.[2,7] Additionally, combining STEM with energy dispersive spectroscopy (EDS), for example, allows the user to evaluate the chemical composition of the active components and develop a visual map of the distribution of metal species in materials where more than one species is present.[7–10] These techniques can be used on fresh, spent, and pretreated catalysts to monitor changes in metal morphology. Specifically, changes in particle size distribution, sintering effects, and homogeneity of alloy formation in multi-metallic particles can be observed and used to correlate findings in reactivity studies for structure-sensitive systems.[11–13] The outcome of specialized synthesis techniques can also be measured by microscopic techniques where visual corroboration of morphological features in materials such as nanostructured[14,15] and core-shell[16–20] catalysts is the primary measure of synthesis success.

Spectroscopic techniques, which analyze the interaction between matter and the electromagnetic spectrum, have also been of importance in the study of catalytic materials. By using different portions of the electromagnetic spectrum, different types of excitations can be induced on a material and a wide range of properties can be assessed. Figure 1.2 summarizes some of the most common spectroscopic techniques, arranged by the energetic range in which they operate within the electromagnetic spectrum. Vibrational spectroscopy is an overarching term that encompasses the study of molecular vibrations induced by the absorption or scattering of photons (Infrared and Raman spectroscopy, respectively), electrons (electron energy loss spectroscopy), or neutrons (inelastic neutron scattering).[21] Infrared spectroscopy is the most common type of vibrational spectroscopy and is generally used to identify adsorbed species on a catalyst surface, along with their modes of adsorption.[22] It can also be used to elucidate specific adsorption sites present in a material in both *ex-situ* and *in-situ* studies, the latter of which frequently require the use of specialized cells for analysis.

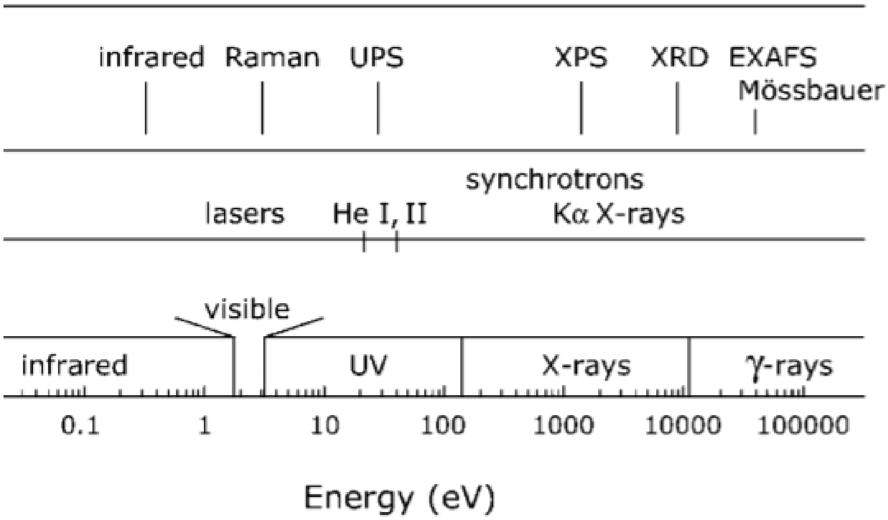

Figure 1.2. Common spectroscopic techniques employed at various energetic points of the electromagnetic spectrum.[21]

On the higher end of the electromagnetic spectrum, X-ray absorption spectroscopy (XAS) uses high intensity, energy-tunable x-rays available only at synchrotron facilities to study formal oxidation states as well as local coordination environments of species in the bulk.[23–25] Analysis of the oxidation states via x-ray absorption near-edge structure (XANES) spectra facilitates the identification of unknown compounds by comparison to fingerprints from reference spectra and is useful in identifying features in electronic structures based on spectral features observed.[26] Meanwhile studies of the extended x-ray absorption fine structure (EXAFS) spectrum can be used to identify the number and type of neighboring atoms as well as their relative distance to the absorbing atom, thus providing useful information regarding local structure. Since this technique is primarily a local structural method, amorphous and solution samples can be readily analyzed since long range order is not needed.[23] Additionally, the XAS technique is useful in both *ex-situ* and *in-situ* studies, including under *in operando* conditions, of homogeneous and heterogeneous catalysts[23,27,28] to evaluate parameters such as crystallite size, dopant effects, and ligand/adsorbate effects.[29–32]

Common use of the majority of techniques previously discussed aims to address the characterization of chemical and structural properties of catalytic materials in an effort to explain activity and selectivity trends observed under steady-state conditions. However, valuable mechanistic information that might not be easily attainable with independent characterization techniques can be obtained directly from kinetic data collected under transient reaction conditions. Steady-state isotopic transient kinetic analysis (SSITKA) has been widely used for this purpose to gain insights on reaction mechanisms, to quantify the concentration, surface coverage, and surface residence time of reactive intermediates, and to directly measure the number of catalytically active sites under reaction conditions.[33–35] In summary, this technique is based upon the detection of isotopic labels in the reactor effluent as a function of time following a step change in the isotopic labelling of a reactant in the feed. Analysis of the resulting transient response profiles thus provides direct information regarding catalytically active sites and plausible reaction pathways. Goodwin and coworkers have investigated the impact of promoting species, support effects, and pretreatment conditions on catalysts used for Fischer-Tropsch synthesis[36–38] and CO hydrogenation[39–42]. Similarly, Davis and coworkers have made extensive use of transient kinetic studies in systems such as ammonia synthesis[43–45], ethanol coupling[46,47], CO hydrogenation[48], and the reduction of propionic acid[49], among others.

Furthermore, coupling the SSITKA technique with other infrared spectroscopic methods such as diffuse reflectance infrared Fourier transform spectroscopy (DRIFTS) can focus further into reactive intermediates on a catalytic surface under reaction conditions.[34,50,51] For example, Meunier and coworkers combined DRIFTS and transient studies to study the Fischer Tropsch reaction over Co-MgO catalysts and found that formate and methylene species observed by DRIFTS did not have significant roles as reaction intermediates in the Fischer-Tropsch system based on SSITKA experiments.[52] Similarly, Thibault-Starzyk and coworkers used SSITKA to clarify the role of surface formate species detected by *operando* infrared studies and determined that the majority of formate species were spectators and not primary intermediates in methanol photo-oxidation.[50] Chuang and coworkers have used *in situ* IR studies combined with transient experiments to elucidate the reaction mechanism involved in the CO_2 reforming of methane[53] as well as the CO hydrogenation and NO-CO reactions[54] over rhodium catalysts.

Finally, it is important to note that while all the characterization techniques discussed so far in this chapter are of an experimental nature, theoretical methods are indispensable to experimental researchers in developing a fundamental understanding of catalytic surfaces. Collaborations with computational researchers have led to the development of detailed kinetic and microkinetic models based on thermodynamic and energetic parameters obtained from first-principles density functional theory (DFT) calculations. These models can be and have been used to identify the most favorable pathways of reaction mechanisms and analyze the effects of surface coverage on reaction kinetics, among other purposes, while also being used to both drive and explain experimental studies and findings. Case studies on water gas shift[55–57], ammonia synthesis[58], and hydrogenation[59–61] reactions serve to highlight the importance of combining theoretical and experimental techniques.

1.3 Dissertation Scope

The work presented in this dissertation aims to highlight the importance of various catalyst characterization techniques in developing a fundamental understanding of the physical and chemical properties responsible for reactivity trends observed in heterogeneous catalysts, as discussed above. Experimental techniques are also combined with theoretical methods for supported catalysts in various reactive systems to further elucidate the governing factors behind catalytic performance.

Chapter 2 explores the effect of support acidity on the reactivity profiles of zeolite-supported platinum and platinum-tin catalysts for the non-oxidative coupling of methane. To this purpose, a series of Pt-Sn/H-ZSM-5 catalysts with SiO_2:Al_2O_3 ratios between 23 and 280 were synthesized and analyzed for their ability to activate the methane molecule under non-oxidative conditions and subsequently generate ethylene and aromatics compounds. N_2 physisorption, CO chemisorption, and NH_3 temperature programed desorption were used to quantify support surface area as well as the active metal site and acid site densities on fresh and spent catalysts. Reactivity studies for Pt-Sn/H-ZSM-5 catalysts showed that while all catalysts produced ethylene as the primary product, increasing support acidity led to an increase in naphthalene selectivity at the expense of benzene selectivity. Furthermore, catalytic activity as a function of time on stream for these acidic catalysts revealed a volcano-shaped behavior in the generation of aromatic products, suggesting that the formation of a reactive hydrocarbon pool on acidic support surfaces could be responsible for the oligomerization of ethylene. Moreover, the best performing Pt-Sn/H-ZSM-5 catalyst was found to be comparable to the state-of-the-art Mo/H-ZSM-5 catalysts in terms of carbon product generation and resistance to coke formation.

Chapter 3 demonstrates the use of x-ray absorption spectroscopy (XAS) as a key tool to highlight the effect of local electronic and structural environments of multi-metallic catalysts in a variety of reaction case studies. Pd-based monometallic and bimetallic catalysts synthesized via controlled surface reactions were studied using XAS techniques to inspect the local coordination and nearest-neighbor distance of Pd species in order to understand Pd dispersion on the parent metal as well as the effect of catalyst support on the extent of bimetallic particle formation. Near-edge structure analyses were also used on these Pd catalysts, as well as on a set of Mo-containing multi-metallic catalysts prepared by atomic layer deposition, to understand catalyst reducibility along with potential support and hydrogen spillover effects on the extent of metal reduction. The results of these XAS analyses were used to support findings from additional characterization techniques in explaining the catalytic performance of these materials in amination, hydrodechlorination, hydrogenation, and synthesis gas conversion reactions.

Chapter 4 explores the effects of catalyst support and pretreatment environment on the activity of platinum-based catalysts for the hydrogenation of acetone. Pt/H-ZSM-5 catalysts were found to be 2-3 orders of magnitude more active than SiO_2 and Al_2O_3-supported catalysts, regardless of pretreatment conditions. For the Pt/H-ZSM-5 materials, catalysts calcined at 773 K were more active than those calcined at 573 K and, at each calcination temperature, those reduced at 353 K displayed higher activity than those reduced at 573 K. This behavior was attributed to the effects of oxidative and reductive treatments on the morphological characteristics of platinum nanoparticles, since the temperatures have been shown to influence metal dispersion differently based on the pretreatment gas used. CO-FTIR measurements showed a shift to higher frequency of the Pt-CO band in ZSM-5-based catalysts compared to SiO_2, which was attributed to electronic effects from interactions between Pt species and the zeolite channels. It was therefore suggested that interactions between Pt particles and the zeolite pores, including stabilization of the particles and possible confinement effects, could be responsible for the enhanced hydrogenation activity observed over the Pt/ZSM-5 catalysts.

Chapter 5 presents a theoretical and experimental study that explores the importance of surface coverage effects in the hydrogenation of acetone over a platinum catalyst using transient kinetics techniques. Transient response models based on steady-state microkinetic analyses employing traditional Langmuir-type isotherms were found to predict full removal of the most abundant reactive intermediate (MARI) from the catalytic platinum surface following both removal or substitution of the acetone species in the reactant feed. In contrast, models accounting for the effects of nearest-neighbor interactions by use of the Bragg-Williams approximation predicted that full removal of the MARI species from the catalytic surface could only be achieved following the substitution of acetone by its isotopically-labeled counterpart in the reactant feed, while removal of the acetone species from the feed led only to minimal changes in the MARI surface coverage. Analogous experimental studies using SSITKA methods served to validate the theoretical predictions and provided tangible evidence for the importance of surface coverage effects in understanding the reactivity of platinum catalysts for acetone hydrogenation.

Chapter 6 provides a summary of the main conclusions obtained in this work and discusses potential directions for future research in the area of transient kinetics for heterogeneous catalysts. Further development and use of transient techniques, combined with various other structural characterization methods, can lead to in-depth understanding of reactive systems and enable better design and application of catalytic materials.

1.4 References

(1) Armor, J. N. A History of Industrial Catalysis. *Catal. Today* **2011**, *163* (1), 3–9.

(2) Hagen, J. Heterogeneous Catalysis: Fundamentals. In *Industrial Catalysis: A Practical Approach*; Wiley-VCH Verlag GmbH & Co. KGaA: Weinheim, Germany, 2015; pp 99–209.

(3) Farrauto, R. J. Industrial Catalysis: A Practical Guide. In *Handbook of Industrial Chemistry and Biotechnology*; Kent, J. A., Ed.; Springer International Publishing, 2017; pp 1995–2035.

(4) Grünert, W. Principles and Practice of Heterogeneous Catalysis. *Zeitschrift für Phys. Chemie* **1998**, *205* (Part_1), 130–131.

(5) Webb, P. A. Introduction to Chemical Adsorption Analytical Techniques and Their Applications to Catalysis. *MIC Tech. Publ.* **2003**, *13* (January), 1–4.

(6) Raja, P. M. V.; Barron, A. R. BET Surface Area Analysis of Nanoparticles https://chem.libretexts.org/Bookshelves/Analytical_Chemistry/Book%3A_Physical_Methods_in_Chemistry_and_Nano_Science_(Barron)/00%3A_Front_Matter/01%3A_TitlePage (accessed Jul 13, 2020).

(7) Liu, J. Advanced Electron Microscopy Characterization of Nanostructured Heterogeneous Catalysts. In *Microscopy and Microanalysis*; 2004; Vol. 10, pp 55–76.

(8) Ball, M. R.; Wesley, T. S.; Rivera-Dones, K. R.; Huber, G. W.; Dumesic, J. A. Amination of 1-Hexanol on Bimetallic AuPd/TiO2 Catalysts. *Green Chem.* **2018**, *20* (20), 4695–4709.

(9) Hakim, S. H.; Sener, C.; Alba-Rubio, A. C.; Gostanian, T. M.; O'Neill, B. J.; Ribeiro, F. H.; Miller, J. T.; Dumesic, J. A. Synthesis of Supported Bimetallic Nanoparticles with Controlled Size and Composition Distributions for Active Site Elucidation. *J. Catal.* **2015**, *328*, 75–90.

(10) Sener, C.; Wesley, T. S.; Alba-Rubio, A. C.; Kumbhalkar, M. D.; Hakim, S. H.; Ribeiro, F. H.; Miller, J. T.; Dumesic, J. A. PtMo Bimetallic Catalysts Synthesized by Controlled Surface Reactions for Water Gas Shift. *ACS Catal.* **2016**, *6* (2), 1334–1344.

(11) Claus, P.; Hofmeister, H. Electron Microscopy and Catalytic Study of Silver Catalysts: Structure Sensitivity of the Hydrogenation of Crotonaldehyde. *J. Phys. Chem. B* **1999**, *103* (14), 2766–2775.

(12) Valden, M.; Pak, S.; Lai, X.; Goodman, D. W. Structure Sensitivity of CO Oxidation over Model Au/TiO2 Catalysts. *Catal. Letters* **1998**, *56* (1), 7–10.

(13) Andersson, M. P.; Abild-Pedersen, F.; Remediakis, I. N.; Bligaard, T.; Jones, G.; Engbæk, J.; Lytken, O.; Horch, S.; Nielsen, J. H.; Sehested, J.; et al. Structure Sensitivity of the Methanation Reaction: H2-Induced CO Dissociation on Nickel Surfaces. *J. Catal.* **2008**, *255* (1), 6–19.

(14) Di Gregorio, F.; Bisson, L.; Armaroli, T.; Verdon, C.; Lemaitre, L.; Thomazeau, C. Characterization of Well Faceted Palladium Nanoparticles Supported on Alumina by

Transmission Electron Microscopy and FT-IR Spectroscopy of CO Adsorption. *Appl. Catal. A Gen.* **2009**, *352* (1–2), 50–60.

(15) Kibsgaard, J.; Clausen, B. S.; Topsøe, H.; Lægsgaard, E.; Lauritsen, J. V.; Besenbacher, F. Scanning Tunneling Microscopy Studies of TiO2-Supported Hydrotreating Catalysts: Anisotropic Particle Shapes by Edge-Specific MoS2-Support Bonding. *J. Catal.* **2009**, *263* (1), 98–103.

(16) Lei, Y.; Liu, B.; Lu, J.; Lobo-Lapidus, R. J.; Wu, T.; Feng, H.; Xia, X.; Mane, A. U.; Libera, J. A.; Greeley, J. P.; et al. Synthesis of Pt-Pd Core-Shell Nanostructures by Atomic Layer Deposition: Application in Propane Oxidative Dehydrogenation to Propylene. *Chem. Mater.* **2012**, *24* (18), 3525–3533.

(17) Zhang, S.; Chen, C.; Cargnello, M.; Fornasiero, P.; Gorte, R. J.; Graham, G. W.; Pan, X. Dynamic Structural Evolution of Supported Palladium-Ceria Core-Shell Catalysts Revealed by in Situ Electron Microscopy. *Nat. Commun.* **2015**, *6* (1), 1–6.

(18) Oezaslan, M.; Hasché, F.; Strasser, P. Pt-Based Core-Shell Catalyst Architectures for Oxygen Fuel Cell Electrodes. *J. Phys. Chem. Lett.* **2013**, *4* (19), 3273–3291.

(19) Wojtysiak, S.; Solla-Gullón, J.; Dłuzewski, P.; Kudelski, A. Synthesis of Core-Shell Silver-Platinum Nanoparticles, Improving Shell Integrity. *Colloids Surfaces A Physicochem. Eng. Asp.* **2014**, *441*, 178–183.

(20) Lu, J.; Elam, J. W.; Stair, P. C. Atomic Layer Deposition—Sequential Self-Limiting Surface Reactions for Advanced Catalyst “Bottom-up” Synthesis. *Surf. Sci. Rep.* **2016**, *71* (2), 410–472.

(21) Niemantsverdriet, J. W. *Spectroscopy in Catalysis*; Wiley, 2007.

(22) Thibault-Starzyk, F.; Mauge, F. Infrared Spectroscopy. In *Characterization of Solid Materials and Heterogeneous Catalysts: From Structure to Surface Reactivity*; Che, M., Vedrine, J. C., Eds.; Wiley-VCH Verlag GmbH & Co. KGaA, 2012; pp 3–45.

(23) Nelson, R. C.; Miller, J. T. An Introduction to X-Ray Absorption Spectroscopy and Its in Situ Application to Organometallic Compounds and Homogeneous Catalysts. *Catal. Sci. Technol* **2012**, *2*, 461–470.

(24) Newville, M. Fundamentals of XAFS. *Rev. Mineral. Geochemistry* **2014**, *78* (1), 33–74.

(25) Lacheen, H. S.; Iglesia, E. Stability, Structure, and Oxidation State of Mo/H-ZSM-5 Catalysts during Reactions of CH4 and CH4-CO2 Mixtures. *J. Catal.* **2005**, *230* (1), 173–185.

(26) Penner-Hahn, J. E. X-Ray Absorption Spectroscopy. In *Comprehensive Coordination Chemistry II*; McCleverty, J. A., Meyer, T. J., Eds.; Pergamon, 2003; Vol. 2, pp 159–186.

(27) Fornasini, P. Introduction to X-Ray Absorption Spectroscopy. In *Synchrotron Radiation: Basics, Methods and Applications*; 2015; pp 181–211.

(28) Geantet, C.; Pichon, C. X-Ray Absorption Spectroscopy. In *Characterization of Solid Materials and Heterogeneous Catalysts: From Structure to Surface Reactivity*; Che, M.,

Vedrine, J. C., Eds.; Wiley-VCH Verlag GmbH & Co. KGaA, 2012; pp 511–534.

(29) Spieker, W. A.; Liu, J.; Miller, J. T.; Kropf, A. J.; Regalbuto, J. R. An EXAFS Study of the Co-Ordination Chemistry of Hydrogen Hexachloroplatinate(IV): 1. Speciation in Aqueous Solution. *Appl. Catal. A Gen.* **2002**, *232* (1–2), 219–235.

(30) Gracia, F. J.; Bollmann, L.; Wolf, E. E.; Miller, J. T.; Kropf, A. J. In Situ FTIR, EXAFS, and Activity Studies of the Effect of Crystallite Size on Silica-Supported Pt Oxidation Catalysts. *J. Catal.* **2003**, *220* (2), 382–391.

(31) Gracia, F. J.; Miller, J. T.; Kropf, A. J.; Wolf, E. E. Kinetics, FTIR, and Controlled Atmosphere EXAFS Study of the Effect of Chlorine on Pt-Supported Catalysts during Oxidation Reactions. *J. Catal.* **2002**, *209*, 341–354.

(32) Spieker, W. A.; Liu, J.; Hao, X.; Miller, J. T.; Kropf, A. J.; Regalbuto, J. R. An EXAFS Study of the Coordination Chemistry of Hydrogen Hexachloroplatinate (IV) - 2. Speciation of Complexes Adsorbed onto Alumina. *Appl. Catal. A Gen.* **2003**, *243* (1), 53–66.

(33) Ali, S. H.; Goodwin, J. G. Isotopic Transient Kinetic Analysis of the Induction Phenomenon for Methanol Synthesis on Pd/SiO2. *J. Catal.* **1997**, *170* (2), 265–274.

(34) Ledesma, C.; Yang, J.; Chen, D.; Holmen, A. Recent Approaches in Mechanistic and Kinetic Studies of Catalytic Reactions Using SSITKA Technique. *ACS Catalysis*. 2014, pp 4527–4547.

(35) Shannon, S. L.; Goodwin, J. G. Characterization of Catalytic Surfaces by Isotopic-Transient Kinetics during Steady-State Reaction. *Chem. Rev.* **1995**, *95*, 677–695.

(36) Sudsakorn, K.; Goodwin, J. G.; Adeyiga, A. A. Effect of Activation Method on Fe FTS Catalysts: Investigation at the Site Level Using SSITKA. *J. Catal.* **2003**, *213* (2), 204–210.

(37) Lohitharn, N.; Goodwin, J. G. Impact of Cr, Mn and Zr Addition on Fe Fischer-Tropsch Synthesis Catalysis: Investigation at the Active Site Level Using SSITKA. *J. Catal.* **2008**, *257* (1), 142–151.

(38) Lohitharn, N.; Goodwin, J. G. An Investigation Using SSITKA of Chain Growth on Fe and FeMnK Fischer-Tropsch Synthesis Catalysts. *Catal. Commun.* **2009**, *10* (6), 758–762.

(39) Ali, S. H.; Goodwin, J. G. SSITKA Investigation of Palladium Precursor and Support Effects on CO Hydrogenation over Supported Pd Catalysts. *J. Catal.* **1998**, *176* (1), 3–13.

(40) Panpranot, J.; Goodwin Jr., J. G.; Sayari, A. CO Hydrogenation on Ru-Promoted Co/MCM-41 Catalysts. *J. Catal.* **2002**, *211* (2), 530–539.

(41) Tsai, Y. T.; Mo, X.; Goodwin, J. G. The Synthesis of Hydrocarbons and Oxygenates during CO Hydrogenation on CoCuZnO Catalysts: Analysis at the Site Level Using Multiproduct SSITKA. *J. Catal.* **2012**, *285* (1), 242–250.

(42) Vada, S.; Chen, B.; Goodwin, J. G. Isotopic Transient Study of La Promotion of Co/Al2O3or CO Hydrogenation. *J. Catal.* **1995**, *153* (2), 224–231.

(43) McClaine, B. C.; Davis, R. J. Importance of Product Readsorption during Isotopic Transient Analysis of Ammonia Synthesis on Ba-Promoted Ru/BaX Catalyst. *J. Catal.* **2002**, *211* (2),

379–386.

(44) Davis, R. J.; McClaine, B. C. Isotopic Transient Kinetic Analysis of Cs-Promoted Ru/MgO during Ammonia Synthesis. *J. Catal.* **2002**.

(45) Siporin, S. E.; Davis, R. J. Isotopic Transient Analysis of Ammonia Synthesis over Ru/MgO Catalysts Promoted by Cesium, Barium, or Lanthanum. *J. Catal.* **2004**, *222* (2), 315–322.

(46) Birky, T. W.; Kozlowski, J. T.; Davis, R. J. Isotopic Transient Analysis of the Ethanol Coupling Reaction over Magnesia. *J. Catal.* **2013**, *298*, 130–137.

(47) Hanspal, S.; Young, Z. D.; Shou, H.; Davis, R. J. Multiproduct Steady-State Isotopic Transient Kinetic Analysis of the Ethanol Coupling Reaction over Hydroxyapatite and Magnesia. *ACS Catal.* **2015**, *5* (3), 1737–1746.

(48) Shou, H.; Davis, R. J. Multi-Product Steady-State Isotopic Transient Kinetic Analysis of CO Hydrogenation over Supported Molybdenum Carbide. *J. Catal.* **2013**, *306*, 91–99.

(49) Kammert, J. D.; Xie, J.; Godfrey, I. J.; Unocic, R. R.; Stavitski, E.; Attenkofer, K.; Sankar, G.; Davis, R. J. Reduction of Propionic Acid over a Pd-Promoted ReOx/SiO2 Catalyst Probed by X-Ray Absorption Spectroscopy and Transient Kinetic Analysis. *ACS Sustain. Chem. Eng.* **2018**, *6* (9), 12353–12366.

(50) El-Roz, M.; Bazin, P.; Daturi, M.; Thibault-Starzyk, F. Operando Infrared (IR) Coupled to Steady-State Isotopic Transient Kinetic Analysis (SSITKA) for Photocatalysis: Reactivity and Mechanistic Studies. *ACS Catal.* **2013**, *3* (12), 2790–2798.

(51) Tibiletti, D.; Goguet, A.; Reid, D.; Meunier, F. C.; Burch, R. On the Need to Use Steady-State or Operando Techniques to Investigate Reaction Mechanisms: An in Situ DRIFTS and SSITKA-Based Study Example. In *Catalysis Today*; Elsevier, 2006; Vol. 113, pp 94–101.

(52) Schweicher, J.; Bundhoo, A.; Frennet, A.; Kruse, N.; Daly, H.; Meunier, F. C. DRIFTS/MS Studies during Chemical Transients and SSITKA of the CO/H 2 Reaction over Co-MgO Catalysts. *J. Phys. Chem. C* **2010**, *114* (5), 2248–2255.

(53) Stevens, R. W.; Chuang, S. S. C. In Situ IR Study of Transient CO 2 Reforming of CH 4 over RH/Al 2O 3. *J. Phys. Chem. B* **2004**, *108* (2), 696–703.

(54) Chuang, S. S. C.; Brundage, M. A.; Balakos, M. W.; Srinivas, G. Transient in Situ Infrared Methods for Investigation of Adsorbates in Catalysis. *Appl. Spectrosc.* **1995**, *49* (8), 1151–1163.

(55) Grabow, L. C.; Gokhale, A. A.; Evans, S. T.; Dumesic, J. A.; Mavrikakis, M. Mechanism of the Water Gas Shift Reaction on Pt: First Principles, Experiments, and Microkinetic Modeling. *J. Phys. Chem. C* **2008**, *112* (12), 4608–4617.

(56) Madon, R. J.; Braden, D.; Kandoi, S.; Nagel, P.; Mavrikakis, M.; Dumesic, J. A. Microkinetic Analysis and Mechanism of the Water Gas Shift Reaction over Copper Catalysts. *J. Catal.* **2011**, *281* (1), 1–11.

(57) Ammal, S. C.; Heyden, A. Water-Gas Shift Catalysis at Corner Atoms of Pt Clusters in

Contact with a TiO2 (110) Support Surface. *ACS Catal.* **2014**, *4* (10), 3654–3662.

(58) Boisen, A.; Dahl, S.; Jacobsen, C. J. H. Promotion of Binary Nitride Catalysts: Isothermal N2 Adsorption, Microkinetic Model, and Catalytic Ammonia Synthesis Activity. *J. Catal.* **2002**, *208* (1), 180–186.

(59) Heard, C. J.; Hu, C.; Skoglundh, M.; Creaser, D.; Grönbeck, H. Kinetic Regimes in Ethylene Hydrogenation over Transition-Metal Surfaces. *ACS Catal.* **2016**, *6* (5), 3277–3286.

(60) Rekoske, J. E.; Cortright, R. D.; Goddard, S. A.; Sharma, S. B.; Dumesic, J. A. Microkinetic Analysis of Diverse Experimental Data for Ethylene Hydrogenation on Platinum. *J. Phys. Chem.* **1992**, *96* (4), 1880–1888.

(61) Demir, B.; Kropp, T.; Rivera-Dones, K. R.; Gilcher, E. B.; Huber, G. W.; Mavrikakis, M.; Dumesic, J. A. A Self-Adjusting Platinum Surface for Acetone Hydrogenation. *Proc. Natl. Acad. Sci. U. S. A.* **2020**, *117* (7), 3446–3450.

Chapter 2. Effect of Zeolite Acidity on Supported Pt-Sn Catalysts for the Non-Oxidative Coupling of Methane[a,b]

2.1 Introduction

Methane is a stable molecule that is difficult to activate without significant energy input, and its activation and subsequent conversion into more valuable chemicals has long been recognized as an important challenge.[1,2] While many studies have addressed oxidative coupling of methane, nonoxidative methane coupling techniques to produce ethane, ethylene, and aromatics have also received significant attention. However, thermodynamic considerations limit nonoxidative methane conversion, even at high temperatures (970 K), to less than 10% for C_2 products, while carbon formation is highly favored and results in surface deactivation and loss of selectivity.[2]

A promising class of catalysts for non-oxidative methane conversion chemistry is comprised of shape-selective silica−alumina zeolites such as ZSM-5, ZSM-8, ZSM-11, and MCM-22 modified with transition metal species such as molybdenum.[3–5] Early work by Wang et al. reported that benzene could be produced on Mo- or Zn-modified ZSM-5 catalysts at 973 K under nonoxidizing conditions.[6] A bifunctional mechanism was proposed, with activation of methane on molybdenum-containing sites and dimerization of CH_3 radicals to form ethane and ethylene, followed by aromatization of ethylene to benzene on Brønsted acid sites.[7,8] Additionally, numerous studies have investigated the activity of transition metals such as Fe, Re, V, and Cr supported on SiO_2 and H-ZSM-5 for methane conversion.[9–12]

---

[a] This chapter has been adapted from the following publication: Gerceker, D.; Motagamwala, A. H.; Rivera-Dones, K.; Miller, J. B.; Huber, G. W.; Mavrikakis, M.; Dumesic, J. A. "Methane Conversion to Ethylene and Aromatics on PtSn Catalysts" *ACS Catal.* 7 (2017) 2088-2100

[b] Author contributions: DG performed reactivity and characterization experiments for SiO_2- and ZSM-5 (280)-supported Pt and Pt-Sn catalysts , DG and AHM developed microkinetic model, KRD performed characterization, reactivity experiments, and data analysis for effects of support acidity and comparisons to Mo/ZSM-5 catalysts. All authors contributed to manuscript development and review.

Besides transition metals, the effect of using noble metals such as platinum has also been researched. In an early work that addressed low-temperature activation of methane, a 6 wt % Pt/SiO_2 catalyst was first exposed to methane at 523 K and then flushed with H_2, resulting in the formation of C_2 to C_7 hydrocarbon products. Pt/H-X and Pt/H-Y catalysts with the same metal loading exhibited higher methane conversion and higher formation rates of C_3 and C_5 products. The catalysts were not effective at higher temperatures because of coke deposition on Pt.[13,14] At 973 K, a 2 wt % Pt/H-ZSM-5 catalyst exhibited low methane conversions. However, adding Pt to Mo/H-ZSM-5 improved the catalytic activity of Mo/H-ZSM-5 by decreasing the rate of coke formation.[15,16] The active sites of the catalyst were hypothesized to be associated with a $PtMoO_3$-H-ZSM-5 structure on the catalyst.[17] At 973 K, addition of 0.1 wt % Sn to the Pt-Mo/H-ZSM-5 catalyst yielded slightly lower methane conversion while decreasing the extent of coke deposition and increasing the selectivity to aromatics. Catalysts prepared by sequential impregnation of Pt followed by Sn exhibited higher benzene selectivity and better coke mitigation in comparison to catalysts prepared by coimpregnation.[18,19]

Recent work within our group[20] investigated the effects of Pt and Pt-Sn for non-oxidative methane conversion, and found that the addition of Sn to Pt/SiO_2 led to a three-fold increase in ethylene turnover frequency (TOF) and a two-fold increase in benzene TOF, with higher conversion to products and higher ethylene selectivity than on Pt/SiO_2. Furthermore, when using ZSM-5 as support, the ethylene TOF was found to be 4 times higher for Pt-Sn/ZSM-5 than Pt/ZSM-5 and 15 times higher than that of the Pt-Sn/SiO_2 catalyst. Overall, the ZSM-5-supported catalysts demonstrated better activity than the SiO_2 supported materials, with the bimetallics showing higher activity towards the formation of ethylene and benzene than the monometallics. Scanning transmission electron microscope (STEM) imaging highlighted the presence of smaller metal particle sizes in ZSM-5 catalysts when compared to SiO_2, which served as a partial explanation for the improved activity over zeolite-based catalysts.

The effects of particle size on the activity over Pt and Pt-Sn catalysts were further supported by a microkinetic model developed for the non-oxidative coupling of methane as part of the same study. This model used thermodynamic and kinetic parameters derived from density functional theory (DFT) calculations for terrace and step surfaces of Pt and Pt-Sn to predict product formation rates and surface coverages of intermediate species at reaction conditions. Specifically, the effects of Sn addition, hydrogen co-feeding, and particle size were considered. Figure 2.1 shows the variation of surface coverages for the various intermediate species as well as the ethylene TOF values predicted for the surfaces studied. The model predicted platinum terrace and step sites were almost fully covered with adsorbed intermediate species, identified as mainly CH and C. Coverage by these species was drastically reduced with the addition of tin on terrace sites and even more so on step sites, where coverage was predicted to be mostly adsorbed hydrogen.

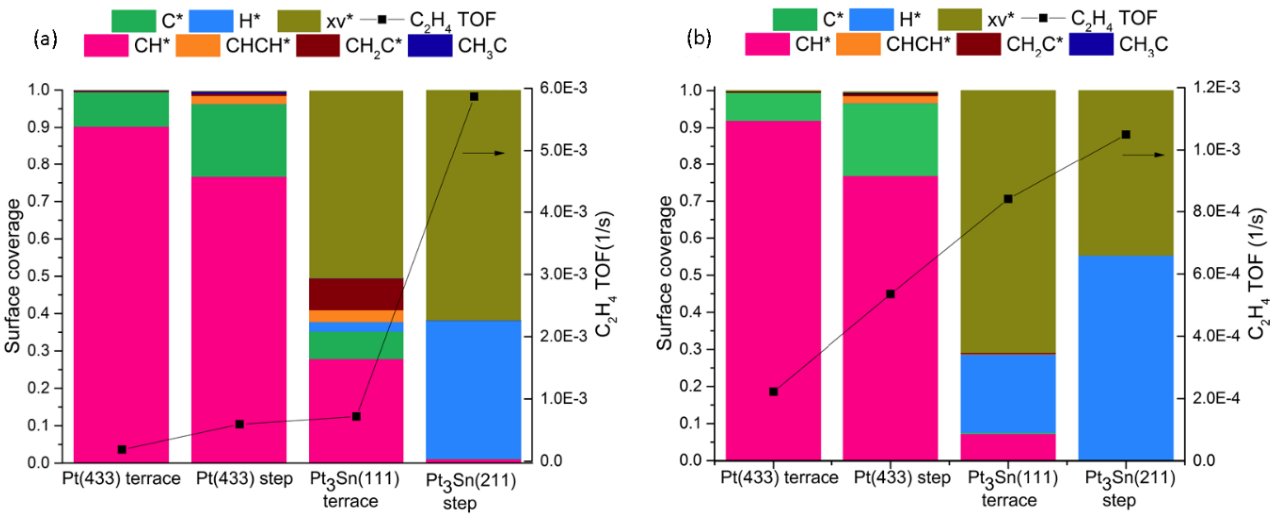

Figure 2.1. Predicted surface coverages and ethylene TOF values with (a) pure methane and (b) 5% H_2 co-feeding. Reaction Conditions: 973 K, 2 g catalyst, 42 cm^3/min CH_4 [+ 2 cm^3/min H_2 for (b)]

Moreover, the model predicted that these bimetallic surfaces contained a large fraction of vacant sites (>0.40) and were therefore cleaner than the monometallic surfaces. Figure 2.1(a) shows that the Pt-Sn step surface has a higher vacancy than the Pt-Sn terrace under a pure methane feed, which suggests the step sites should be more catalytically active. This, in turn, supports the observation drawn from STEM imaging that the higher reactivity seen experimentally with Pt-Sn/ZSM-5 over Pt-Sn/SiO_2 could be in part due to the zeolite-supported catalyst having a larger fraction of smaller nanoparticles. The model also predicted higher catalytic activity with steps of the PtSn surface in terms of ethylene TOF. As seen in Figure 2.1, a substantial increase in this parameter was seen on the bimetallic stepped surface when compared to the other surfaces studied. When compared to the experimental results, the model can be said to succeed in qualitatively predicting the reactivity improvements seen with the Pt-Sn catalysts.

In this chapter, we further evaluate the nonoxidative methane conversion on Pt-Sn bimetallic catalysts that exhibit high activity, selectivity, and stability for production of ethylene. We show that the addition of Brønsted acid sites to Pt-Sn/ZSM-5 leads to catalysts that are active for the conversion of methane to benzene and naphthalene. This occurs through a bifunctional mechanism, whereby ethylene is produced on highly dispersed Pt-Sn nanoparticles, followed by its conversion to benzene and naphthalene on Brønsted acid sites within the zeolite support.

2.2 Experimental Methods

2.2.1 Catalyst Synthesis

Catalysts consisting of Pt-Sn supported on H-ZSM-5 were prepared by incipient wetness impregnation. For this purpose, four different ZSM-5 supports with nominal SiO_2:Al_2O_3 ratios of 23, 50, 80, and 280 were obtained in NH_4^+ form (Zeolyst). Prior to impregnation, supports were calcined in air at 873 K for 18 h to remove ammonia and obtain the H-ZSM-5 form. On the basis of the targeted Pt:Sn atomic ratio of 1:2 for a 0.58 wt% Pt catalyst, the required amount of the Sn precursor, tri-n-butyltin (Strem Chemicals Inc., min 94%), was dissolved in methanol and impregnated onto the zeolite support. After it was dried overnight at 373 K, the catalyst was calcined under 50 cm^3 (STP)/min of air flow at 573 K for 2 h. Subsequently, Sn/H-ZSM-5 was impregnated with Pt using an aqueous solution of tetraammineplatinum (II) nitrate precursor (Sigma Aldrich, 99%). The resulting catalyst was dried overnight at 373 K, treated in 50 cm^3 (STP)/min of Ar at 573 K for 1 h, and reduced under H_2 at 773 K for 6 h. Prior to contact with air, the catalyst was cooled to room temperature under Ar flow and passivated with flowing 1% O_2/Ar for 30 min. Catalysts prepared by this procedure are labeled as Pt-Sn/Z-280, Pt-Sn/Z-80, Pt-Sn/Z-50, and Pt-Sn/Z-23 on the basis of their composition and SiO_2:Al_2O_3 ratio.

Zeolite-supported molybdenum catalysts were also prepared in this study. Catalysts with 0.58 wt% and 4 wt% Mo loading were synthesized via incipient wetness impregnation on H-ZSM-5 with $SiO_2/Al_2O_3 = 50$. The zeolite support was pretreated as previously described. To achieve the desired loadings, the required amount of ammonium molybdate tetrahydrate was dissolved in de-ionized water and impregnated onto the zeolite support. As before, the resulting catalyst was dried overnight at 373 K, treated in 50 cm^3 (STP)/min of Ar at 573 K for 1 h, and reduced under H_2 at 773 K for 6 h. The catalyst was then cooled to room temperature under Ar flow and passivated with flowing 1% O_2/Ar for 30 min before exposure to ambient air.

2.2.2 Catalyst Characterization

Textural properties of the blank H-ZSM-5 catalysts were determined from N_2 adsorption−desorption isotherms obtained at 77 K using the same instrument. Prior to the adsorption measurements, samples were degassed at 423 K and evacuated for 6 h. Specific surface areas of the catalysts were calculated by the BET method.

The platinum surface site density of the fresh catalysts was determined by CO chemisorption at 308 K (Micromeritics, ASAP, 2020C Analyzer). Turnover frequencies (TOF) for product formation were normalized by the Pt site density value of the catalyst.

The acid site densities of fresh and spent catalysts were measured by NH_3-temperature-programmed desorption (NH_3-TPD). A 100 mg portion of each catalyst sample was heated to 473 K under helium flow and kept at a constant temperature for 1 h. After cooling to 423 K, NH_3 was adsorbed on the sample from a 1% NH_3/He flow for 45 min. Following a purge with helium at 423 K for 90 min to remove weakly adsorbed NH_3, the sample was heated to 973 K under helium flow with a 10 K/min ramp and held at 973 K for 2 h. Online analysis of desorbed species was performed using a Pfeiffer Vacuum Omnistar mass spectrometer.

Thermogravimetric analysis (TGA) was performed on spent catalysts to quantify the amount of deposited coke (TGA 500). In this analysis, 25−30 mg of the spent catalyst sample was heated from room temperature to 973 K with a ramp of 20 K/ min under oxygen flow. The change in the sample mass due to combustion of coke and release of CO_2 was used in the calculation of the amount of coke deposition.

2.2.3 Reactivity Measurements

Reactivity experiments were conducted in a ¼ inch stainless steel reactor packed with 0.25 g of catalyst diluted in 2 – 2.5 g of silica chips. Following an *in-situ* reduction with H_2 for 1 h at 773 K, the catalyst was heated to 973 K under flowing He. Once the reactor temperature reached 973 K, a feed stream of 10% N_2/CH_4 at 10.5 cm_3 (STP)/min was introduced. Analysis of the reaction products was carried out by an online gas chromatograph (Shimadzu Corp., GC-2014) equipped with an Agilent J&W GS-GasPro column and a flame ionization detector. All system lines between the reactor outlet and the GC sampling loop inlet were heat-traced to 493 K to prevent product condensation.

2.3 Results and Discussion

The surface area of the blank zeolite supports was obtained using N_2 physisorption, and the results are shown in Table 2.1. The BET surface areas obtained for the blank H-ZSM-5 supports were in agreement with values reported in the literature.[6,21] The platinum site density for the impregnated Pt-Sn catalysts was obtained via CO chemisorption, and the results are also shown in Table 2.1. All catalysts were prepared with the same target platinum loading, and resulted in similar active site densities, suggesting that all catalysts were prepared with similar platinum dispersion.

Table 2.1. BET surface area of zeolite supports and platinum site density of Pt-Sn catalysts

Support	BET Surface Area[a] (m^2/g)	Catalyst	Pt Site Density[b] (µmol Pt/g)
Z-23	355	Pt-Sn/Z-23	8.9
Z-50	397	Pt-Sn/Z-50	4.8
Z-80	351	Pt-Sn/Z-80	6.3
Z-280	378	Pt-Sn/Z-280	5.6

[a] BET surface area determined by N_2 physisorption, ± 5 m^2/g
[b] Platinum site density measured by CO chemisorption

The acid site densities of the blank supports, the impregnated catalysts, and the spent samples are shown in Table 2.2. As expected, the calculated acid site density from the desorption of ammonia decreased with increasing SiO_2:Al_2O_3 ratio of the H-ZSM-5 support (from 850 to 62 µmol/g). The same trend was observed with the samples of fresh catalysts on which Sn and Pt were impregnated (from 710 to 41 µmol/g). Similarly, on the spent catalysts collected at the end of the reaction, the acid site density decreased with increasing SiO_2:Al_2O_3 ratio; however, the range of the values was narrower (from 140 to 90 μmol/g). This difference may be related to the accumulation of coke deposits on the acid sites of the support.

Table 2.2. Acid site density as determined by NH_3-TPD for zeolite supports as well as fresh and spent Pt-Sn catalysts.

Support	**Acid Site Density (μmol/g)**	**Catalyst**	**Acid Site Density (μmol/g)**	
			Fresh	**Spent**
Z-23	850	Pt-Sn/Z-23	710	140
Z-50	270	Pt-Sn/Z-50	280	120
Z-80	250	Pt-Sn/Z-80	250	120
Z-280	62	Pt-Sn/Z-280	41	90

To study the effect of surface acidity on catalyst performance and the product distribution of zeolite-supported catalysts, we prepared Pt-Sn catalysts using a variety of acidic H-ZSM-5 supports: Z-280, Z-80, Z-50, and Z-23. Figure 2.2a shows the ethylene TOF as a function of time on stream over four Pt-Sn catalysts supported on H-ZSM-5 supports with different acidities. The highest rate of ethylene production was observed on the Pt-Sn/Z-50 catalyst. The catalyst showed an increasing ethylene TOF profile up to more than 20 h, after which it began to decrease. The less acidic catalyst Pt-Sn/Z-80 reached an earlier peak around 10 h with almost half of the ethylene TOF value of Pt-Sn/Z-50, and the least acidic Pt-Sn/Z-280 catalyst yielded almost a flat profile in comparison to the other three more acidic catalysts.

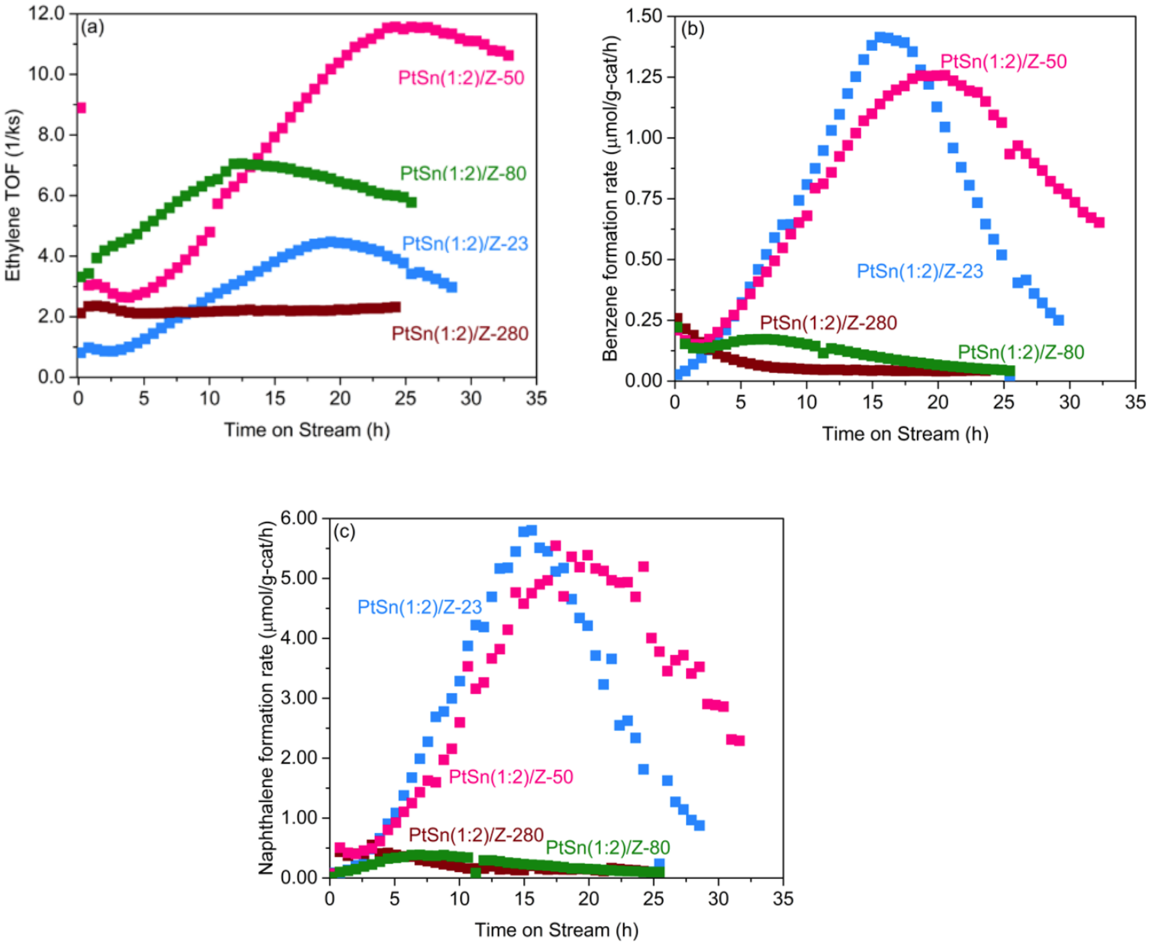

Figure 2.2. Effect of support acidity on (a) C_2H_4 TOF, (b) C_6H_6 formation rate, and (c) $C_{10}H_8$ formation rate. Reaction Conditions: CH_4 flow rate = 10.5 cm^3(STP)/min, T = 973 K, catalyst mass = 0.25 g.

To compare the activity of the catalysts toward the formation of aromatics, the formation rates of benzene and naphthalene per mass of catalyst are plotted in Figure 2.2b,c, respectively. The catalysts with the two most acidic supports, Pt-Sn/Z-23 and Pt-Sn/Z-50, showed the highest activity for both benzene and naphthalene production. The two less acidic catalysts, Pt-Sn/Z-80 and Pt-Sn/Z-280, were significantly less active for the production of aromatics and deactivated during time on stream. On the Pt-Sn/Z-23 catalyst, the maximum formation rate was achieved at 15 h, and on Pt-Sn/Z-50 it was achieved at around 20 h. For both catalysts, these time points were earlier than the time for maximum production of ethylene. The initially increasing and then decreasing volcano-shaped activity profile for the formation of all the products suggests the formation of a reactive “hydrocarbon pool” on the acidic surface during the earlier period of the reaction, similar to the hydrocarbon pool concept extensively studied and described in methanol to olefin (MTO) literature. It can be hypothesized that oligomerization of ethylene on the acid sites takes place together with interaction with the higher hydrocarbon structures of polyaromatics deposited in the pores.[22,23] After the maximum rate for ethylene formation is achieved, methane conversion is suppressed by deactivation.

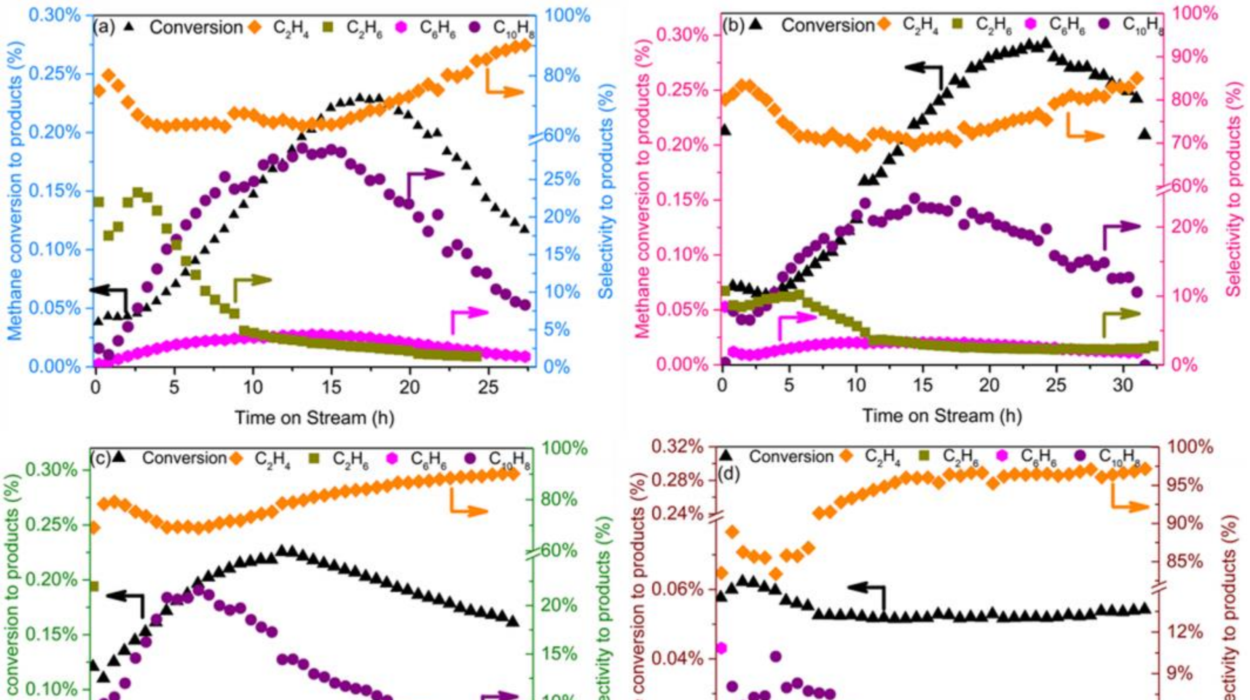

Figure 2.3. Effect of support acidity on methane conversion to detectable products and selectivities of (a) Pt-Sn/Z-23, (b) Pt-Sn/Z-50, (c) Pt-Sn/Z-80, and (d) Pt-Sn/Z-280. Reaction conditions: CH_4 flow rate = 10.5 cm^3(STP)/min, T = 973 K, catalyst mass = 0.25 g.

The methane conversion to detectable products (left axis) and the selectivities of the catalysts toward ethylene, ethane, benzene and naphthalene (right axis) over total hydrocarbon products excluding coke are plotted for each catalyst in Figure 2.3. The Pt-Sn/Z-50 catalyst showed the highest conversion, reaching approximately 0.30%, followed by the Pt-Sn/Z-23 catalyst. Conversion profiles of both catalysts were similar to the profiles for aromatics formation. The least acidic catalyst, Pt-Sn/Z-280, had low conversion, as indicated by its low ethylene TOF and aromatic formation rates. On all the catalysts, regardless of their activity, ethylene was the product with highest selectivity, and benzene formation was significantly lower during the entire time on stream. Over the two most active catalysts, there were visibly opposite trends between ethylene and naphthalene selectivities. During the initial periods of the reaction while ethylene formation was still increasing, its selectivity decreased in the favor of naphthalene formation, which subsequently decreased when the ethylene selectivity began to increase again. The benzene selectivities of the catalysts were lower than those of naphthalene, supporting the argument that naphthalene was formed from benzene.[24] The delay in the maximum rate of ethylene formation in comparison to that for aromatics can be explained by faster oligomerization of ethylene to benzene on the more acidic catalysts, in comparison to desorption of ethylene from the catalyst. After the maximum rate is reached, the catalyst begins to deactivate due to coke deposition. As seen in Table 2.3, quantification of the amount of coke deposited on spent zeolite-supported catalysts showed that the catalysts supported on more acidic supports had higher extents of coke deposition, while the Pt-Sn catalysts supported on Z-280 and the relatively inactive Pt/Z-280 catalyst had lower amounts of coke.

Table 2.3. Coke deposition on spent Pt-Sn/ZSM-5 catalysts, as determined by TGA.

Catalyst	**Coke Deposition (mmol C / g_{cat})**
Pt-Sn/Z-23	9.6
Pt-Sn/Z-50	8.9
Pt-Sn/Z-80	10
Pt-Sn/Z-280	6.5

In previously reported product formation rates, benzene was the main aromatic product, with selectivity higher than 60%.[3,25–28] However, for our catalysts with the two most acidic supports (Z-23 and Z-50), naphthalene was the major aromatic product, with formation rates up to 7 times higher than that of benzene. Over these two catalysts, when naphthalene formation reached its maximum rate, the selectivity to ethylene was 60%, that of naphthalene was 30%, and that of benzene was less than 5%. Furthermore, the total rate of carbon product formation (the sum of ethylene, benzene, and naphthalene) on the Pt-Sn/Z-50 catalyst was approximately 2.5 mmol of C/((mol of Pt) s), which is comparable to the calculated values of 0.1,[29] 0.2,[30] 0.3,[31] 0.6,[32] 0.7,[27] 2.1,[33] 9.2[34] and 15[35] mmolC/molMo-s from reported product formation rates for various Mo/H-ZSM-5 catalysts operated at 973 K and similar space velocities. To establish our own comparison, we prepared Mo/H-ZSM-5 catalysts with 0.58 and 4 wt% Mo, and we studied these catalysts for methane conversion at 973 K with 0.25 g of catalyst under 10.5 cm^3 (STP)/min methane flow. The total rates of carbon product formation for these catalysts were 1.8 and 0.3 mmol of C/((mol of Mo) s), respectively. To better illustrate this comparison, Figure 2.4a−c displays the rate of carbon product formation from ethylene, benzene, and naphthalene, respectively, on the 0.58 wt% Pt-Sn/Z-50, 0.58 wt% Mo/Z-50, and 4 wt% Mo/Z-50 catalysts. The total rate of carbon product formation on each catalyst is shown in Figure 2.4d. The rates in Figure 2.4 are normalized per Pt atom or per Mo atom in the catalyst.

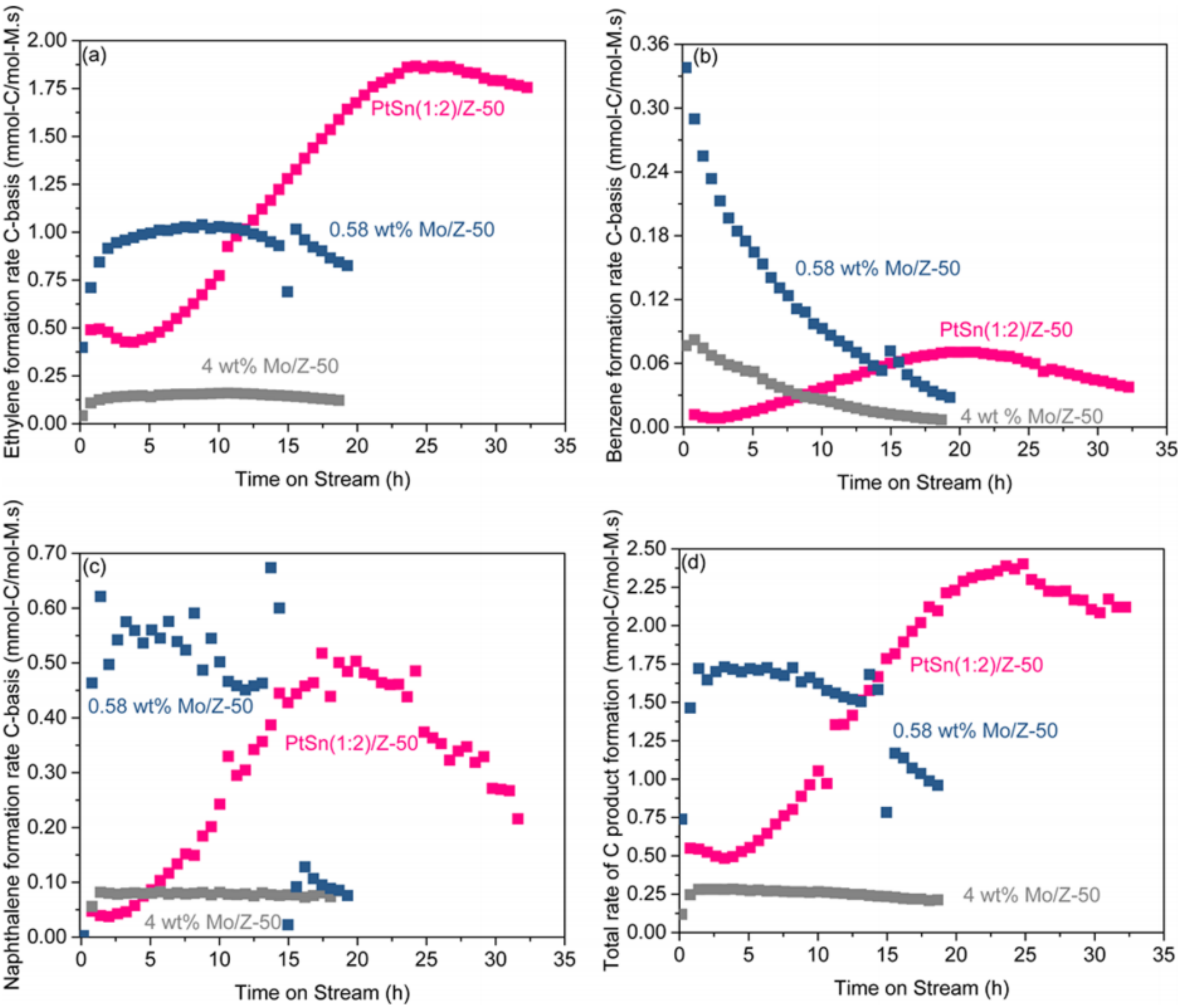

Figure 2.4. Rate of carbon formation from (a) ethylene, (b) benzene, and (c) naphthalene on the 0.58 wt% Pt-Sn/Z-50, 0.58 wt% Mo/Z-50, and 4 wt% Mo/Z-50 catalysts. (d) Total rate of carbon product formation on each catalyst. Reaction conditions: CH_4 flow rate = 10.5 cm^3 (STP)/min, T = 973 K, catalyst mass = 0.25 g.

2.4 Conclusions

In this chapter, we showed that Pt-Sn catalysts supported on H-ZSM-5 can be employed in methane conversion under nonoxidative conditions. Pt-Sn/H-ZSM5 catalysts with SiO_2:Al_2O_3 = 280 showed higher ethylene TOF with improved carbon balance in comparison to SiO_2-supported catalysts. When the acidity of the zeolite support is varied, a bifunctional catalyst can be obtained that forms benzene with a higher rate by conversion of ethylene on acidic sites. Additionally, Pt-

Sn catalysts supported on zeolites with SiO_2:Al_2O_3 = 23 and 50 produce significant amounts of naphthalene. The total rate of carbon production in the observed products (i.e., the sum of ethylene + benzene + naphthalene) of the Pt-Sn/Z-50 catalyst is comparable with those of state-of-the-art Mo/H-ZSM-5 catalysts reported in the literature and prepared in this study.

2.5 References

(1) Xu, Y.; Lin, L. Recent Advances in Methane Dehydro-Aromatization over Transition Metal Ion-Modified Zeolite Catalysts under Non-Oxidative Conditions. *Appl. Catal. A Gen.* **1999**, *188* (1–2), 53–67.

(2) Karakaya, C.; Kee, R. J. Progress in the Direct Catalytic Conversion of Methane to Fuels and Chemicals. *Progress in Energy and Combustion Science*. Elsevier Ltd July 1, 2016, pp 60–97.

(3) Shu, Y.; Ichikawa, M. Catalytic Dehydrocondensation of Methane towards Benzene and Naphthalene on Transition Metal Supported Zeolite Catalysts: Templating Role of Zeolite Micropores and Characterization of Active Metallic Sites. In *Catalysis Today*; 2001; Vol. 71, pp 55–67.

(4) Ma, S.; Guo, X.; Zhao, L.; Scott, S.; Bao, X. Recent Progress in Methane Dehydroaromatization: From Laboratory Curiosities to Promising Technology. *Journal of Energy Chemistry*. Elsevier B.V. 2013, pp 1–20.

(5) Shu, Y.; Ma, D.; Xu, L.; Xu, Y.; Bao, X. Methane Dehydro-Aromatization over Mo/MCM-22 Catalysts: A Highly Selective Catalyst for the Formation of Benzene. *Catal. Letters* **2000**, *70* (1–2), 67–73.

(6) Wang, L.; Tao, L.; Xie, M.; Xu, G.; Huang, J.; Xu, Y. Dehydrogenation and Aromatization of Methane under Non-Oxidizing Conditions. *Catal. Letters* **1993**, *21* (1), 35–41.

(7) Chen, L. Y.; Lin, L.; Xu, Z.; Li, X.; Zhang, T. Dehydro-Oligomerization of Methane to Ethylene and Aromatics over Molybdenum/HZSM-5 Catalyst. *J. Catal.* **1995**, *157* (1), 190–200.

(8) Wang, D.; Lunsford, J. H.; Rosynek, M. P. Catalytic Conversion of Methane to Benzene over Mo/ZSM-5. *Top. Catal.* **1996**, *3* (3–4), 289–297.

(9) Weckhuysen, B. M.; Wang, D.; Rosynek, M. P.; Lunsford, J. H. Catalytic Conversion of Methane into Aromatic Hydrocarbons over Iron Oxide Loaded ZSM-5 Zeolites. *Angew. Chemie (International Ed. English)* **1997**, *36* (21), 2374–2376.

(10) Wang, L.; Ohnishi, R.; Ichikawa, M. Selective Dehydroaromatization of Methane toward Benzene on Re/HZSM-5 Catalysts and Effects of CO/CO2 Addition. *J. Catal.* **2000**, *190* (2), 276–283.

(11) Weckhuysen, B. M.; Wang, D.; Rosynek, M. P.; Lunsford, J. H. Conversion of Methane to Benzene over Transition Metal Ion ZSM-5 Zeolites: I. Catalytic Characterization. *J. Catal.* **1998**, *175* (2), 338–346.

(12) Guo, X.; Fang, G.; Li, G.; Ma, H.; Fan, H.; Yu, L.; Ma, C.; Wu, X.; Deng, D.; Wei, M.; et al. Direct, Nonoxidative Conversion of Methane to Ethylene, Aromatics, and Hydrogen. *Science* **2014**, *344* (6184), 616–619.

(13) Belgued, M.; Pareja, P.; Amariglio, A.; Amariglio, H. Conversion of Methane into Higher Hydrocarbons on Platinum. *Nature* **1991**, *352* (6338), 789–790.

(14) Mielczarski, E.; Monteverdi, S.; Amariglio, A.; Amariglio, H. Direct Conversion of Methane to Higher Alkanes by Platinum Loaded Zeolites. *Appl. Catal. A, Gen.* **1993**, *104* (2), 215–228.

(15) Xu, Y.; Liu, S.; Guo, X.; Wang, L.; Xie, M. Methane Activation without Using Oxidants over Mo/HZSM-5 Zeolite Catalysts. *Catal. Letters* **1994**, *30* (1–4), 135–149.

(16) Chen, L.; Lin, L.; Xu, Z.; Zhang, T.; Li, X. Promotional Effect of Pt on Non-Oxidative Methane Transformation over Mo-HZSM-5 Catalyst. *Catal. Letters* **1996**, *39* (3–4), 169–172.

(17) Pinglian, T.; Zhusheng, X.; Tao, Z.; Laiyuan, C.; Liwu, L. Aromatization of Methane over Different Mo-Supported Catalysts in the Absence of Oxygen. *React. Kinet. Catal. Lett.* **1997**, *61* (2), 391–396.

(18) Tshabalala, T. E.; Coville, N. J.; Scurrell, M. S. Dehydroaromatization of Methane over Doped Pt/Mo/H-ZSM-5 Zeolite Catalysts: The Promotional Effect of Tin. *Appl. Catal. A Gen.* **2014**, *485*, 238–244.

(19) Tshabalala, T. E.; Coville, N. J.; Anderson, J. A.; Scurrell, M. S. Dehydroaromatization of Methane over Sn-Pt Modified Mo/H-ZSM-5 Zeolite Catalysts: Effect of Preparation Method. *Appl. Catal. A Gen.* **2015**, *503*, 218–226.

(20) Gerceker, D.; Motagamwala, A. H.; Rivera-Dones, K. R.; Miller, J. B.; Huber, G. W.; Mavrikakis, M.; Dumesic, J. A. Methane Conversion to Ethylene and Aromatics on PtSn Catalysts. *ACS Catal.* **2017**, *7* (3), 2088–2100.

(21) Tessonnier, J. P.; Louis, B.; Rigolet, S.; Ledoux, M. J.; Pham-Huu, C. Methane Dehydro-Aromatization on Mo/ZSM-5: About the Hidden Role of Brønsted Acid Sites. *Appl. Catal. A Gen.* **2008**, *336* (1–2), 79–88.

(22) Haw, J. F.; Song, W.; Marcus, D. M.; Nicholas, J. B. The Mechanism of Methanol to Hydrocarbon Catalysis. *Acc. Chem. Res.* **2003**, *36* (5), 317–326.

(23) White, J. L. Methanol-to-Hydrocarbon Chemistry: The Carbon Pool (r)Evolution. *Catalysis Science and Technology*. Royal Society of Chemistry 2011, pp 1630–1635.

(24) Carlson, T. R.; Jae, J.; Huber, G. W. Mechanistic Insights from Isotopic Studies of Glucose Conversion to Aromatics over ZSM-5. *ChemCatChem* **2009**, *1* (1), 107–110.

(25) Derouane-Abd Hamid, S. B.; Anderson, J. R.; Schmidt, I.; Bouchy, C.; Jacobsen, C. J. H.; Derouane, E. G. Effect of the Activation Procedure on the Performance of Mo/H-MFI Catalysts for the Non-Oxidative Conversion of Methane to Aromatics. *Catal. Today* **2000**, *63* (2–4), 461–469.

(26) Lacheen, H. S.; Iglesia, E. Stability, Structure, and Oxidation State of Mo/H-ZSM-5 Catalysts during Reactions of CH4 and CH4-CO2 Mixtures. *J. Catal.* **2005**, *230* (1), 173–185.

(27) Xu, Y.; Song, Y.; Suzuki, Y.; Zhang, Z. G. Mechanism of Fe Additive Improving the Activity Stability of Microzeolite-Based Mo/HZSM-5 Catalyst in Non-Oxidative Methane Dehydroaromatization at 1073 K under Periodic CH4-H2switching Modes. *Catal. Sci.*

Technol. **2014**, *4* (10), 3644–3656.

(28) Song, Y.; Xu, Y.; Suzuki, Y.; Nakagome, H.; Zhang, Z. G. A Clue to Exploration of the Pathway of Coke Formation on Mo/HZSM-5 Catalyst in the Non-Oxidative Methane Dehydroaromatization at 1073 K. *Appl. Catal. A Gen.* **2014**, *482*, 387–396.

(29) Liu, S.; Dong, Q.; Ohnishi, R.; Ichikawa, M. Unique Promotion Effect of CO and CO2 on the Catalytic Stability for Benzene and Naphthalene Production from Methane on Mo/HZSM-5 Catalysts. *Chem. Commun.* **1998**, No. 11, 1217–1218.

(30) Solymosi, F.; Erdöhelyi, A.; Szöke, A. Dehydrogenation of Methane on Supported Molybdenum Oxides. Formation of Benzene from Methane. *Catal. Letters* **1995**, *32* (1–2), 43–53.

(31) Ohnishi, R.; Liu, S.; Dong, Q.; Wang, L.; Ichikawa, M. Catalytic Dehydrocondensation of Methane with CO and CO2 toward Benzene and Naphthalene on Mo/HZSM-5 and Fe/Co-Modified Mo/HZSM-5. *J. Catal.* **1999**, *182* (1), 92–103.

(32) Fila, V.; Bernauer, M.; Bernauer, B.; Sobalik, Z. Effect of Addition of a Second Metal in Mo/ZSM-5 Catalyst for Methane Aromatization Reaction under Elevated Pressures. *Catal. Today* **2015**, *256* (P2), 269–275.

(33) Burns, S.; Hargreaves, J. S. J.; Pal, P.; Parida, K. M.; Parija, S. The Effect of Dopants on the Activity of MoO3/ZSM-5 Catalysts for the Dehydroaromatisation of Methane. *Catal. Today* **2006**, *114* (4 SPEC. ISS.), 383–387.

(34) Shu, Y.; Xu, Y.; Wong, S. T.; Wang, L.; Guo, X. Promotional Effect of Ru on the Dehydrogenation and Aromatization of Methane in the Absence of Oxygen over Mo/HZSM-5 Catalysts. *J. Catal.* **1997**, *170* (1), 11–19.

(35) Shu, Y.; Ohnishi, R.; Ichikawa, M. Pressurized Dehydrocondensation of Methane toward Benzene and Naphthalene on Mo/HZSM-5 Catalyst: Optimization of Reaction Parameters and Promotion by CO2 Addition. *J. Catal.* **2002**, *206* (1), 134–142.

Chapter 3. Structural Characterization of Supported Multi-Metallic Catalysts by X-Ray Absorption Spectroscopy[a,b]

3.1 Introduction

The electronic and structural environments of supported nanoparticles are fundamental to understanding the catalytic performance of heterogeneous materials. This is particularly the case for bimetallic catalysts, in which close interaction of the two metals is usually vital to the improvement of catalytic activity when compared to the monometallic catalysts. Various spectroscopic techniques can be used to explore the local environment of such catalysts, including infrared (IR) spectroscopy, x-ray photoelectron spectroscopy (XPS), and x-ray absorption spectroscopy (XAS). In contrast to diffraction and other spectroscopic techniques, XAS allows the possibility to simultaneously determine both electronic and structural properties of a bulk material in crystalline and amorphous samples under vacuum and realistic reaction conditions.

XAS techniques evaluate the transitions that take place following the excitation of a core electron by an x-ray beam. For an excitation event to occur, the incident x-ray beam must have an energy that is at least equal to the binding energy of a core-level electron. When this happens, a sharp rise in x-ray absorption is observed, which signals the promotion of the core-level electron

---

[a] This chapter has been adapted from the following publications: (1) Ball, M.; Wesley, T.; Rivera-Dones, K.; Huber, G.; Dumesic, J. "Amination of 1-Hexanol on Bimetallic AuPd/TiO_2 Catalysts" *Green Chem* 20 (2018) 4695-4709. (2) Ball, M.; Rivera-Dones, K.; Stangland, E.; Mavrikakis, M.; Dumesic, J. "Hydrodechlorination of 1,2-dichlorethane on Supported AgPd Catalysts". *J Catal* 370 (2019) 241-250. (3) Zhang, L.; Ball, M.; Rivera-Dones, K.; Wang, S.C.; Kuech, T.; Huber, G.; Hermans, I.; Dumesic, J. "Synthesis Gas Conversion over Molybdenum-Based Catalysts Promoted by Transition Metals". *ACS Catal.* 10 (2020) 365-374. (4) Ball, M.R.; Rivera-Dones, K.R., Gilcher, E.B.; Ausman, S.A.; Hullfish, C.W.; Lebrón, E.R., Dumesic, J.A. "AgPd and CuPd catalysts for selective hydrogenation of acetylene" *ACS Catal*. 10 (2020) 8567–8581

[b] Author contributions: M.B., T.W., L.Z., S.C.W., E.B.G., S.A.A., C.W.H., and E.R.L performed reactivity and characterization experiments for their corresponding publications. K.R.R.D performed XANES and EXAFS experiments, data collection and analyses for all publications. All authors contributed to manuscript development for their respective publications.

to the continuum. This sudden rise in absorption is deemed an *absorption edge*. To accomplish these excitations, XAS requires intense and continuously tunable x-ray beams that can only be achieved at synchrotron facilities, where x-rays can be tuned between 100 eV to 10^4 eV to target the adsorption edge corresponding to core electrons at particular shells of specific chemical elements. A well-defined absorption edge exists for the different electron orbitals, and the nomenclature used for each edge is based on the quantum numbers corresponding to the target orbitals. Each edge is identified by a single letter and index number, where the letter refers to the first quantum number n (with K, L, and M being used for $n = 1$, 2, and 3, respectively) and the index number refers to the second quantum number l, (with 1 used for $l = 0$, and 2 and 3 used for $l = 1$)[1].

The x-ray absorption spectrum obtained via XAS generally encompasses two main regions: X-ray absorption near-edge structure (XANES) and extended x-ray absorption fine structure (EXAFS). The XANES region typically evaluates an area within ~30-50 eV of the adsorption edge and contains features caused by the electronic and magnetic structures, as well as the geometry and symmetry, around absorbing atoms.[1] As a result, XANES is sensitive to oxidation state, types of ligands, and coordination chemistry, and can be particularly useful for fingerprinting or identifying an unknown substance. The EXAFS region is typically considered to begin at least 50 eV or more above the edge energy and can extend for hundreds of eV further. In this region, EXAFS spectra contain oscillations that occur as a result of interference between waves of ejected photoelectrons and those reflected from neighboring atoms.[2] Therefore, the EXAFS region can be used to determine the local geometry of the absorbing atoms with respect to the atoms in their immediate vicinity. Specifically, parameters such as average coordination number and nearest-neighbor distance can be extracted from the Fourier-transformed EXAFS spectra.

Our group has traditionally used XAS measurements to evaluate the structure and composition of bimetallic and multi-metallic catalysts synthesized via specialized techniques, including controlled surface reactions (CSR) and atomic layer deposition (ALD). Synthesis of bimetallic catalysts by CSR involves selectively depositing a metal of interest onto a reduced parent catalyst by means of an organometallic precursor that, ideally, only reacts with the metal already present on the parent material while having minimal interaction with the catalyst support. This technique has been consistently shown to yield bimetallic catalysts with narrow distributions of particle size and composition, and has allowed clear elucidation of the nature of catalytically active sites in numerous reactive systems.[3–9] Similarly, catalyst synthesis by ALD has proven advantageous in the preparation of materials with high surface area and high metal dispersion by exploiting the self-limiting feature of the technique in order to carefully control the location of metal and metal oxide sites on catalytic supports.[10,11] Additionally, bimetallic catalysts shown to have high activity and selectivity have also been prepared by ALD, whereby the location of each metal can be precisely controlled.[12–15]

In this chapter, we explore the use of XANES and EXAFS measurements to understand the chemical and structural environment of bimetallic Pd-containing catalysts synthesized by CSR and Mo-based multi-metallic catalysts created via ALD. The information gained from the XAS characterization of these catalytic systems, combined with additional techniques such as infrared spectroscopy and CO chemisorption, supports a fundamental understanding of activity and selectivity patterns observed in amination[6], hydrodechlorination[16], hydrogenation[17], and synthesis gas conversion[11] reactions.

3.2 Experimental Methods

XAS measurements were taken at MRCAT Beamlines 10-BM and 10-ID of the Advanced Photon Source at Argonne National Laboratory. Measurements were taken at the Au-L_3 edge (11919 eV) and at the K edge for Ni (8333 eV), Cu (8979 eV), Mo (20000 eV), Ag (22514 eV), and Pd (24350 eV). Prior to analysis, catalyst samples were pressed into wafers inside a stainless-steel sample holder and placed into a quartz tube sealed on both ends by Ultra-Torr fittings (Swagelok) equipped with Kapton windows to allow for gas flow through the cell during pretreatment and analysis. To calibrate edge energies, spectra of the appropriate foils were taken for each sample at each edge of interest. Data analysis for all samples was performed using the Demeter software package.

In the study for the amination of 1-hexanol, Au/TiO_2, Pd/TiO_2, and AuPd/TiO_2 catalyst samples were flushed with He (Airgas) once they were mounted onto the quartz tubes prior to analysis. Spectra were taken in transmission mode at room temperature and under inert flow. XANES fitting was performed using a linear combination of experimental standards within the range of -20 to +30 eV of the corresponding edge energy. The experimental standards used were Au and Pd foils, Au_2O_3 powder, and PdO powder. EXAFS data fitting was performed over an R-range of 1.4 – 3.4 Å and a k-range of 3 – 10 $Å^{-1}$, with amplitude reduction factors (S_0^2) of 0.82 and 0.86 as determined by fitting reference foil spectra for Au and Pd, respectively.

Supported Ag, Pd, and AgPd catalysts used in the hydrodechlorination of 1,2-dichloroethane were reduced *in-situ* using 3% H_2 in He (Airgas) for 30 min at 473 K, purged with He, and allowed to cool to room temperature under inert flow prior to analysis. Spectra at the corresponding edges were taken in transmission mode at room temperature and under inert flow. Data fitting was performed over an R-range of 1.6 – 3.2 Å and a k-range of 2.8 – 13.5 $Å^{-1}$, with

S_0^2 = 0.88 for Ag and S_0^2 = 0.86 for Pd as determined by fitting the corresponding reference foil spectra.

Mono- and bimetallic catalysts used for acetylene hydrogenation were pre-treated either by flowing He at room temperature or by *in-situ* reduction at 473 K in 3% H_2/He. A select group of catalysts was also analyzed after being exposed to reaction conditions at 313 K for 24 hr. The "post-reaction" catalysts were recovered from the reactor and packed into the appropriate sample holders using an inert glove box to avoid exposure to ambient air. XANES fitting was performed using a linear combination of experimental standards within the range of -20 to +30 eV of the corresponding edge energy. The experimental standards used were Ag, Cu, and Pd foils as well as Ag_2O, CuO, and PdO powders. EXAFS data fitting was performed over an R-range of 1.6 – 3.6 Å and a k-range of 2.8 – 12.3 $Å^{-1}$ at the Ag edge, an R-range of 1.1 – 2.8 Å and k-range of 2.4 – 10.8 $Å^{-1}$ at the Cu edge, and an R-range of 1.1 – 2.8 Å and k-range of 2.4 – 11.6 $Å^{-1}$ at the Pd edge. Fits of the reference foil spectra were used to determine amplitude reduction factors of 0.74, 0.89, and 0.86 for Cu, Ag, and Pd, respectively.

Ni- and Mo-containing catalysts used in synthesis gas conversion were pre-treated *in situ* under 3% H_2/He flow and cooled to room temperature under inert flow prior to analysis. XANES spectra were collected in transmission mode under inert flow at room temperature. Fitting was performed using a linear combination of experimental standards within the range of -20 to +30 eV of the corresponding edge energy. The experimental standards used were Mo and Ni foils, as well as powdered MoO_2, MoO_3, and NiO.

3.3 Results and Discussion

This chapter will present various case studies to discuss the use of XAS measurements as a characterization tool for specially synthesized multi-metallic catalysts developed using CSR and ALD methods within our group over recent years.

3.3.1 Au-Pd Catalysts for the Amination of 1-Hexanol

In the first study to be discussed herein, titania-supported AuPd catalysts were synthesized via CSR and studied for the direct amination of 1-hexanol.[6] In this study, bimetallic AuPd catalysts were found to exhibit higher hexanol conversion site-time yields than the monometallic catalysts, with the formation of primary species enhanced as Pd is incrementally added to the parent Au catalyst. XAS measurements were used in this study to understand the chemical and structural effects of depositing Pd on Au. Table 3.1 shows the distribution of oxidation states for Au and Pd in the reduced-then-passivated monometallic and bimetallic catalysts, as determined by a linear combination analysis of XANES spectra from the corresponding standards. These results show that Au exists primarily in a metallic state in all Au-containing catalysts. In contrast, the amount of metallic Pd appears to increase with decreasing Pd:Au loading ratios. Specifically, the Pd^0:Pd^{+2} ratio increases from 1:1 for the monometallic Pd catalyst to 9:1 for the $AuPd_{0.23}/TiO_2$ catalyst. Unfortunately, the low Pd content of the $AuPd_{0.06}/TiO_2$ catalyst prevented a reliable analysis of the spectra for the Pd edge. The presence of Pd^{+2} species is characteristic of oxide formation in the surface layer of the passivated catalyst. Therefore, the data suggests that Pd favors subsurface migration with decreasing Pd loading, which also explained the low dispersions measured by associated CO chemisorption studies.

Table 3.1. Fractional composition of oxidation states for amination catalysts as determined by XANES measurements at the Pd-K and Au-L_3 edges.[a]

Catalyst	Pd^0	Pd^{+2}	Au^0	Au^{+3}
Pd/TiO_2	0.46	0.54	N/A	N/A
$AuPd_{0.67}/TiO_2$	0.72	0.28	0.96	0.04
$AuPd_{0.55}/TiO_2$	0.73	0.27	0.97	0.03
$AuPd_{0.23}/TiO_2$	0.90	0.10	0.97	0.03
$AuPd_{0.06}/TiO_2$[b]	--	--	1.00	0.00
Au/TiO_2	N/A	N/A	0.96	0.04

[a] Linear combination fits have ± 2% error.

[b] Reliable speciation limited by low Pd loading.

EXAFS results for the Au and Pd edges are shown in Table 3.2. All bimetallic catalysts show to have Pd-Pd coordination numbers below 2 and Pd-Au coordination numbers above 8, thus suggesting that Pd is well diluted in the Au and that monometallic Pd particles have a negligible presence in the bimetallic catalysts. Further evidence for the existence of well-diluted Pd in Au can be found in the similar coordination numbers observed for the Pd-Au and Au-Pd paths across all bimetallic catalysts. Additionally, Au-Pd coordination appears to increase with increasing Pd content, as seen by results from the Au-L_3 edge. The intimate contact between Au and Pd species in the bimetallic alloys was found to enhance catalytic activity for the gas-phase amination of hexanol due to a combination of electronic and ensemble effects, as verified by CO-FTIR.

Table 3.2. EXAFS fitting results for amination catalysts at the Pd-K and Au-L$_3$ edges.[a]

Catalyst	Pd K-Edge				Au L$_3$-Edge			
	Scatter Path	**N[b]**	**R[c] (Å)**	**R-factor**	**Scatter Path**	**N[b]**	**R[c] (Å)**	**R-factor**
Pd/TiO$_2$	Pd – Pd	5.4	2.73	0.006				
	Pd – O	2.3	1.92					
AuPd$_{0.67}$/TiO$_2$	Pd – Pd	1.6	2.86	0.015	Au – Au	9.1	2.85	0.039
	Pd – Au	11.0	2.80		Au – Pd	3.1	2.77	
	Pd – O	0.4	1.97		Au – O	0.2	1.97	
AuPd$_{0.55}$/TiO$_2$	Pd – Pd	1.0	2.75	0.002	Au – Au	10.0	2.85	0.051
	Pd – Au	8.6	2.82		Au – Pd	2.2	2.80	
	Pd – O	1.0	2.01		Au – O	0.6	1.98	
AuPd$_{0.23}$/TiO$_2$	Pd – Pd	1.0	2.63	0.057	Au – Au	9.9	2.84	0.061
	Pd – Au	10.8	2.81		Au – Pd	0.7	2.82	
	Pd – O	0.6	2.04		Au – O	0.5	1.90	
AuPd$_{0.06}$/TiO$_2$	Pd – Pd	Unable to fit Pd-edge due to high noise level from low Pd loading			Au – Au	10.0	2.82	0.035
	Pd – Au				Au – Pd	0.6	2.85	
	Pd – O				Au – O	0.4	1.91	
Au/TiO$_2$					Au – Au	8.8	2.85	0.015
					Au – O	0.2	2.06	

[a] The Debye-Waller factor for all measurements is $\sigma^2 = 0.008$ Å^2.
[b] Coordination number. Estimated uncertainty is ± 20%.
[c] Distance between absorber and back-scatterer. Estimated uncertainty is ± 0.02 Å.

3.3.2 Ag-Pd Bimetallic Catalysts for the Hydrodechlorination of 1,2-dichloroethane

The importance of structural characterization by XAS measurements was also highlighted in a recent study on the hydrodechlorination of 1,2-dichloroethane over supported AgPd catalysts. In this study, Ag, Pd, and AgPd catalysts were synthesized over SiO$_2$, TiO$_2$, and high-temperature treated carbon (HTTC) using CSR techniques to evaluate the influence of catalyst support on bimetallic nanoparticle formation.[16] EXAFS analyses were performed on catalysts following an *in situ* reduction at 473 K, and results are shown in Table 3.3 below. While measurements were taken at both the Ag and Pd K-edges, the close proximity of these edge energies leads to similar scattering patterns for the Ag-Pd and Ag-Ag paths, thus inhibiting our ability to distinguish the identity of the back-scattering atom. Consequently, the results provided here are for Ag-M and Pd-M scattering paths, which include both neighboring Ag and Pd atoms. As a result, these measurements can provide information about the extent of bimetallic nanoparticle formation by evaluating the distance between the absorber and back-scattering atoms, R. The expected radii for the nearest neighboring atom in bulk Ag and Pd samples are $R_{Ag\text{-}Ag}$ = 2.89 Å and $R_{Pd\text{-}Pd}$ = 2.75 Å, respectively. Therefore, an intermediate R value is indicative of a mixture of Ag and Pd atoms.[18,19]

Table 3.3. EXAFS fitting results for hydrodechlorination catalysts at the Ag and Pd K-edges.

Catalyst	Scatter Path	N[a]	R[b] (Å)	σ^2 (Å^2)	R-factor
Ag/SiO_2	Ag – M	3.4	2.79	0.010	0.079
$AgPd_{1.3}/SiO_2$	Ag – M Pd – M	4.5 6.0	2.77 2.73	0.010	0.046 0.017
Pd/SiO_2	Pd – M	9.4	2.74	0.006	0.009
Ag/HTTC	Ag – M	9.4	2.87	0.010	0.010
$AgPd_{0.6}$/HTTC	Ag – M Pd – M	10.0 10.6	2.85 2.76	0.010	0.009 0.008
Pd/HTTC	Pd – M	10.9	2.74	0.006	0.004
Ag/TiO_2	Ag – M	9.6	2.86	0.010	0.021
$AgPd_{0.35}/TiO_2$[c]	Ag – M Pd – M	9.4 9.9	2.85 2.84	0.010	0.021 0.046
$AgPd_{0.5}/TiO_2$	Ag – M Pd – M	9.1 11.1	2.84 2.82	0.010	0.021 0.011
$AgPd_{1.9}/TiO_2$	Ag – M Pd – M	10.5 10.1	2.83 2.79	0.010	0.007 0.017
Pd/TiO_2	Pd – M	8.3	2.74	0.006	0.031

[a] Coordination number. Estimated uncertainty is ± 20%.
[b] Distance between absorber and back-scatterer. Estimated uncertainty is ± 0.02 Å.
[c] Spectra for $AgPd_{0.35}/TiO_2$ collected without H_2 pretreatment.

In the TiO_2 supported catalysts, a decrease in the value of R follows an increase in the palladium concentration of the bimetallic samples, which is in line with the lower value of R for bulk Pd. Perhaps more importantly, the R values for the Ag-M and Pd-M paths are quite similar for the $AgPd_{0.35}/TiO_2$ and $AgPd_{0.5}/TiO_2$ catalysts, suggesting that Ag and Pd are well mixed within the bimetallic nanoparticle structure. With a significant increase in palladium content, the $AgPd_{1.9}/TiO_2$ catalyst appears to have more segregation between the Ag and Pd phases. A similar observation can be made for the $AgPd_{1.3}/SiO_2$ catalyst. Furthermore, the carbon-supported bimetallic catalyst shows an even larger difference in the R values for the Ag-M and Pd-M paths than do the higher loading TiO_2 and SiO_2 catalysts. These results suggest that the $AgPd_{0.6}$/HTTC catalyst has the highest degree of segregation between the Ag and Pd, as evidenced by the $R_{Ag\text{-}M} = 2.85$ and $R_{Pd\text{-}M} = 2.76$ values each being closest to the corresponding bulk metal distances.

EXAFS data, in collaboration with other characterization techniques like CO chemisorption and FTIR, can therefore be used to highlight significant differences in the extent of bimetallic nanoparticle formation as an effect of catalyst support in the AgPd catalysts. Associated reactivity studies showed that the $AgPd/TiO_2$ catalysts containing isolated Pd species were found to be up to 97% selective to ethylene. In contrast, the $AgPd/SiO_2$ catalyst was found to be 91% selective to ethane. It was therefore concluded that isolated Pd species, such as those formed on TiO_2, are more active and selective to ethylene than contiguous Pd species, which are selective to ethane and are more easily formed on SiO_2.

3.3.3 Ag-Pd and Cu-Pd Catalysts for Acetylene Hydrogenation

Additional work further evaluating the use of AgPd catalysts for reactive systems was conducted on the selective hydrogenation of acetylene in ethylene-rich streams.[17] In conjunction with CuPd catalysts, the AgPd catalysts were evaluated for their ability to selectively hydrogenate acetylene to ethylene while preventing over-hydrogenation to ethane. To this purpose, AgPd and CuPd catalysts were synthesized on TiO_2 and SiO_2 supports using the CSR technique. Table 3.4 shows XANES data for these catalysts and their monometallic counterparts under various pretreatment conditions, including a He purge at room temperature, a reduction under 3% hydrogen at 473 K, and following a 24 h exposure to reaction conditions at 313 K.

Table 3.4. Fractional compositions of oxidation states for acetylene hydrogenation catalysts following various pretreatments, as determined from XANES measurements at the Ag, Pd, and Cu K-edges.

Catalyst	Pretreatment	Ag^0	Ag^{+1}	Pd^0	Pd^{+2}	Cu^0	Cu^{+2}
Ag/TiO_2	None	0.83	0.17				
	Reduced	1.00	0.00				
Ag/SiO_2	None	0.77	0.23				
	Reduced	0.55	0.45				
$AgPd_{0.64}/TiO_2$	None	1.00	0.00	0.94	0.06		
	Reduced	0.91	0.09	a	a		
	Post-Reaction	1.00	0.00	1.00	0.00		
$AgPd_{0.15}/SiO_2$	None	0.85	0.15	0.46	0.54		
	Reduced	0.67	0.33	a	a		
	Post-Reaction	0.66	0.34	0.60	0.40		
Pd/TiO_2	None			0.48	0.52		
	Reduced			0.34	0.66		
	Post-Reaction			0.83	0.17		
Pd/SiO_2	None			0.82	0.18		
	Reduced			0.79	0.21		
	Post-Reaction			0.91	0.09		
$CuPd_{0.08}/TiO_2$	None			0.11	0.89	0.00	1.00
	Reduced			0.45	0.55	0.12	0.88
$CuPd_{0.02}/TiO_2$	None			0.00	1.00	0.00	1.00
	Reduced			0.43	0.57	0.38	0.62
	Post-Reaction			0.68	0.32	--	--
$CuPd_{0.09}/SiO_2$	None			0.11	0.89	0.05	0.95
	Reduced			0.44	0.56	0.54	0.46
	Post-Reaction			0.56	0.44	--	--
Cu/TiO_2	None					0.03	0.97
	Reduced					0.08	0.93
Cu/SiO_2	None					0.24	0.76
	Reduced					0.00	1.00

[a] Spectra too noisy to allow for reliable fitting at the Pd edge

The results in Table 3.4 show that catalysts were more easily reduced on the TiO_2 support in comparison to SiO_2. In addition, it appears that the addition of Pd aids in further reducing the parent Ag or Cu metal in the bimetallic catalysts over both supports. It is also worthwhile to note that Pd does not appear to be fully reduced in any catalyst following the H_2 treatment at 473 K. However, the concentration of metallic Pd does appear to increase after a 24 h exposure to the hydrocarbon/hydrogen feed under reaction conditions. This result aligns well with reactivity experiments, where an activation time of up to 24 hrs was observed for bimetallic catalysts to achieve steady state.

EXAFS results for the AgPd and CuPd catalysts are summarized in Table 3.5 and Table 3.6, respectively. We note that the monometallic Pd catalysts shown are the same for both bimetallic catalyst sets, and the corresponding fitting results were duplicated across the tables for easier referencing. It can be observed from the Pd edge that the Pd/TiO_2 catalyst has lower total coordination numbers than the SiO_2-supported monometallic catalyst across all pretreatment conditions. This finding supports the idea that metal-TiO2 interactions lead to some metal being buried at the support interface, as determined by associated CO chemisorption measurements.

Table 3.5. EXAFS fitting results for Pd and AgPd catalysts used in acetylene hydrogenation analyzed at the Ag and Pd K-edges following various pretreatments.

Catalyst	**Pretreatment**	**Scatter Path**[a]	**N**[b]	**R**[c] **(Å)**	**σ^2 (Å^2)**	**R-factor**
$AgPd_{0.64}/TiO_2$	None	Ag – M	7.9	2.86	0.007	0.060
		Pd – M	9.3	2.80		0.022
	Reduced	Ag – M	5.3	2.84	0.007	0.075
	Post-Reaction	Ag – M	8.0	2.86	0.007	0.046
		Pd – M	8.0	2.84		0.089
$AgPd_{0.15}/SiO_2$	None	Ag – M	4.7	2.80	0.011	0.075
		Ag – O	0.4	2.23		
	Reduced	Ag – M	6.0	2.78	0.019	0.015
		Ag – O	1.3	2.17		
	Post-Reaction	Ag – M	5.2	2.77	0.017	0.028
		Ag – O	1.2	2.19		
		Pd – M	7.5	2.86	0.007	0.049
Pd/TiO_2	None	Pd – Pd	4.0	2.74	0.007	0.011
		Pd – O	2.7	1.79		
	Reduced	Pd – Pd	2.2	2.75	0.007	0.076
		Pd – O	3.3	2.00		
	Post-Reaction	Pd – Pd	6.7	2.75	0.007	0.053
Pd/SiO_2	None	Pd – Pd	11.2	2.74	0.007	0.013
	Reduced	Pd – Pd	11.5	2.73	0.007	0.013
	Post-Reaction	Pd – Pd	10.6	2.77	0.007	0.013

[a] First element in the path dictates the absorbing atom.

[b] Coordination number, uncertainty ± 15%

[c] Distance between absorber and back-scatterer. Estimated uncertainty is ± 5%.

Table 3.6. EXAFS fitting results for Pd and CuPd catalysts used in acetylene hydrogenation analyzed at the Cu and Pd K-edges following various pretreatments.

Catalyst	Pretreatment	Scatter Path	N[b]	R[c] (Å)	σ^2 (Å^2)	R-factor
CuPd$_{0.08}$/TiO$_2$	None	Cu – Cu Cu – O	0.8 3.6	2.48 1.95	0.007	0.035
		Pd – Pd Pd – O	2.0 2.7	2.74 2.00	0.007	0.081
	Reduced	Cu – Cu Cu – O	4.2 2.0	2.54 1.86	0.007	0.032
		Pd – Pd Pd – Cu	6.3 0.5	2.57 1.99	0.007	0.008
CuPd$_{0.02}$/TiO$_2$	None	Cu – Cu Cu – O	0.3 3.5	2.19 1.93	0.007	0.008
		Pd – Cu Pd – O	0.7 3.7	2.45 2.02	0.007	0.076
	Reduced	Cu – Cu Cu – O	5.7 2.1	2.53 1.81	0.007	0.061
		Pd – Pd Pd – Cu	4.8 0.8	2.55 1.98	0.007	0.033
	Post-Reaction	Pd – Pd Pd – Cu Pd – O	2.7 7.0 0.8	2.99 2.59 1.98	0.007	0.017
CuPd$_{0.09}$/SiO$_2$	None	Cu – Cu Cu – O	-- 3.1	-- 1.90	0.007	0.006
		Pd – Pd Pd – Cu Pd – O	-- 2.4 2.5	-- 2.56 2.00	0.007	0.046
	Reduced	Cu – Cu Cu – O	4.2 2.0	2.54 1.86	0.007	0.032
		Pd – Cu Pd – O	5.5 0.6	2.55 1.97	0.007	0.010
	Post-Reaction	Pd – Cu Pd – O	7.8 0.4	2.58 1.98	0.007	0.007
Pd/TiO$_2$	None	Pd – Pd Pd – O	4.0 2.7	2.74 1.79	0.007	0.011
	Reduced	Pd – Pd Pd – O	2.2 3.3	2.75 2.00	0.007	0.076
	Post-Reaction	Pd – Pd	6.7	2.75	0.007	0.053
Pd/SiO$_2$	None	Pd – Pd	11.2	2.74	0.007	0.013
	Reduced	Pd – Pd	11.5	2.73	0.007	0.013
	Post-Reaction	Pd – Pd	10.6	2.77	0.007	0.013

[a] First element in the path dictates the absorbing atom.

[b] Coordination number, uncertainty ± 15%

[c] Distance between absorber and back-scatterer. Estimated uncertainty is ± 5%.

In following with the lack of distinguishable scattering previously discussed for Ag-Ag and Ag-Pd paths, as well as the Pd-edge counterparts, due to the similarity in edge energies, results for the AgPd catalysts will be discussed in terms of overall coordination from each edge. As can be observed from Table 3.5, the $AgPd_{0.64}/TiO_2$ catalyst appears to have a higher coordination from the Pd edge than from the Ag edge when no pretreatment is performed on the catalyst. In contrast, similar coordination exists from both edges when the catalyst has been exposed to reaction conditions for 24 hrs. These results suggest that the metals in this catalyst originally have different average environments, and that, in accordance with associated CO chemisorption results, the catalytic surface is Ag enriched while Pd prefers to occupy subsurface sites. Moreover, the change in coordination following exposure to reaction conditions indicates that some degree of surface restructuring occurs through which some of the existent Pd is brought to the surface.

With regards to the CuPd catalysts, the results in Table 3.6 show that the Pd is well-dispersed in the Cu parent for the $CuPd_{0.02}/TiO_2$ and $CuPd_{0.09}/SiO_2$ catalysts, given the lack of Pd-Pd coordination for these catalysts without pretreatment. Once the catalysts are reduced, an increase in the Pd-Pd coordination is observed for the $CuPd_{0.02}/TiO_2$ and $CuPd_{0.08}/TiO_2$ catalysts, whereas no Pd-Pd coordination can be found for the $CuPd_{0.09}/SiO_2$ catalyst. Therefore, it can be inferred that the catalyst structure changes more drastically for TiO_2-supported catalysts than it does for those on a SiO_2 support following pretreatment, and that the changes in structure lead to an agglomeration of Pd nanoparticles. These results, combined with those for the AgPd catalysts, serve to highlight the effects that pretreatment conditions can have on catalyst structure, alluding to the dynamic nature of the catalysts and potential differences that develop based on choice of catalyst support. When evaluating the reactivity of these catalytic systems for the hydrogenation of acetylene, it was found that the bimetallic AgPd and CuPd catalysts were generally more selective to ethylene formation than the monometallic Pd catalysts, and that the TiO_2-supported bimetallic catalysts were more selective than the SiO_2-supported materials for ethylene generation.

3.3.4 Ni-Mo Multimetallic Catalysts for Synthesis Gas Conversion

In a final case study, the effect of transition metal promoter on SiO_2-supported molybdenum oxide catalysts synthesized by atomic layer deposition was evaluated for the conversion of synthesis gas to higher alcohols[11]. In this study, XANES data was used as a supporting technique to understand the effect of hydrogen spillover on the reaction mechanism by evaluating the oxidation state of Ni and Mo species in response to the presence of additional promoters. The composition of oxidation states determined via XANES analysis from the Ni-K and Mo-K edges for all catalysts is shown in Table 3.7. These results show that all Ni-containing samples have metallic Ni as their primary component, while the monometallic molybdenum catalyst contains only Mo^{+4} species. Interestingly, the addition of Ni to MoO_x catalysts improved the reducibility of molybdenum, leading to at least a 40% presence of $Mo^{+\delta}$ $(0 < \delta < 2)$ species in these materials.

Table 3.7. Fractional composition of oxidation states for Ni- and Mo-containing catalysts used in synthesis gas conversion, as determined from XANES measurements at the Ni-K and Mo-K edges.

Catalyst	Ni^0	Ni^{+2}	$Mo_{0<\delta<2}^{+\delta}$	Mo^{+4}	Mo^{+6}
Ni/SiO_2	0.83	0.17	--	--	--
$Ni/MoO_x/SiO_2$	0.92	0.08	0.51	0.49	0
$Ni/MoMnO_x/SiO_2$	0.89	0.11	0.50	0.50	0
$Ni/MoTiO_x/SiO_2$	0.85	0.15	0.40	0.60	0
$Ni/MoAlO_x/SiO_2$	0.89	0.11	0.30	0.55	0.15
MoO_x/SiO_2	--	--	0	1.00	0

However, the addition of reducible metal oxides like MnO_x and TiO_x did not seem to cause a significant change in the distribution of molybdenum states. The addition of AlO_x, on the other hand, led to the presence of Mo^{+6} species with a decrease in the presence of $Mo^{+\delta}$ for the $Ni/MoAlO_x/SiO_2$ catalyst when compared to the other multi-metallic materials. This finding indicates that the non-reducible AlO_x dopant actually blocks hydrogen spillover and slows down the reduction of the molybdenum species.

These XANES results are consistent with temperature programmed reduction (TPR) and isotopic H_2-D_2 exchange experiments used to explore the presence of hydrogen spillover phenomena in this study. From TPR experiments, it was noted that the addition of reducible metals to the MoO_x catalyst shifts the reduction peak to lower temperatures, indicating that the reduction of MoO_x is facilitated by hydrogen spillover from reducible metals. In conjunction, the H_2-D_2 experiments highlighted that the exchange rate in the Ni and $NiMoO_x$ catalysts were similar and related to the presence of Ni, as the exchange rate over the MoO_x catalyst was around two orders of magnitude lower.

3.4 Conclusions

X-ray absorption spectroscopy studies are a fundamental tool in understanding the structural environment of supported multi-metallic heterogeneous catalysts. Various case studies from work within our group highlight the importance of structural characterization for specially synthesized catalysts using CSR and ALD techniques. The extent of bimetallic nanoparticle formation in AgPd, CuPd, and AuPd catalysts synthesized by CSR was evaluated using EXAFS to inspect the local coordination and nearest neighbor distance of the Pd species. This information further served to understand the dispersion of Pd on the parent metal as well as the effect of support on the extent of bimetallic particle formation. Furthermore, XANES analyses of Pd-containing bimetallic and Mo-based multi-metallic catalysts helped to understand the reducibility of the respective catalysts and served as evidence for the existence of support effects and hydrogen spillover on the extent of metal reduction.

3.5 References

(1) van Bokhoven, J. A.; Lamberti, C. *X-Ray Absorption and X-Ray Emission Spectroscopy: Theory and Applications*; 2015; Vol. 1–2.

(2) Zaera, F.; Ma, Z. Characterization of Heterogeneous Catalysts. In *Surface and Nanomolecular Catalysis*; Richards, R. M., Ed.; Taylor & Francis (CRC Press), 2006; pp 1–38.

(3) Ro, I.; Aragao, I. B.; Chada, J. P.; Liu, Y.; Rivera-Dones, K. R.; Ball, M. R.; Zanchet, D.; Dumesic, J. A.; Huber, G. W. The Role of Pt-FexOy Interfacial Sites for CO Oxidation. *J. Catal.* **2018**, *358*, 19–26.

(4) Ro, I.; Aragao, I. B.; Brentzel, Z. J.; Liu, Y.; Rivera-Dones, K. R.; Ball, M. R.; Zanchet, D.; Huber, G. W.; Dumesic, J. A. Intrinsic Activity of Interfacial Sites for Pt-Fe and Pt-Mo Catalysts in the Hydrogenation of Carbonyl Groups. *Appl. Catal. B Environ.* **2018**, *231*, 182–190.

(5) Sener, C.; Wesley, T. S.; Alba-Rubio, A. C.; Kumbhalkar, M. D.; Hakim, S. H.; Ribeiro, F. H.; Miller, J. T.; Dumesic, J. A. PtMo Bimetallic Catalysts Synthesized by Controlled Surface Reactions for Water Gas Shift. *ACS Catal.* **2016**, *6* (2), 1334–1344.

(6) Ball, M. R.; Wesley, T. S.; Rivera-Dones, K. R.; Huber, G. W.; Dumesic, J. A. Amination of 1-Hexanol on Bimetallic AuPd/TiO2 Catalysts. *Green Chem.* **2018**, *20* (20), 4695–4709.

(7) Ball, M. R.; Rivera-Dones, K. R.; Stangland, E.; Mavrikakis, M.; Dumesic, J. A. Hydrodechlorination of 1,2-Dichloroethane on Supported AgPd Catalysts. *J. Catal.* **2019**, *370*, 241–250.

(8) Alba-Rubio, A. C.; Sener, C.; Hakim, S. H.; Gostanian, T. M.; Dumesic, J. A. Synthesis of Supported RhMo and PtMo Bimetallic Catalysts by Controlled Surface Reactions. *ChemCatChem* **2015**, *7* (23), 3881–3886.

(9) Hakim, S. H.; Sener, C.; Alba-Rubio, A. C.; Gostanian, T. M.; O’Neill, B. J.; Ribeiro, F. H.; Miller, J. T.; Dumesic, J. A. Synthesis of Supported Bimetallic Nanoparticles with Controlled Size and Composition Distributions for Active Site Elucidation. *J. Catal.* **2015**, *328*, 75–90.

(10) O’Neill, B. J.; Jackson, D. H. K.; Lee, J.; Canlas, C.; Stair, P. C.; Marshall, C. L.; Elam, J. W.; Kuech, T. F.; Dumesic, J. A.; Huber, G. W. Catalyst Design with Atomic Layer Deposition. *ACS Catal.* **2015**, *5* (3), 1804–1825.

(11) Zhang, L.; Ball, M. R.; Rivera-Dones, K. R.; Wang, S. C.; Kuech, T. F.; Huber, G. W.; Hermans, I.; Dumesic, J. A. Synthesis Gas Conversion over Molybdenum-Based Catalysts Promoted by Transition Metals. *ACS Catal.* **2020**, *10* (1), 365–374.

(12) Christensen, S. T.; Feng, H.; Libera, J. L.; Guo, N.; Miller, J. T.; Stair, P. C.; Elam, J. W. Supported Ru-Pt Bimetallic Nanoparticle Catalysts Prepared by Atomic Layer Deposition. *Nano Lett.* **2010**, *10* (8), 3047–3051.

(13) Johansson, A. C.; Larsen, J. V.; Verheijen, M. A.; Haugshøj, K. B.; F. Clausen, H.; Kessels, W. M. M.; H. Christensen, L.; Thomsen, E. V. Electrocatalytic Activity of Atomic Layer

Deposited Pt-Ru Catalysts onto N-Doped Carbon Nanotubes. *J. Catal.* **2014**, *311*, 481–486.

(14) Lu, J.; Low, K. Bin; Lei, Y.; Libera, J. A.; Nicholls, A.; Stair, P. C.; Elam, J. W. Toward Atomically-Precise Synthesis of Supported Bimetallic Nanoparticles Using Atomic Layer Deposition. *Nat. Commun.* **2014**, *5*.

(15) Lei, Y.; Liu, B.; Lu, J.; Lobo-Lapidus, R. J.; Wu, T.; Feng, H.; Xia, X.; Mane, A. U.; Libera, J. A.; Greeley, J. P.; et al. Synthesis of Pt-Pd Core-Shell Nanostructures by Atomic Layer Deposition: Application in Propane Oxidative Dehydrogenation to Propylene. *Chem. Mater.* **2012**, *24* (18), 3525–3533.

(16) Ball, M. R.; Rivera-Dones, K. R.; Stangland, E.; Mavrikakis, M.; Dumesic, J. A. Hydrodechlorination of 1,2-Dichloroethane on Supported AgPd Catalysts. *J. Catal.* **2019**, *370*, 241–250.

(17) Ball, M. R.; Rivera-Dones, K. R.; Gilcher, E. B.; Ausman, S. F.; Hullfish, C. W.; Lebrón, E. A.; Dumesic, J. A. AgPd and CuPd Catalysts for Selective Hydrogenation of Acetylene. *ACS Catal.* **2020**, *10* (15), 8567–8581.

(18) Glyzdova, D. V.; Vedyagin, A. A.; Tsapina, A. M.; Kaichev, V. V.; Trigub, A. L.; Trenikhin, M. V.; Shlyapin, D. A.; Tsyrulnikov, P. G.; Lavrenov, A. V. A Study on Structural Features of Bimetallic Pd-M/C (M: Zn, Ga, Ag) Catalysts for Liquid-Phase Selective Hydrogenation of Acetylene. *Appl. Catal. A Gen.* **2018**, *563*, 18–27.

(19) Aich, P.; Wei, H.; Basan, B.; Kropf, A. J.; Schweitzer, N. M.; Marshall, C. L.; Miller, J. T.; Meyer, R. Single-Atom Alloy Pd-Ag Catalyst for Selective Hydrogenation of Acrolein. *J. Phys. Chem. C* **2015**, *119* (32), 18140–18148.

Chapter 4. Effects of zeolite support in the hydrogenation of carbonyl groups over Pt/ZSM-5 catalysts[a,b]

4.1 Introduction

Pt catalysts have been widely used and studied due to their high activity and selectivity in a variety of reactions such as CO oxidation[1,2], water gas shift[3,4], and (de)-hydrogenation[5–7] reactions. Many attempts have been made to increase the activity of Pt catalysts by the addition of promoting materials such as Fe, Sn, and Ga and by utilization of active supports such as TiO_2 and zeolite.[6,8–13] Cortright et al. demonstrated improvements in catalytic activity and selectivity for the dehydrogenation of isobutane over L-zeolite-supported PtSn catalysts.[6] Gercecker et al. also showed significant improvements in activity and resistance to coke formation for PtSn over Pt catalysts in the non-oxidative coupling of methane.[11] Ponec et al. studied the promotional effects of Fe, Ga, and Ge on Pt catalysts and found enhanced activity in the hydrogenation of acetone and propanal with the promoted materials.[14] Somorjai et al showed that adding Fe to Pt catalysts increased the catalytic hydrogenation of ethylene and cyclohexene.[8]

Various enhancement mechanisms were suggested and include electronic (ligand) effects[15,16], lattice strain effects[17], geometric (ensemble) effects[18], surface adsorption of inactive spectator species[8], and additional active sites[19]. Ammal and co-workers demonstrated that TiO_2 support at Pt-TiO_2 interface can provide oxygen vacancies that promote H_2O adsorption and dissociation for the water gas shift reaction.[20] Dumesic and coworkers used DFT calculations, microkinetic modeling, and imaging techniques to partially attribute the catalytic performance of PtSn catalysts

---

[a] Rivera-Dones, K. R.; Ro, I.; Huber, G.W.; Dumesic, J.A. “Superior catalytic performance of zeolite-supported Pt catalysts for the hydrogenation of carbonyl group: effect of zeolite support” *Manuscript under development.*

[b] Author contributions: K.R.R.D. and I.R. contributed equally to this work and performed all reactivity and characterization studies. All authors contributed to manuscript development.

to particle size effects in the conversion of methane to ethylene and aromatics.[11] This same study also discussed the importance of acid sites adjacent to Pt species in zeolite-supported materials for the formation of a hydrocarbon pool conducive to the oligomerization of ethylene species. Moreover, we have also recently shown that the formation of Pt-Fe_xO_y and Pt-MoO_x interfacial sites increases the activity of platinum-based catalysts for the hydrogenation of carbonyl groups by increasing the interaction of the C=O bond with the catalyst surface.[9]

While the addition of promoters has been a widely used method in the enhancement of platinum catalysts, an alternative approach has recently been presented to increase the activity of Pt-based materials. This approach involves the design and synthesis of Pt single atom catalysts. Atomically dispersed Pt catalysts have recently received considerable attention due to their more efficient use of Pt atoms. Datye and co-workers developed thermally stable and active Pt single atoms on CeO_2 catalyst for CO oxidation.[21] Flytzani-Stephanopoulos and co-workers found that Pt single atoms embedded in Cu (111) or Cu nanoparticles exhibit high activity and selectivity for butadiene hydrogenation to butenes.[22] Zhang and co-workers demonstrated that a Pt single atom catalyst has higher atom efficiency compared to a Pt nanoparticle catalyst for both CO oxidation and preferential oxidation of CO in H_2.[2]

The work discussed in this chapter involves the preparation of Pt catalysts on different supports such as SiO_2, Al_2O_3, and zeolites with different acidities to investigate their activity for acetone hydrogenation. Specifically, we investigated the effect of catalyst support and pretreatment conditions based on the hypothesis that particle size, location, or electronic state of the platinum species as well as the interaction between metal and support could vary as a result of synthesis conditions and subsequently affect catalytic activity. Therefore, this study is aimed at providing a better understanding of the dominant factors influencing catalytic activity in the hydrogenation of carbonyl groups that could be used to further develop platinum catalysts with improved atomic efficiency.

4.2. Experimental Methods

4.2.1 Catalyst Synthesis

Pt/ZSM-5 catalysts were prepared by an ion-exchange as follows. The NH_4^+ form of the ZSM-5 supports (Zeolyst) with different acidities (SiO_2:Al_2O_3 = 23, 80, and 280) were calcined at 873 K for 18 h (with a heating rate of 1 K min^{-1}) to obtain the H-ZSM-5 form. Hereafter, the zeolite supports will be referred to as ZSM-5 (x), where x is the SiO_2/Al_2O_3 ratio of the support. Tetraammineplatinum(II) nitrate [$[Pt(NH_3)_4](NO_3)_2$, Sigma-Aldrich] was added to Milli-Q water, and the H-ZSM-5 support was dispersed in solution and left under continuous mixing at room temperature for 24 h. Afterwards, the solid material was extracted by centrifugation, and the recovered solid was added into a fresh aqueous solution containing tetraammineplatinum(II) nitrate for a 2nd deposition cycle. The exchange was repeated for a total of 3 cycles, after which the solid was once again recovered by centrifugation, washed and filtered with 1 L of Milli-Q water, and dried at 383 K overnight. Since the platinum loading of Pt/ZSM-5 catalysts synthesized by this ion exchange method was solely dependent on the acidity of the zeolite support, a control 0.59 wt% Pt/ZSM-5(280) catalyst was prepared using incipient wetness impregnation for comparison. Pt/SiO_2 and Pt/Al_2O_3 catalysts were prepared by an incipient wetness impregnation of SiO_2 (Davisil grade 646, Sigma-Aldrich) and γ-Al_2O_3 (Strem Chemicals) with an aqueous solution of chloroplatinic acid hexahydrate ($H_2PtCl_6 \cdot 6H_2O$) (Sigma-Aldrich), as described in detail elsewhere.[23] The samples were calcined *ex situ* (denoted as EC@) at 573 K or 773 K under air flow for 1 h (with a heating rate of 6 K min^{-1}), followed by an *in situ* reduction (denoted as IR@) at 353 K or 573 K.

4.2.2 Reactivity Measurements

The catalytic activity for gas-phase acetone hydrogenation was evaluated in a fixed-bed quartz reactor at atmospheric pressure, as described elsewhere.[9] Prior to reactivity measurements, catalysts were reduced *in situ* at 353 or 573 K (with a heating rate of 3 K min^{-1}) under H_2 flow (20 cm^3 (STP) min^{-1}) for 2 h. Catalysts (1-130 mg) were diluted with 150 mg of crushed silica chips (silicon dioxide, fused, 60-100 mesh, Sigma Aldrich) and placed in the center of the reactor. Liquid acetone (>99.5%, Fisher Scientific) was fed to the reactor system at room temperature using a flow rate of 0.75 µL/min via syringe pump (Harvard Apparatus). The acetone feed was vaporized at the reactor inlet by mixing with He and H_2 flowing at rates of 25 and 5 cm^3 (STP) min^{-1}, respectively. The temperature of the reactor was measured using a K-type thermocouple attached to the outside of the reactor wall. The reaction temperature was adjusted by a variable autotransformer power source connected to a tube furnace. Control experiments without catalyst confirmed the absence of reactivity from the reactor. Reaction products were analyzed by an online gas chromatograph with a barrier discharge ionization detector (GC-BID) system (Shimadzu). The acetone hydrogenation reaction rate was measured at 353 K after 1 h, and the turnover frequency (TOF) was calculated using the number of Pt sites measured by CO chemisorption.

4.3 Catalyst Characterization

4.3.1 CO Chemisorption

The CO chemisorption studies were carried out using a Setaram C-80 heat-flux calorimeter, which was connected to a gas handling system and a volumetric system. Pressure was monitored with Baratron capacitance manometers ($\pm 0.5\times10^{-4}$ Torr), allowing precise pressure measurements, as described in detail elsewhere.[24] The catalysts were reduced under H_2 flow at either 353K or 573

K, and CO adsorption was performed at 293 K after reduction. The adsorption stoichiometry between CO and surface Pt sites was assumed to be 1:1.

4.3.2 Inductively Coupled Plasma-Absorption Emission Spectroscopy (ICP-AES)

The Pt loading of catalysts was determined using a Varian Vista-MPX ICP-OES instrument (Agilent Technologies Inc., Santa Clara, CA USA). Typically, 40 mg of catalyst were digested in a mixture of 2.5 g of nitric acid (Fischer, 65 %) and 7.5 g of hydrochloric acid (Fischer, 37 %) by refluxing at 393 K for 12 hours. Platinum standards for the ICP analysis were prepared from a commercially available Pt ICP standard solution (Aldrich, 979 mg L^{-1}). After digestion, the solution mixture was cooled to room temperature, diluted in Milli-Q water, filtered, and analyzed with ICP emission spectrometer.

4.3.3 NH_3-temperature-programmed desorption (NH_3-TPD)

NH_3-TPD was carried out to measure the acid site densities of all prepared catalysts. Approximately 100 mg of each catalyst sample were loaded onto a flow-through cell and heated to 473 K under helium flow, followed by a 1 h temperature soak to remove excess moisture. After cooling to 423 K, NH_3 was adsorbed on the sample from a 1% NH_3/He flow for 45 min. Following NH_3 saturation, the sample was purged with helium at 423 K for 90 min to remove weakly adsorbed species. Afterwards, the sample was heated to 973 K under helium flow with a 10 K/min ramp and held at 973 K for 2 h. The desorption of ammonia species from the catalyst surface was monitored by an online Omnistar (Pfeiffer Vacuum) mass spectrometer. The evolution of water was also monitored to account for the effect of its fragmentation pattern in the quantification of ammonia.

4.4 Results and Discussion

Table 4.1 shows the number of acid sites in the prepared catalysts as determined by NH_3-TPD. The number of acid sites of the zeolite supported Pt catalysts after calcination at 573 K increases with decreasing SiO_2:Al_2O_3 ratio, from 667 μmol g_{cat}^{-1} over Pt/ZSM-5 (23) to 36 μmol g_{cat}^{-1} over Pt/ZSM-5 (280). The number of acid sites of the zeolite catalysts after high temperature calcination at 773 K decreases compared to the low temperature calcination at 573 K, but the increasing trend with decreasing SiO_2:Al_2O_3 ratio was maintained. According to previous studies, the decrease in the acidity of the zeolite with increasing calcination temperatures can be ascribed to the dehydroxylation of the zeolite lattice[25,26], the conversion of Bronsted acid sites into Lewis acid sites[26], and a local dealumination of the lattice[27] (i.e. the transformation of the tetrahedral Al of the framework into the extra-lattice octahedral Al in the pore system) at the higher temperature pretreatment. In contrast, the Pt/Al_2O_3 catalyst showed an increase in acid site density with an increase in calcination temperature. Since the Al_2O_3 support only contains Lewis acid sites, the increase in acidity observed at the higher pretreatment temperature could be explained by an increase in the total number of Lewis acid sites, as reported previously.[28–30] Acid sites were not detected on Pt/SiO_2 by NH_3 TPD.

Table 4.1. Acid site density of Pt catalysts [a]

Catalyst	Calcination temperature (K)	Acid site density (μmol g_{cat}^{-1})
Pt/ZSM-5 (280)	573	36
	773	25
Pt/ZSM-5 (80)	573	264
	773	177
Pt/ZSM-5 (23)	573	667
	773	312
Pt/SiO_2	573	n.d.[b]
	773	n.d.[b]
Pt/Al_2O_3	573	97
	773	133

[a] Acid site density was measured by NH_3 TPD. [b] the number of acid sites was not detectable.

Table 4.2 shows the platinum loading and the metal site density determined by ICP and CO chemisorption measurements, respectively. The Pt loading of the zeolite-supported catalysts was found to be higher on the more acidic zeolite support, which can be explained by the higher ion exchange capacity of the more acidic zeolite.

Table 4.2. Pt loading and metal site density of catalysts as a function of pretreatment conditions

Catalyst	Pt loading [a] (wt%)	Calcination temperature (K)	Reduction temperature (K)	Pt site density [b] (μmol g_{cat}^{-1})	Dispersion (%)
Pt/ZSM-5 (280)	0.25	573	353	1.83	14
		573	573	2.12	17
		773	353	0.66	5
		773	573	0.86	7
Pt/ZSM-5 (80)	0.50	573	353	8.92	35
		573	573	12.10	47
		773	353	20.14	79
		773	573	9.89	39
Pt/ZSM-5 (23)	2.29	573	353	14.40	12
		573	573	12.72	11
		773	353	12.23	10
		773	573	13.63	12
Pt/SiO_2	0.23	573	353	2.55	22
		573	573	5.66	48
		773	353	2.76	23
		773	573	1.25	11
Pt/Al_2O_3	0.23	573	353	n.d.[c]	0
		573	573	6.80	58
		773	353	n.d.[c]	0
		773	573	5.03	43

[a] Platinum loading was measured by ICP. [b] Pt surface site density was measured by CO chemisorption. [c] the number of Pt site was not detectable.

It is interesting to note that no Pt sites were detected over Pt/Al_2O_3 after reduction at 353 K, unlike Pt on SiO_2 and zeolite supports. This is because the degree of reduction for Pt is different depending on the type of support. It was reported that the degree of reduction of Pt/Al_2O_3 and Pt/SiO_2 at 873 K is 45 and 70%, respectively, based on temperature-programmed reduction (TPR) results.[10] In addition, the main peak of the Pt/Al_2O_3 TPR spectrum is positioned at 848 K, whereas those of Pt/SiO_2 and Pt/ZSM-5 are located at 578/698 K and 533/713 K, respectively.[7,33] Therefore, it is likely that the lower hydrogen pretreatment temperature of 353 K was not sufficient to induce a significant reduction of the platinum species on the Pt/Al_2O_3 catalyst. Moreover, there is a larger decrease in Pt sites after high temperature calcination over the Pt/SiO_2 catalyst compared to the changes observed over Pt/Al_2O_3 and Pt/ZSM-5. Corma and co-workers suggested that the encapsulation of nanoparticles by zeolite support can alleviate the aggregation of Pt metal speices after treatement at high temperature.[32] It was also reported that the interaction between Pt and support is weaker on SiO_2 than on supports such as zeolite and Al_2O_3, and therefore Pt species on the SiO_2 support are more susceptible to sintering, in agreement with our results.[32,34]

Figure 4.1 shows infrared spectra, collected at 298 K, of CO chemisorbed on the Pt/SiO_2 and the Pt/ZSM-5 (280 and 80) catalysts following a calciantion at 773 K and reduction at both 353 K and 573 K. The spectra of Pt/SiO_2 and the two zeolite-supported Pt catalysts exhibited a main feature at 2050 and 2085 cm^{-1}, respectively. A decrease in the peak areas was observed after reduction at 573 K compared to that at 353 K, which is indicative of a decrease in the number of Pt sites as a result of metal sintering, as mentioned earlier. The higher frequency feature of CO adsorbed on the Pt/ZSM-5 catalysts compared to Pt/SiO_2 can be attributed to Pt located in different structual environments on the support. Stakheev and co-workers assigned the band at 2082 cm^{-1} to small Pt particles inside zeolite pores, while the band at 2056 cm^{-1} was assigned to particles on the outer zeolite surface of the Pt/ZSM-5 catalyst.[35] They also attributed the higher frequency band (2082 cm^{-1}) on zeolite-supported catalysts to a decrease in electron density of Pt particles located inside zeolite pores due to their interaction with strong Bronsted acid sites of the H-ZSM-5 support.

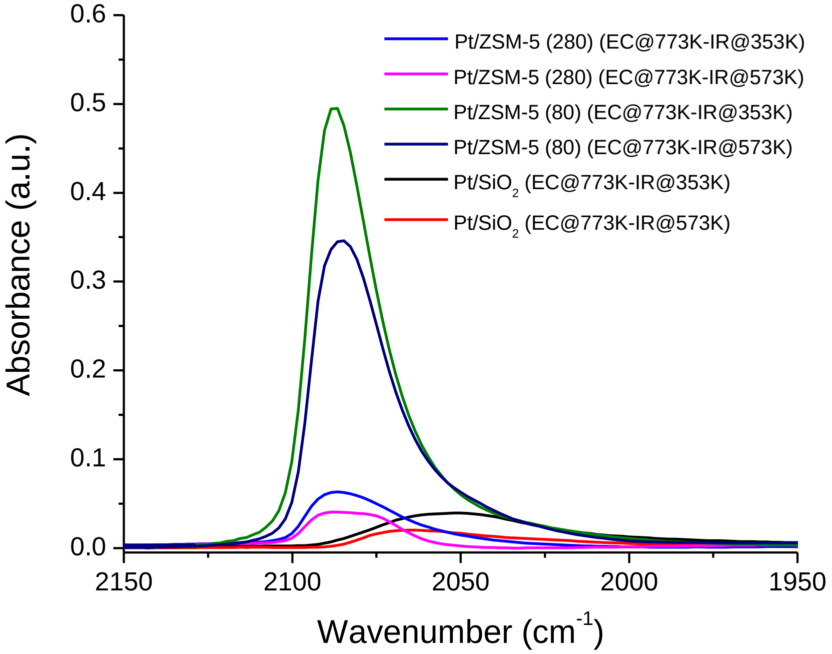

Figure 4.1. CO-FTIR spectra collected at 298 K of in situ reduced Pt/ZSM-5, Pt/SiO$_2$, and Pt/Al$_2$O$_3$ catalysts after introduction of 8 Torr CO, followed by a 10 min evacuation under He flow. Intensities are normalized by pellet density.

Figure 4.2 shows the specific conversion rate (based on the amount of Pt measured by ICP) and TOF (based on Pt sites measured by CO chemisorption) for acetone hydrogenation over the Pt/ZSM-5, Pt/SiO$_2$, and Pt/Al$_2$O$_3$ catalysts. All catalysts showed 100% selectivity to isopropanol (IPA) under these reaction conditions, except for Pt/ZSM-5 (23) after calcination at 573 K, followed by reduction at 353 K. The large number of acid sites available in the Pt/ZSM-5 (23) after these pretreatment conditions, shown in Table 4.1, can subsequently dehydrate IPA to form di-isopropyl ether (DIPE), as reported previously.[31] This dehydration of IPA to generate DIPE occurred to a small extent over the highly acidic Pt/ZSM-5 (23) catalyst, as reflected in a measured DIPE selectivity between 5 - 7%. Overall, the specific reaction rate and TOF over zeolite-supported Pt catalysts were higher than those observed over the Pt/SiO_2 and Pt/Al_2O_3 catalysts for acetone hydrogenation, as shown in Figure 4.2. Among the zeolite supported catalysts, the Pt/ZSM-5 (280) catalyst exhibited the highest specific conversion and TOF. The catalytic activity was also observed to decrease with decreasing SiO_2:Al_2O_3 ratio. In addition, significant changes in the catalytic activity after different pretreatment conditions were observed. In general, zeolitic materials calcined at 773 K were more active than those calcined at 573 K, and those reduced at 353 K displayed higher activity than those reduced at 573 K. It is also worthwhile to note that these relative differences in activity became less drastic with decreasing SiO_2/Al_2O_3 ratios. On non-zeolitic materials, however, the highest activity was observed on those catalysts exposed to the harshest pretreatment conditions (EC@773K-IR@573K).

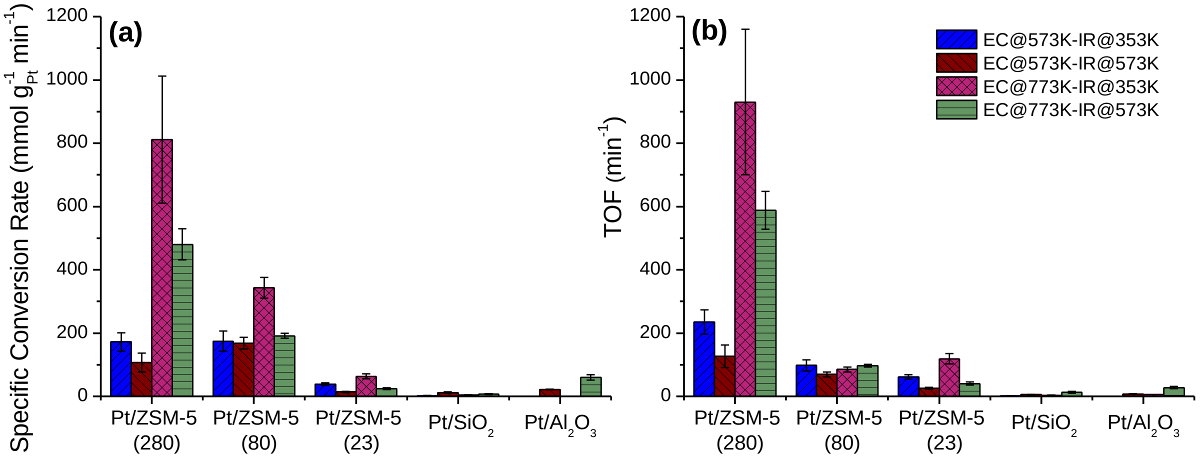

Figure 4.2. (a) Specific conversion rate and (b) turnover frequencies for acetone hydrogenation to IPA over Pt/ZSM-5, Pt/SiO_2, and Pt/Al_2O_3 catalysts.

To probe the relevance of support acidity for zeolitic materials in the hydrogenation of carbonyl groups, we conducted an acetone hydrogenation control experiment using a 0.58 wt% Pt/ZSM-5 (280) catalyst. This catalyst was chosen to maintain a similar platinum loading to the Pt/ZSM-5 (80) catalyst shown above while varying the support acidity. The 0.58 wt% Pt/ZSM-5 (280) catalyst was calcined and reduced at 573 K, and was found to have a specific conversion rate of 41 mmol $g_{Pt}^{-1}min^{-1}$ and a TOF of 44 min^{-1}. When compared to the results shown in Figure 4.2 for the same pretreatment conditions, the activity of the 0.58% Pt/ZSM-5 (280) was observed to be lower than that of the 0.25% Pt/ZSM-5 (280) catalysts and more comparable to that of the 0.5% Pt/ZSM-5 (80) catalyst. Therefore, it would appear that the acidity of the zeolite support is not a significant contributor to the activity of these catalysts for acetone hydrogenation.

The Pt/ZSM-5 (280) catalyst after EC@773K-IR@353K, which exhibited the highest specific conversion rate shown in Figure 4.2, had the lowest number of platinum sites among the zeolite-supported catalysts. Interestingly, the CO uptake of the Pt/ZSM-5 (280) catalyst decreased in the following order: EC@573K-IR@573K > EC@573K-IR@353K > EC@773K-IR@573K > EC@773K-IR@353K. This trend in CO uptake is opposite to that observed to the trend found in catalytic performance, as noted by the specific acetone conversion rate. This result could be related to changes in the particle size of Pt species after the different pretreatment temperatures and atmospheres, as these conditions can play an important role in the level of dispersion and on the effects of sintering.[40,41] Corma and coworkers claimed that oxidation treatments cause disintegration of larger Pt crystallites into sub-nanoclusters, while reduction treatments result in the sintering of metal particles over chabazite zeolite-supported platinum catalysts.[32] Specifically, they showed that the degree of disintegration and sintering of Pt species after calcination and reduction treatment, respectively, increases with increasing treatment temperatures.

It is worthwhile to note that the synthesis method used in this work for zeolite-supported materials could have a role in the final location of the platinum particles within the three-dimensional zeolite structure. Ion-exchanged materials have been found to have metal ions predominantly located in the zeolite channels at ion exchange sites.[36–38] This is in contrast to catalysts synthesized by impregnation methods, which generally result in metal particles that are located primarily on the external surface of the zeolite with only a small fraction of particles located in the channels of the zeolite. Therefore, it is plausible that the Pt/ZSM-5 catalysts used in this work have a non-negligible presence of Pt species within the zeolite channels, and that stabilization of these species can be achieved by confinement effects within the zeolite pores, which would align with the trends observed for changes in CO uptake of as a result of pretreatment temperature.

It is also possible that electron deficient Pt species inside zeolite pores lead to the underestimation of these platinum sites for zeolite supported Pt catalysts, in agreement with the CO uptake shown in Table 4.2. Folefoc and Dwyer also observed similar behaviors and ascribed the lower adsorption of probe molecules (such as CO and H_2) on the small Pt agglomerates over Pt/ZSM-5 to electron deficiency effects as a result of the electron transfer that occurs from Pt atoms to acid sites on the ZSM-5 support.[42] Itoi and co-workers pointed out the difficulty in the accurate estimation of the dispersion for Pt sub-nanoclusters using conventional chemisorption analyses with probe molecules such as CO or H_2.[43] In fact, Datye and co-workers used XRD measurements to determine the amount of Pt species present in their catalysts because CO chemisorption was found to be inappropriate for site estimation of atomically dispersed Pt catalysts.[21] Therefore, the inverse correlation observed sites for the Pt/ZSM-5 (280) catalyst between the specific conversion rate and the number of Pt sites following the different pre-treatments can be related to the unsuccessful assessment of sub-nanoclusters by CO chemisorption.

In this work, it was shown that ZSM-5 supported Pt catalysts exhibited enhanced activity over Pt/SiO_2 and Pt/Al_2O_3 catalysts for acetone hydrogenation. The three-dimensional structure of the ZSM-5 support could likely facilitate the contact between reactants and the Pt active sites inside the pores through the so-called confinement effect. This confinement effect potentially stabilizes reaction precursors and intermediates through interaction with C=O moieties, and thereby increases the acetone hydrogenation reaction rates. Similar to Pt/ZSM-5 catalysts, we have recently demonstrated that the formation of Pt-Fe_xO_y and Pt-MoO_x interfacial sites improved the catalytic activity for carbonyl group hydrogenation by promoting the interaction between the C=O bond and the catalyst surface.[9] Although the formation of interfacial sites showed an order of magnitude enhancement in the catalytic activity over the their monometallic counterparts, creating active interfacial sites for carbonyl group hydrogenation requires a considerable amount of Pt (5 wt%), and those bimetallic catalysts still exhibited a lower atom efficiency compared to Pt/ZSM-5.[9] In this sense, the findings from this work will provide guidance for the design of more active Pt catalysts for carbonyl group hydrogenation while minimizing the amount of noble Pt metal used.

4.5 Conclusions

A variety of Pt/ZSM-5, Pt/SiO_2, and Pt/Al_2O_3 catalysts were used to investigate the effects of catalyst support and pretreatment conditions on acetone hydrogenation. ZSM-5-supported catalysts exhibited specific conversion rates and turnover frequencies that were 2-3 orders of magnitude higher than those for the SiO_2- and Al_2O_3-supported catalysts at all pretreatment conditions. While no significant direct effects from zeolite support acidity on the catalytic activity were observed, CO-FTIR results indicated a shift to higher frequencies of the Pt-CO band in ZSM-5 catalysts when compared to Pt/SiO_2.These results suggest that the enhanced catalytic activity observed over Pt/ZSM-5 catalysts could be due to the interaction of Pt species with the three-dimensional structure of the zeolite support. Specifically, the presence of Pt species within the zeolite pores could stabilize the metal particles, making them more resistant to morphological changes following variations in pretreatment, and enhance catalytic activity for acetone hydrogenation due to confinement effects.

4.6 References

(1) Johansson, A. C.; Larsen, J. V.; Verheijen, M. A.; Haugshøj, K. B.; F. Clausen, H.; Kessels, W. M. M.; H. Christensen, L.; Thomsen, E. V. Electrocatalytic Activity of Atomic Layer Deposited Pt-Ru Catalysts onto N-Doped Carbon Nanotubes. *J. Catal.* **2014**, *311*, 481–486.

(2) Qiao, B.; Wang, A.; Yang, X.; Allard, L. F.; Jiang, Z.; Cui, Y.; Liu, J.; Li, J.; Zhang, T. Single-Atom Catalysis of CO Oxidation Using Pt1/FeO X. *Nat. Chem.* **2011**, *3* (8), 634–641.

(3) Wei, J. M.; Iglesia, E. Mechanism and Site Requirements for Activation and Chemical Conversion of Methane on Supported Pt Clusters and Turnover Rate Comparisons among Noble Metals. *J. Phys. Chem. B* **2004**, *108*, 4094–4103.

(4) Sener, C.; Wesley, T. S.; Alba-Rubio, A. C.; Kumbhalkar, M. D.; Hakim, S. H.; Ribeiro, F. H.; Miller, J. T.; Dumesic, J. A. PtMo Bimetallic Catalysts Synthesized by Controlled Surface Reactions for Water Gas Shift. *ACS Catal.* **2016**, *6* (2), 1334–1344.

(5) Deng, L.; Miura, H.; Shishido, T.; Wang, Z.; Hosokawa, S.; Teramura, K.; Tanaka, T. Elucidating Strong Metal-Support Interactions in Pt–Sn/SiO2 Catalyst and Its Consequences for Dehydrogenation of Lower Alkanes. *J. Catal.* **2018**, *365*, 277–291.

(6) Cortright, R. D.; Dumesic, J. A. L-Zeolite-Supported Platinum and Platinum/Tin Catalysts for Isobutane Dehydrogenation. *Appl. Catal. A Gen.* **1995**, *129* (1), 101–115.

(7) Bai, L.; Zhou, Y.; Zhang, Y.; Liu, H.; Tang, M. Influence of Calcium Addition on Catalytic Properties of PtSn/ZSM-5 Catalyst for Propane Dehydrogenation. *Catal. Letters* **2009**, *129* (3–4), 449–456.

(8) Wang, H.; Krier, J. M.; Zhu, Z.; Melaet, G.; Wang, Y.; Kennedy, G.; Alayoglu, S.; An, K.; Somorjai, G. A. Promotion of Hydrogenation of Organic Molecules by Incorporating Iron into Platinum Nanoparticle Catalysts: Displacement of Inactive Reaction Intermediates. *ACS Catal.* **2013**, *3* (10), 2371–2375.

(9) Ro, I.; Aragao, I. B.; Brentzel, Z. J.; Liu, Y.; Rivera-Dones, K. R.; Ball, M. R.; Zanchet, D.; Huber, G. W.; Dumesic, J. A. Intrinsic Activity of Interfacial Sites for Pt-Fe and Pt-Mo Catalysts in the Hydrogenation of Carbonyl Groups. *Appl. Catal. B Environ.* **2018**, *231*, 182–190.

(10) Bariå, O. A.; Holmen, A.; Blekkan, E. A. *Propane Dehydrogenation over Supported Pt and Pt-Sn Catyalysts: Catalyst Preparation, Characterization, and Activity Measurements*; 1996; Vol. 158.

(11) Gerceker, D.; Motagamwala, A. H.; Rivera-Dones, K. R.; Miller, J. B.; Huber, G. W.; Mavrikakis, M.; Dumesic, J. A. Methane Conversion to Ethylene and Aromatics on PtSn Catalysts. *ACS Catal.* **2017**, *7* (3), 2088–2100.

(12) Michalak, W. D.; Krier, J. M.; Alayoglu, S.; Shin, J.-Y.; An, K.; Komvopoulos, K.; Liu, Z.; Somorjai, G. A. CO Oxidation on PtSn Nanoparticle Catalysts Occurs at the Interface of Pt and Sn Oxide Domains Formed under Reaction Conditions. **2014**.

(13) Sattler, J. J. H. B.; Gonzalez-Jimenez, I. D.; Luo, L.; Stears, B. A.; Malek, A.; Barton, D.

G.; Kilos, B. A.; Kaminsky, M. P.; Verhoeven, T. W. G. M.; Koers, E. J.; et al. Platinum-Promoted Ga/Al $_2$ O $_3$ as Highly Active, Selective, and Stable Catalyst for the Dehydrogenation of Propane. *Angew. Chemie Int. Ed.* **2014**, *53* (35), 9251–9256.

(14) van Druten, G. M. R.; Aksu, L.; Ponec, V. On the Promotion Effects in the Hydrogenation of Acetone and Propanal. *Appl. Catal. A Gen.* **1997**, *149* (1), 181–187.

(15) Englisch, M.; Ranade, V. S.; Lercher, J. A. Hydrogenation of Crotonaldehyde over Pt Based Bimetallic Catalysts. *J. Mol. Catal. A Chem.* **1997**, *121* (1), 69–80.

(16) Richard, D.; Ockelford, J.; Giroir-Fendler, A.; Gallezot, P. Composition and Catalytic Properties in Cinnamaldehyde Hydrogenation of Charcoal-Supported, Platinum Catalysts Modified by FeCl2 Additives. *Catal. Letters* **1989**, *3* (1), 53–58.

(17) Kitchin, J. R.; Nørskov, J. K.; Barteau, M. A.; Chen, J. G. Role of Strain and Ligand Effects in the Modification of the Electronic and Chemical Properties of Bimetallic Surfaces. *Phys. Rev. Lett.* **2004**, *93* (15).

(18) Balakrishnan, K.; Schwank, J. Neopentane Reactions over Bimetallic PtSn/AI2O3 and PtAu/SiO2 Catalysts. *J. Catal.* **1991**, *132* (2), 451–464.

(19) Michalak, W. D.; Krier, J. M.; Alayoglu, S.; Shin, J.-Y.; An, K.; Komvopoulos, K.; Liu, Z.; Somorjai, G. A. CO Oxidation on PtSn Nanoparticle Catalysts Occurs at the Interface of Pt and Sn Oxide Domains Formed under Reaction Conditions. *J. Catal.* **2014**, *312*, 17–25.

(20) Ammal, S. C.; Heyden, A. Water-Gas Shift Catalysis at Corner Atoms of Pt Clusters in Contact with a TiO2 (110) Support Surface. *ACS Catal.* **2014**, *4* (10), 3654–3662.

(21) Jones, J.; Xiong, H.; DeLaRiva, A. T.; Peterson, E. J.; Pham, H.; Challa, S. R.; Qi, G.; Oh, S.; Wiebenga, M. H.; Pereira Hernández, X. I.; et al. Thermally Stable Single-Atom Platinum-on-Ceria Catalysts via Atom Trapping. *Science* **2016**, *353* (6295), 150–154.

(22) Lucci, F. R.; Liu, J.; Marcinkowski, M. D.; Yang, M.; Allard, L. F.; Flytzani-Stephanopoulos, M.; Sykes, E. C. H. Selective Hydrogenation of 1,3-Butadiene on Platinum-Copper Alloys at the Single-Atom Limit. *Nat. Commun.* **2015**, *6*.

(23) Ro, I.; Sener, C.; Stadelman, T. M.; Ball, M. R.; Venegas, J. M.; Burt, S. P.; Hermans, I.; Dumesic, J. A.; Huber, G. W. Measurement of Intrinsic Catalytic Activity of Pt Monometallic and Pt-MoOx Interfacial Sites over Visible Light Enhanced PtMoOx/SiO2 Catalyst in Reverse Water Gas Shift Reaction. *J. Catal.* **2016**, *344*, 784–794.

(24) Spiewak, B. E.; Shen, J.; Dumesic, J. A. Microcalorimetric Studies of CO and H2 Adsorption on Nickel Powders Promoted with Potassium and Cesium. *J. Phys. Chem.* **1995**, *99* (49), 17640–17644.

(25) Choudhary, V. R.; Mantri, K.; Sivadinarayana, C. Influence of Zeolite Factors Affecting Zeolitic Acidity on the Propane Aromatization Activity and Selectivity of Ga/H-ZSM-5. *Microporous Mesoporous Mater.* **2000**, *37*, 1–8.

(26) Gauthier, C.; Chiche, B.; Finiels, A.; Geneste, P. Influence of Acidity in Friedel-Crafts Acylation Catalyzed by Zeolites. *J. Mol. Catal.* **1989**, *50* (2), 219–229.

(27) Datka, J.; Gil, B.; Kubacka, A. Heterogeneity of OH Groups in H-Mordenites: Effect of Dehydroxylation. *Zeolites* **1996**, *17* (5–6), 428–433.

(28) Bai, P.; Ma, Z.; Li, T.; Tian, Y.; Zhang, Z.; Zhong, Z.; Xing, W.; Wu, P.; Liu, X.; Yan, Z. Relationship between Surface Chemistry and Catalytic Performance of Mesoporous γ-Al2O3 Supported VOX Catalyst in Catalytic Dehydrogenation of Propane. *ACS Appl. Mater. Interfaces* **2016**, *8* (39), 25979–25990.

(29) Mizuno, N.; Tabata, M.; Uematsu, T.; Iwamoto, M. Direct Amination of Lower Alkenes with Ammonia over Zeolite Catalysts. *Stud. Surf. Sci. Catal.* **1994**, *90* (C), 71–76.

(30) Skotak, M.; Lomot, D.; Karpiński, Z. Catalytic Conversion of C6-Alkanes over Pd/Al2O3 Catalysts: The Effect of Support Acidity. *Appl. Catal. A Gen.* **2002**, *229* (1–2), 103–115.

(31) Knifton, J. F.; Dai, P. S. E. Diisopropyl Ether Syntheses from Crude Acetone. *Catal. Letters* **1999**, *57* (4), 193–197.

(32) Moliner, M.; Gabay, J. E.; Kliewer, C. E.; Carr, R. T.; Guzman, J.; Casty, G. L.; Serna, P.; Corma, A. Reversible Transformation of Pt Nanoparticles into Single Atoms inside High-Silica Chabazite Zeolite. *J. Am. Chem. Soc.* **2016**, *138* (48), 15743–15750.

(33) Rode, C. V.; Arai, M.; Nishiyama, Y. Gas Phase Hydrogenation of Acetonitrile over Alumina- and Silica-Supported Platinum Catalysts. *J. Mol. Catal. A Chem.* **1997**, *118* (2), 229–234.

(34) Bartholomew, C. H. Mechanisms of Catalyst Deactivation. *Appl. Catal. A Gen.* **2001**, *212* (1–2), 17–60.

(35) Sachtler, W. M. H.; Stakheev, A. Y. Electron-Deficient Palladium Clusters and Bifunctional Sites in Zeolites. *Catal. Today* **1992**, *12* (2–3), 283–295.

(36) Xu, Y.; Lin, L. Recent Advances in Methane Dehydro-Aromatization over Transition Metal Ion-Modified Zeolite Catalysts under Non-Oxidative Conditions. *Appl. Catal. A Gen.* **1999**, *188* (1–2), 53–67.

(37) Weckhuysen, B. M.; Wang, D.; Rosynek, M. P.; Lunsford, J. H. Conversion of Methane to Benzene over Transition Metal Ion ZSM-5 Zeolites: I. Catalytic Characterization. *J. Catal.* **1998**, *175* (2), 338–346.

(38) Arcoya, A.; Seoane, X. L.; Grau, J. M. Surface Characterization and Dehydrocyclization Activity of Pt/KL Catalysts Prepared by Different Methods. *Appl. Surf. Sci.* **2002**, *205* (1–4), 206–211.

(39) Kim, J.; Kim, W.; Seo, Y.; Kim, J.-C.; Ryoo, R. N-Heptane Hydroisomerization over Pt/MFI Zeolite Nanosheets: Effects of Zeolite Crystal Thickness and Platinum Location. *J. Catal.* **2013**, *301*, 187–197.

(40) Gates, B. C. Supported Metal Clusters: Synthesis, Structure, and Catalysis. *Chem. Rev.* **1995**, *95* (3), 511–522.

(41) Van Den Broek, A. C. M.; Van Grondelle, J.; Van Santen, R. A. Preparation of Highly Dispersed Platinum Particles in HZSM-5 Zeolite: A Study of the Pretreatment Process of

[Pt(NH3)4]2+. *J. Catal.* **1997**, *167* (2), 417–424.

(42) Folefoc, G. N.; Dwyer, J. Dispersion of Platinum in Pt/ZSM-5 Zeolites. *J. Catal.* **1992**, *136* (1), 43–49.

(43) Itoi, H.; Nishihara, H.; Kogure, T.; Kyotani, T. Three-Dimensionally Arrayed and Mutually Connected 1.2-Nm Nanopores for High-Performance Electric Double Layer Capacitor. *J. Am. Chem. Soc.* **2011**, *133* (5), 1165–1167.

Chapter 5. Transient Reaction Kinetics Studies of Acetone Hydrogenation to Isopropanol over Platinum Catalysts[a,b]

5.1 Introduction

Electronic structure calculations studies employing density functional theory are frequently used to model the thermodynamics and surface energetics of adsorbates on supported metal clusters to elucidate the most favorable reaction pathways for a given system. Ideally, these computational efforts are typically in collaboration with experimental studies to develop an in-depth analysis of reactive systems. Numerous case studies for water-gas shift[1–3], methanol synthesis[4], and ethylene hydrogenation, among others[5], have demonstrated the importance of combining theoretical and experimental techniques in catalytic work.

While computational studies generally evaluate surface energetics based on clean catalytic surfaces, many also often explore the coverage dependence of energetic parameters by introducing spectator species onto the metallic surface of interest. Considering the coverage dependencies of these energetic parameters provides a more accurate representation of surface activity under realistic reaction conditions and paves the way for improved modelling of experimental data. To further improve the fundamental understanding of catalytic materials, detailed microkinetic models are frequently employed to bridge the gap between theory and experiment. Many of these

---

[a] This chapter has been adapted from the following publications: (1) Demir, B.; Kropp, T; Rivera-Dones, K. R.; Gilcher, E. B.; Huber, G. W.; Mavrikakis, M.; Dumesic, J.A. “Acetone Hydrogenation on Platinum: A Self-Adjusting Surface” *PNAS* 117 (2020) 3446-3450. (2) Rivera-Dones, K. R.; Demir, B.; Kropp, T.; Huber, G. W.; Mavrikakis, M.; Dumesic, J.A. “Transient Reaction Kinetics Studies of Acetone Hydrogenation to Isopropanol over Platinum Catalysts” *Manuscript under development.*

[b] Author contributions: B.D. and E.B.G. performed steady-state reactivity studies and analyzed data, T.K. performed DFT calculations, B.D. and T.K. developed steady-state microkinetic model, K.R.R.D. performed experimental and theoretical transient kinetic studies. All authors contributed to development and review of their corresponding manuscripts.

models aim to predict the working mechanism of a chemical reaction by employing the Langmuir adsorption isotherm, where site adsorption is assumed to be independent of the presence of particles already adsorbed at neighboring sites.[6,7] Generally, the Langmuir models are valid for systems in which the catalytic surface operates under a low coverage of reactive adsorbates. For those reactive systems that operate under high surface coverage, however, the underlying assumptions of the Langmuir model lose validity and the effects of nearest-neighbor site occupancy on site adsorption energetics must be taken into account. Adsorbate-adsorbate interactions can significantly change the energy of adsorption and desorption steps as well as alter the stability of transition states, thus affecting catalytic rates.[7–10] The Bragg-Williams approximation is one such way to estimate the effects of adsorbate/adsorbate interactions in terms of the occupancy of nearest-neighbor sites.[6,11,12] By including the effects of surface coverage in a dynamic way, microkinetic models using the Bragg-Williams approximation are capable of more accurately capturing the fundamental kinetics that govern highly covered catalytic surfaces.[11,13,14]

Although catalytic experiments and microkinetic models have been extensively used to describe steady-state reactivity, these studies have been seldom combined for transient studies of catalytic materials. The use of the steady-state isotopic transient kinetic analysis (SSITKA) technique developed by Happel[15], Bennet[16], and Biloen[17] has been applied to a variety of reaction systems including, among others, ammonia synthesis[18–21], oxygenation[22–24], hydrogenolysis[25], isomerization[26,27], ethanol coupling[28] and hydrogenation[29–32] reactions. The SSITKA technique allows for the elucidation of potential reaction mechanisms as well as *in-situ* determination and quantification of important kinetic parameters, including surface coverages of reaction intermediates and surface residence times[33]. When combined with theoretical models, experimental transient techniques could provide a deeper level of fundamental understanding about a catalyst surface than can be achieved by analyzing catalytic materials using steady-state studies alone.

We have recently developed a steady-state microkinetic model for acetone hydrogenation over platinum that uses DFT-derived thermodynamic properties and surface energetics to explore the importance of adsorbate coverage on the overall reactivity of the platinum surface at 353 K.[14] Models evaluating both static and dynamic inclusion of surface coverage effects into adsorbate energetics using the Langmuir and Bragg-Williams approximations, respectively, were able to describe the experimentally measured steady-state reactivity. Therefore, we have employed transient reaction kinetics studies to elucidate further the effects of surface coverage on the reactivity of platinum catalysts for acetone hydrogenation. In the present work, we evaluate the importance of surface coverage on the acetone hydrogenation reaction by comparing the transient behavior of Pt-based catalysts following either the removal of acetone or its substitution in the reactant feed. In this manner, we provide experimental evidence for the existence of a highly covered surface and the importance of incorporating surface coverage effects dynamically into energetic parameters for microkinetic modeling of acetone hydrogenation over a platinum surface.

5.2 Materials and Methods

5.2.1 Catalyst Synthesis

A Pt/SiO_2 catalyst was prepared using a commercial SiO_2 (Davisil Grade 646, Sigma-Aldrich) as the support. The desired amount of the tetraamineplatinum(II) nitrate precursor ($Pt(NH_3)_4(NO_3)$, Sigma-Aldrich) to achieve a 3 wt% Pt catalyst was dissolved in Milli-Q water and added to the silica support via incipient wetness impregnation. Following impregnation, the catalyst was dried overnight at 383 K and calcined in flowing air at 573 K for 2 h. The calcined catalyst was then reduced at 773 K in flowing H_2 for 6 h and passivated at room temperature using 1% O_2 in He (Airgas).

A commercial α-Al_2O_3 (99.99%, Alfa Aesar) was used as the support for the Pt/α-Al_2O_3 catalyst. Platinum was deposited onto the support via incipient wetness impregnation using an aqueous solution of the tetraamineplatinum(II) nitrate precursor. Due to the low surface area of the α-Al_2O_3 support, the impregnation process required intermediate drying steps at 383 K to avoid exceeding the incipient point during deposition. Following impregnation, the catalyst was dried at 383 K for 0.5 h and calcined in air at 573 K for 1 h (at a heating rate of 6 K/min).

Additional metal oxides were used in this study to evaluate support effects, including a ZSM-5 zeolite, a hydrophobic SiO_2 (Aerosil R-812S, Evonik Industries), and MgO (Nanoscale Materials). A commercial NH_4-ZSM-5 material (Zeolyst, $SiO_2/Al_2O_3 = 280$) was calcined in air at 873 K for 18 h to remove ammonia and obtain the H-ZSM-5 form. All other supports were used as obtained.

5.2.2 Catalyst Characterization

ICP-OES measurements were carried out by digesting 10 mg of catalyst in a mixture containing 2.5 g HNO_3 (Fisher, 65 wt%) and 7.5 g HCl (Fisher, 37wt%) under reflux at 393 K for 12 h. After digestion, the mixture was cooled to room temperature, diluted in Milli-Q water, and filtered. Standard solutions were prepared from commercial Pt ICP standards (Alfa Aesar, 1000 mg/mL). The filtered catalyst samples and Pt standards were analyzed using a Varian Vista-MPX ICP-OES spectrometer (Agilent Technologies Inc).

The number of surface Pt sites was measured using a volumetric gas handling system. Pressure was monitored with Baratron capacitance manometers ($\pm 0.5\times10^{-4}$ Torr), allowing for precise pressure measurements, as described in detail elsewhere.[34] The catalysts were reduced under H_2 flow for 1 h at 723 K and CO adsorption was performed at 293 K after reduction. The adsorption stoichiometry between CO and surface Pt sites was assumed to be 0.7:1.

5.2.3 Acetone Hydrogenation Reaction

The hydrogenation of acetone (HPLC grade, Sigma-Aldrich) to isopropanol (IPA) was carried out in a ¼” OD stainless steel downward flow reactor placed inside a tube furnace attached to the system shown in Figure 5.1. The catalyst bed consisted of the catalyst powder resting at the center of the reactor on a plug of quartz wool, followed by a bed of silica chips used to minimize the reactor void volume downstream of the catalyst. The reactor temperature was measured and controlled by a K-type thermocouple that was inserted from the top of the reactor tube into the middle of the catalyst bed. Prior to reaction kinetics studies, the catalyst bed was reduced *in situ* for 2 h at 573 K in flowing H_2 at 20 cm^3/min. After reduction, the reactor was allowed to cool to a reaction temperature of 353 K under flowing H_2. Acetone was then fed into the system by flowing 5 cm^3/min of a 95% He/5% Ar mixture (Airgas) through a saturator held at 267 K. The acetone/inert stream was mixed with hydrogen to obtain total flow rates between 20 – 70 cm^3/min. Speciation and quantification of the reactor effluent was carried out by a Shimadzu 2014 GC equipped with a Rt-QS-Bond column (0.53 mm ID, 30 m length) and a Flame Ionization Detector (FID).

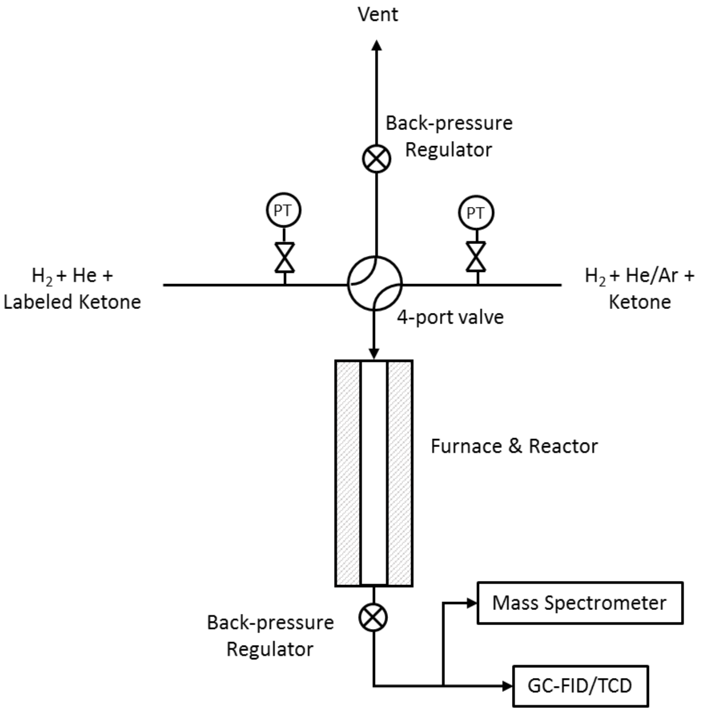

Figure 5.1. Reaction system used for transient kinetic studies of acetone hydrogenation.

5.2.4 Transient Kinetic Analysis

The transient kinetic analysis discussed in this work was performed using a procedure analogous to the Steady-State Isotopic Transient Kinetic Analysis (SSITKA) technique[33,35]. In the transient studies performed herein, the acetone hydrogenation reaction was allowed to reach steady state before abruptly switching the reactant feed to one that contains a different, but structurally similar, ketone. A similar approach has been recently adopted by Kammert et al. for transient reaction studies on the reduction of propionic acid[36]. A typical transient response following the isobaric reactant switch from acetone to 2-pentanone is shown in Figure 5.2. The gas-phase hold up of the reactor system is determined by integrating the decay response of an argon tracer, assuming that no interaction takes place between the tracer and the catalyst surface[33,36]. Similar to the analyses performed during traditional SSITKA experiments, reaction kinetics parameters can be derived from the normalized transient response curve of each individual species (F_i).

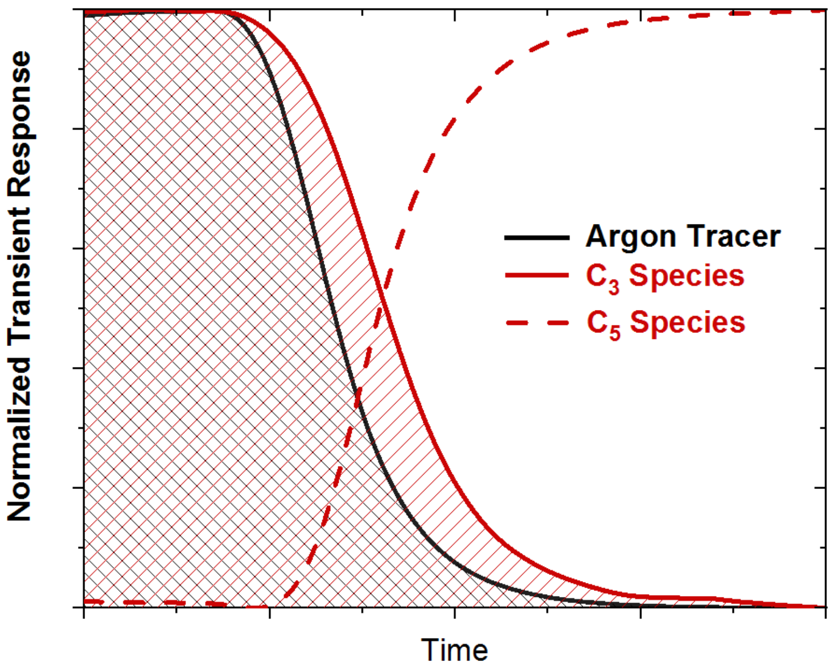

Figure 5.2: Theoretical transient response for a C_3 to C_5 ketone feed switch. Gas-phase holdup is accounted for by the decay of the argon tracer (black) when evaluating mean surface residence time from the C_3 species decay (solid red) and C_5 substitution (dashed red).

The mean surface residence time of each species (τ_i) can be determined by integrating the normalized transient response curve and correcting for the inert tracer response (F_{Ar}) according to Equation 1.

$$\tau_i = \int_{t_0}^{\infty} (F_i - F_{Ar})\, dt \tag{1}$$

The number of catalytically active sites that lead to the formation of IPA were determined based on the difference between the total moles of IPA detected during the transient and those already present in the gas phase at steady-state before the reactant switch. The molar ratio of gas-phase IPA ($IPA_{g,SS}$) to inert tracer (Ar_{SS}) established at steady-state was assumed to remain constant throughout the transient, which allows calculation of the moles of alcohol present in the gas phase during the transient ($IPA_{g,trans}$) as shown in Equation 2. The total moles of argon detected during the transient (Ar_{trans}) were determined by integrating the raw data for the argon molar rate transient response curve over the duration of the transient.

$$mol\ IPA_{g,trans} = \frac{mol\ IPA_{g,SS}}{mol\ Ar_{SS}} * mol\ Ar_{trans} \quad (2)$$

Integration of the molar rate transient response curve for IPA led to the overall moles of IPA eluted during the transient ($IPA_{tot,trans}$). Equation 3, which isolates the moles of IPA desorbing from the catalyst surface during the transient experiment, was then used to determine the true number of catalytically active sites participating in IPA formation (N_{IPA}).

$$N_{IPA} = mol\ IPA_{tot,trans} - mol\ IPA_{g,trans} \quad (3)$$

Two types of transient reaction experiments were performed in this work. The first type of experiment was a reactive transient induced by switching the ketone feed from acetone to 2-pentanone, as previously mentioned. In this method, the acetone hydrogenation reaction was allowed to reach steady-state, at which point flow was started through a second feed and saturator system containing the C_5 ketone. Once flow through the second feed system had stabilized and the system pressures equalized, the reactant feeds were switched via the automated 4-port valve shown in Figure 5.1. Transient monitoring and data collection were performed directly by an online MKS Cirrus 2 mass spectrometer (MS). In the MS, the ion signals for m/z = 58 (acetone), 45 (IPA), and 40 (argon) were continuously monitored during transients. The raw data for all three signals were corrected to remove contributions from the C_5 species, based on established fragmentation patterns and in-house calibrations.

The second type of experiment performed was a desorption-transient experiment, which involved replacing the acetone-containing feed stream with a second feed composed solely of hydrogen and inert gas. All other parameters, data monitoring, and analysis techniques remained the same between the two types of transient experiments.

5.2.5 Computational Methods

The Pt(111) surface was modeled using a *p*(3x3) cell with three atomic layers; the lowest atomic layer was frozen to simulate the bulk. DFT calculations were conducted under periodic boundary conditions using VASP[37,38]. The PBE functional was applied to determine exchange-correlation energies with an energy cutoff of 600 eV[39], and van der Waals interactions were incorporated using the semi-empirical C_6/R^6 term by Grimme (DFT+D2)[39,40]. Structure optimizations were performed until total energies were converged to 10^{-6} eV, and forces acting on the relaxed ions were below 0.02 eV/Å. Structures were proven to be minima by the absence of imaginary frequencies. Additional details on the computational methods can be found in a recent report.[14]

5.3 Results and Discussion

5.3.1 Theoretical model for the transient behavior of acetone hydrogenation over platinum

A steady-state microkinetic model incorporating DFT-derived thermodynamic parameters and surface energetics has recently been developed for acetone hydrogenation over a Pt(111) surface.[14] Based on results from DFT calculations, the favored pathway for acetone hydrogenation to isopropanol over a platinum surface was found to occur via a hydroxypropyl intermediate, $C_3H_6OH^*$, as shown in Scheme 5.1. Previous work explored the significance of coverage-dependent energetics on steady-state reaction kinetics using microkinetic models based on Scheme 5.1 that incorporated both Langmuir behavior and Bragg-Williams approximations to kinetically-relevant energetic parameters.

1. $C_3H_6O + * \leftrightarrow C_3H_6O*$
2. $H_2 + 2* \leftrightarrow 2H*$
3. $C_3H_6O* + H* \leftrightarrow C_3H_6OH* + *$
4. $C_3H_6OH* + H* \leftrightarrow C_3H_7OH* + *$
5. $C_3H_7OH* \leftrightarrow C_3H_7OH + *$

Overall. $C_3H_6O + H_2 \leftrightarrow C_3H_7OH$

Scheme 5.1. The theoretically favored pathway for the hydrogenation of acetone via a hydroxypropyl intermediate, as determined by DFT calculations and the steady-state microkinetic model.[14]

Under each scenario, the coverage dependence was included either statically by neglecting interactions between adsorbates (Langmuir behavior) or dynamically by estimating adsorbate interaction effects linearly in terms of nearest neighbor site occupancy (Bragg-Williams approximation)[41,42]. Results from this previous work ultimately showed that steady-state kinetic data, including apparent activation barriers along with acetone and hydrogen reaction orders, was best described over a wide range of conditions by microkinetic models that dynamically accounted for surface coverage effects using the Bragg-Williams approximations. As shown in Figure 5.3, DFT calculations for the adsorbed species of Scheme 4.1 demonstrated that a more energetically favorable reaction pathway exists when the effects of pre-adsorbed MARI species on adsorbate binding strength are accounted for. Additional details on the DFT calculations, the steady-state microkinetic model, and how the Langmuir and Bragg-Williams approximations were incorporated can be found in a recent publication[14].

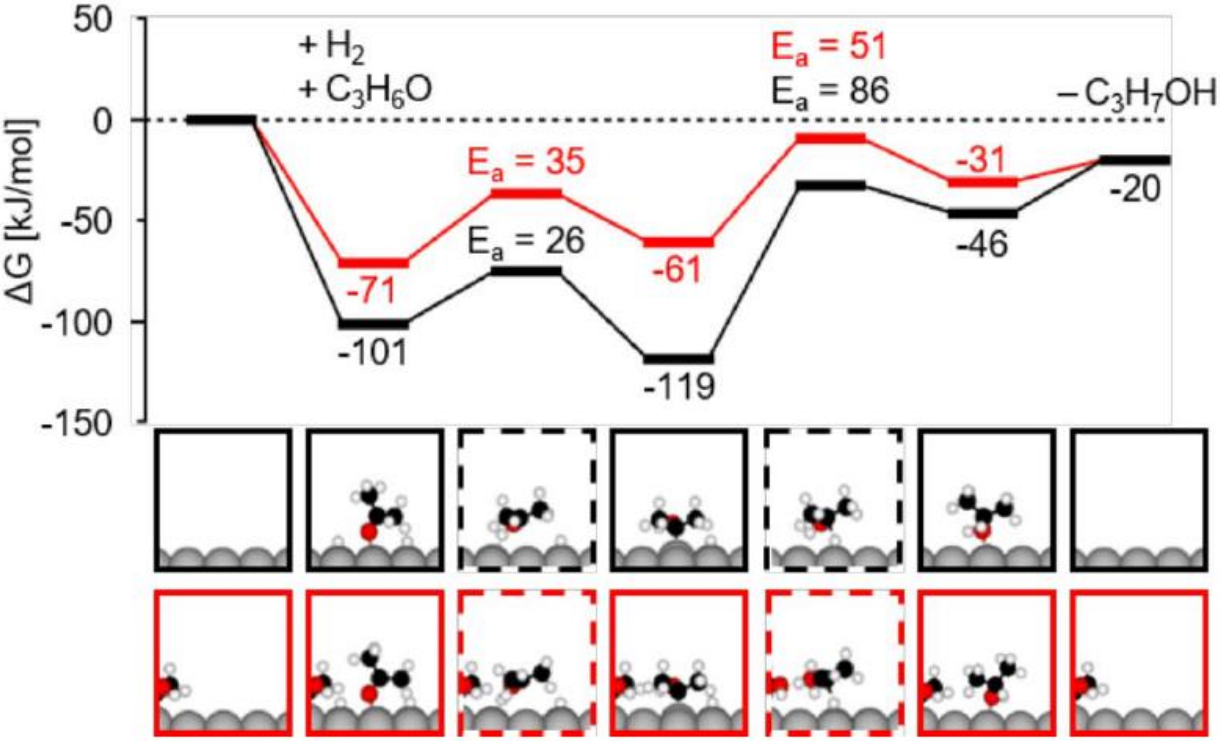

Figure 5.3. Gibbs free energy diagram for the acetone hydrogenation mechanism over a clean platinum surface (black) and in the presence of pre-adsorbed MARI species (red). The molecular structures shown use the following color code: C (black), H (white), O (red), Pt (gray), and the dashed boxes indicate transition states.

Transient reaction kinetics studies generally monitor the time-decay response of a reactant species following either its removal or substitution in the feed stream while maintaining a constant total flow rate. Accordingly, the microkinetic models using Langmuir and Bragg-Williams approximations were used to analyze the transient response of the acetone hydrogenation reaction following the removal of acetone from the feed (desorption) and substitution of the ketone by its isotopically-labeled counterpart (SSITKA). Langmuir model predictions for the normalized transient response and the surface coverage of $C_3H_6OH^*$ as the most abundant reactive intermediate (MARI) for both transient cases are shown in Figure 5.4. As can be observed from Figure 5.4, the Langmuir models predict transients on the order of seconds for the acetone and isopropanol species. The models also show minimal delay between removal of an inert tracer and complete acetone elution, suggesting negligible interaction between acetone and the catalyst surface, as expected based on the energetic parameters determined by DFT and shown in Table 5.1 More importantly, predictions for the desorption and SSITKA cases with Langmuir models show similar transient responses for the ketone and alcohol species, as well as complete removal of the MARI species from the catalytic surface for both transient types.

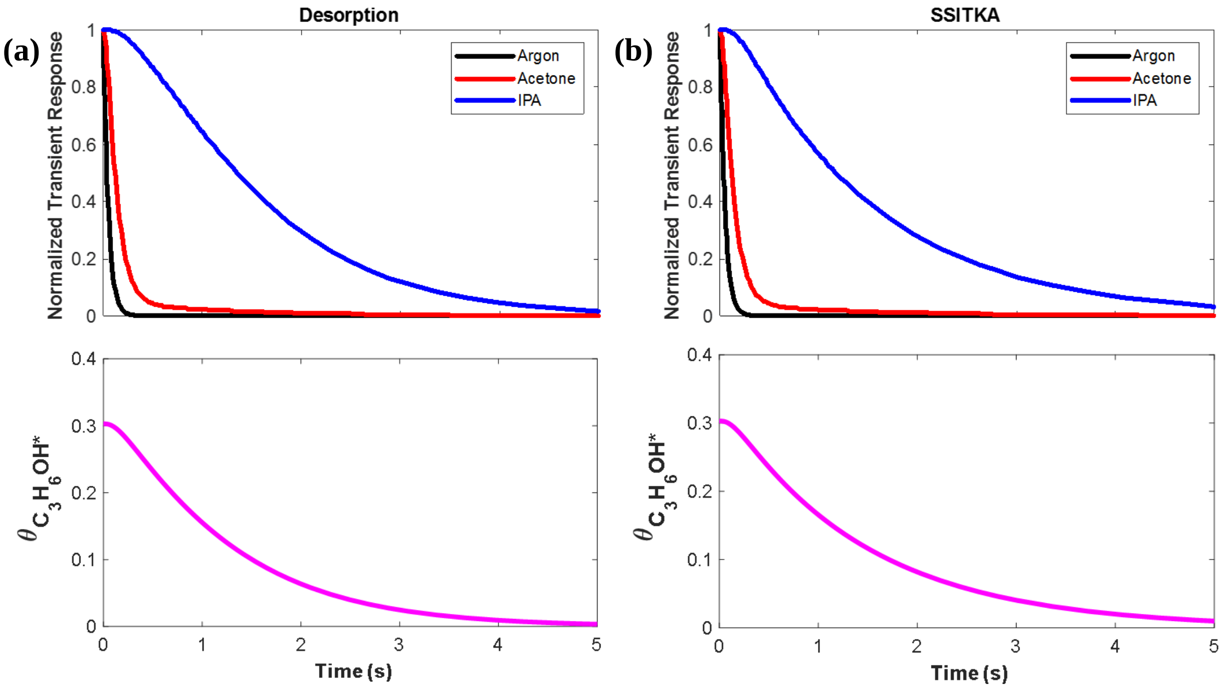

Figure 5.4. Langmuir model predictions for the transient response of the acetone (red), isopropanol (blue), and argon tracer (black) flow rates along with the fractional surface coverage of the MARI (pink) for **(a)** desorption and **(b)** SSITKA transients.

Table 5.1. Energetic parameters for the adsorbed species of interest on a clean Pt(111) surface.

Adsorbed Species	Binding Energy (kJ/mol)	Adsorption Entropy (J/mol-K)
$C_3H_6O^*$	-89	135
H*	-266	9
$C_3H_6OH^*$	-282	109
$C_3H_7OH^*$	-99	133
$C_5H_{10}O^*$	-112	179

Predictions for desorption and SSITKA experiments are shown in Figure 5.5 for microkinetic models based on dynamic incorporation of the MARI surface coverage via the Bragg-Williams approximation. While the transients are still predicted to be of the order of seconds, the Bragg-Williams models show a difference in the elution delay of the alcohol product between the desorption and SSITKA transients that was not observed with the Langmuir model predictions. Specifically, the Bragg-Williams models predict a longer decay time for the isopropanol product during a SSITKA transient than that predicted for the desorption transient, suggesting that more isopropanol is released from the surface during a SSITKA transient than during a desorption transient. The Bragg-Williams models show that surface coverage by the MARI changes minimally during a transient induced by removal of the reactant acetone species. In fact, the model does not predict complete removal of the MARI species from the catalyst surface even after extended desorption times. This behavior suggests that coverage effects suppress the ability to decrease the presence of the MARI species solely by desorption due to an increase in the interaction strength between the MARI and the catalyst surface. On the other hand, the SSITKA model predicts complete removal of the MARI species upon substitution of the ketone in the reactant feed, which suggests that the platinum surface will remain highly covered unless the adsorbates are displaced from the surface by new reactive intermediates.

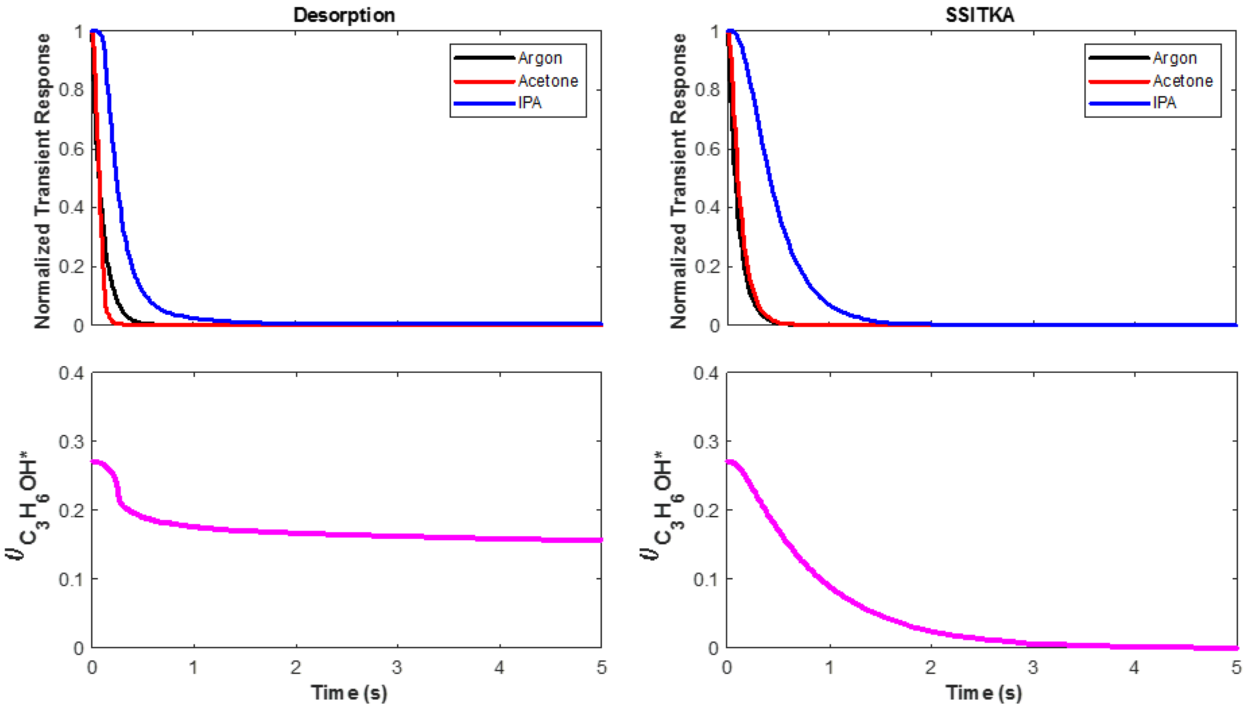

Figure 5.5. Bragg-Williams model predictions for the transient response of the acetone (red), isopropanol (blue), and argon tracer (black) flow rates along with the fractional surface coverage of the MARI (pink) for **(a)** desorption and **(b)** SSITKA transients.

5.3.2 Experimental Transient Kinetic Analyses

To probe the aforementioned predictions of the microkinetic models, we carried out desorption and reactive transients over supported platinum catalysts using the apparatus described in Section 5.2.3. To this effect, a 3 wt% Pt/SiO_2 catalyst was used to hydrogenate acetone at 353 K in a packed bed reactor. Once the reaction achieved steady state, acetone was abruptly removed from the feed stream while maintaining a constant overall flowrate to induce a transient by desorption. The transient response for argon, acetone, and isopropanol under desorption conditions is shown in Figure 5.6. In this Figure, t = 0 marks the point at which the feed switch was made, and the decay of the argon tracer can be used as an indicator of the hold-up time in the system based on the assumption that it is a fully inert species and does not interact with the catalyst bed. Therefore, it follows that the decay of the reactant and product species relative to that of argon is indicative of the residence time of each species on the catalyst bed.

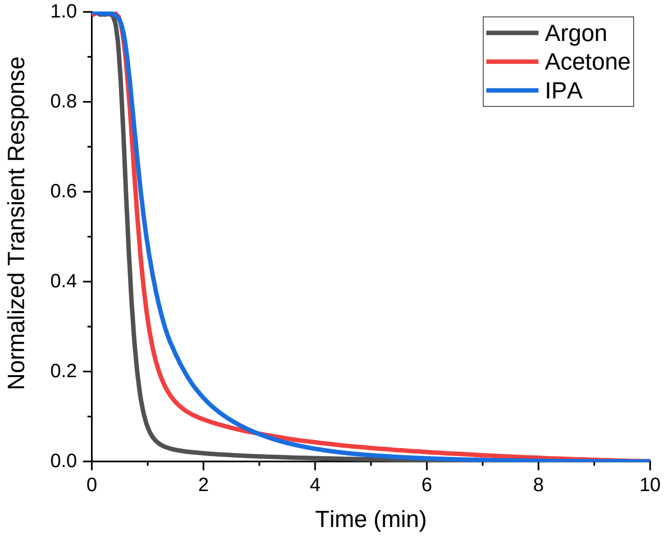

Figure 5.6: Normalized transient response of an argon tracer (black), acetone (red), and isopropanol (blue) over a 3 wt% Pt/SiO_2 catalyst following the removal of acetone from the feed stream. Reaction conditions: 40 mg catalyst, T = 353 K, P = 15 psi, F_{tot} = 20 cm^3/min.

The decay response of isopropanol shown in Figure 5.6 is qualitatively consistent with that predicted by the theoretical models. On the other hand, the acetone response in Figure 5.6 suggests that a significant interaction exists between the acetone reactant and the catalyst surface, which was not apparent from the theoretical predictions. More importantly, the detailed steady-state microkinetic models showed that a negligible surface coverage by acetone was expected, as the hydropropoxyl intermediate and adsorbed hydrogen were predicted to be the primary adsorbates on the catalytic surface[14]. Thus, the decay response could be indicative of acetone interaction with other system components. Control experiments with an acetone-containing feed at typical reaction conditions were performed on the reactor, its packing components, and the bare catalyst support. These experiments – the results of which can be seen in Figure 5.7 – showed no noticeable interaction between acetone and the reactor walls, the silica chips, or the quartz wool used to pack the catalyst bed. In contrast, acetone was found to adsorb on the silica support under reaction conditions, yielding a decay response similar to that observed over the Pt/SiO_2 catalyst. Based on these control experiments, the acetone decay in Figure 5.6 is a direct result of its interaction with the silica support and not solely with the platinum surface. Similar controls were performed with an isopropanol feed under typical reaction conditions. The results for these IPA controls are also shown in Figure 5.7, where they have been overlaid with the acetone controls for simplicity. From these results, it can be seen that the alcohol also had non-negligible interactions with the SiO_2 surface. Therefore, a more inert catalyst support was needed to experimentally probe transient reaction kinetics over a platinum surface.

To identify a more suitable support, control experiments were performed on a variety of metal oxides, including ZSM-5, MgO, hydrophobic SiO_2, and α-Al_2O_3. As shown in Figure 5.7, all supports studied demonstrated significant adsorption of the ketone and alcohol, with α-Al_2O_3 being the notable exception due likely to its considerably lower surface area when compared to the other materials. Accordingly, the performance of an 8 wt% Pt/α-Al_2O_3 catalyst in the acetone hydrogenation reaction was studied under transient reaction conditions induced by desorption, and the results are shown in Figure 5.8a. The desorption transients shown in Figure 5.7 for both acetone and isopropanol demonstrated negligible adsorption of either species on the α-Al_2O_3 support, therefore confirming that the transients in Figure 5.8a are representative of the interactions with the platinum surface. A mean surface residence time (τ_{IPA}) of 3.1 s for the isopropanol species on platinum can be obtained by integrating the area between the argon and isopropanol curves for this desorption experiment. The magnitude of τ_{IPA} suggests that only a small amount of isopropanol leaves the platinum surface upon removal of acetone from the reactant feed.

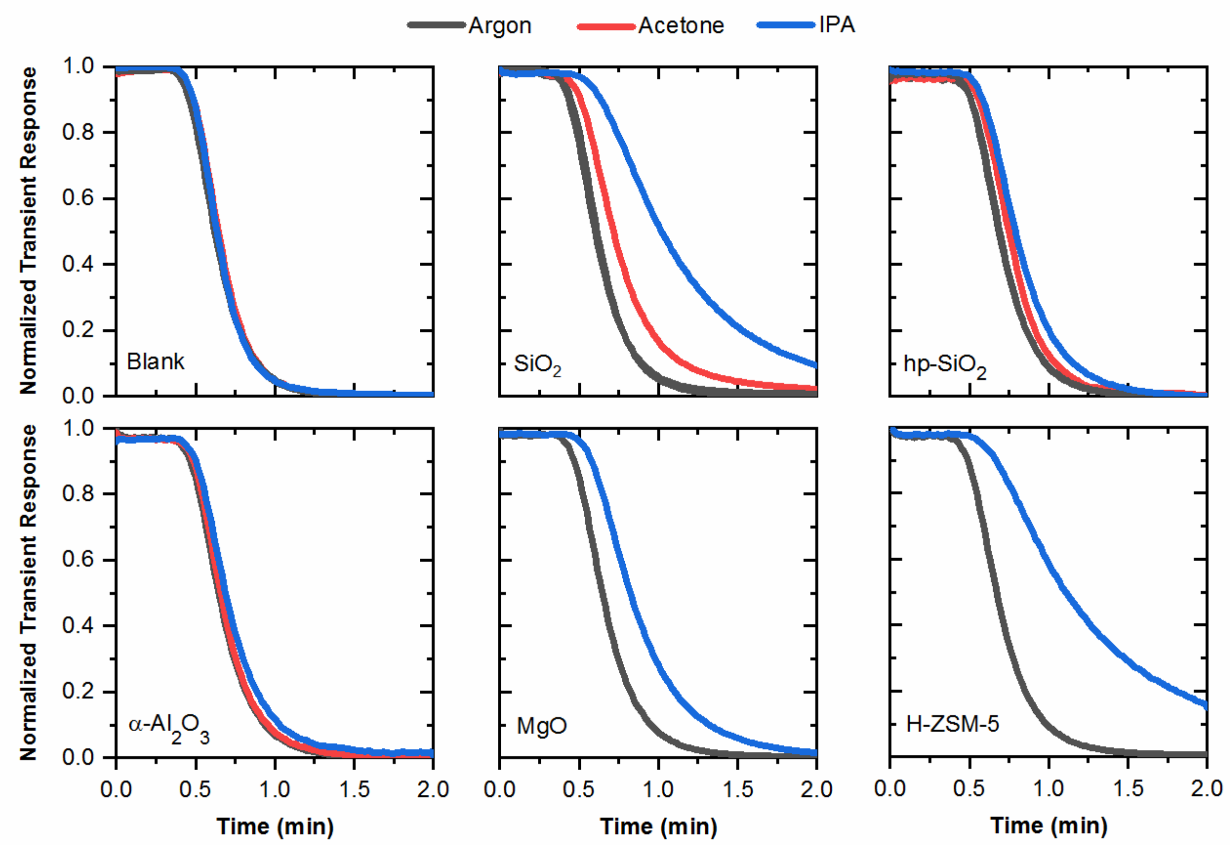

Figure 5.7: Normalized transient responses for argon (black), acetone (red), and IPA (blue) during control experiments over a reactor packed with silica chips and quartz wool (Blank), a silica support (SiO_2), hydrophobic silica (hp-SiO_2), alpha-alumina (α-Al_2O_3), magnesium oxide (MgO), and ZSM-5 zeolite (H-ZSM-5, SiO_2/Al_2O_3 = 280). No acetone responses were collected for MgO and H-ZSM-5.

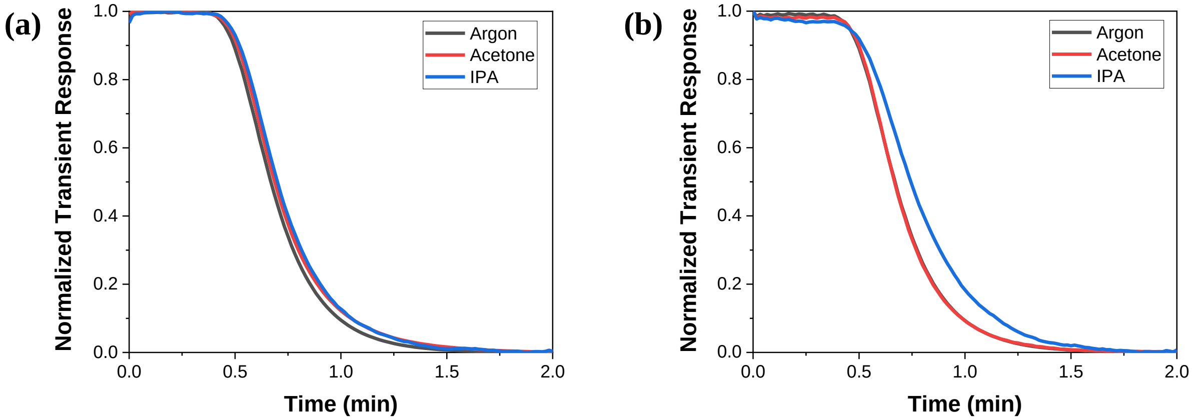

Figure 5.8: Normalized transient response of an argon tracer (black), acetone (red), and isopropanol (blue) over an 8 wt% Pt/α-Al_2O_3 catalyst following **(a)** the removal of acetone from the feed stream and **(b)** substitution of acetone with 2-pentanone. Reaction conditions: 10 mg catalyst, T = 353 K, P = 15 psi, F_{tot} = 20 cm^3/min.

To explore the effects of surface coverage, a reactive transient was experimentally induced over the Pt/α-Al_2O_3 by substituting, instead of removing, the acetone reactant in the feed. In traditional SSITKA studies, the substituent species is an isotopically-labeled version of the original reactant. Here, we have employed an analogous method in which acetone was substituted by a structurally similar ketone, i.e. 2-pentanone, akin to the recent work by Davis and coworkers[36]. The results of this reactive transient are shown in Figure 5.8b. The most notable feature of the transient shown in Figure 5.8b is the longer decay of the isopropanol curve compared to that observed during the desorption transient in Figure 5.8a. A mean surface residence time for isopropanol of 6.4 s was estimated for the reactive transient, which is approximately twice as long as that observed during desorption. This behavior suggests that a larger number of surface species (i.e., $C_3H_6OH^*$) conducive to the formation of isopropanol can be displaced from the catalyst surface by the incoming 2-pentanone system. Using Equation 3, the active site density for this scenario was estimated to be 52 μmol/g_{cat}, which is almost four times larger than the estimated active site density of 15 μmol/g_{cat} determined from the desorption transient in Figure 5.8a.

We note that the active site density values obtained from each of the transients are higher than the site density obtained via CO chemisorption measurements (11 μmol/g_{cat}). This discrepancy could be indicative of surface re-adsorption effects, which would lead to an artificially high site count as molecules occupy multiple sites before finally desorbing into the gas phase. To probe for re-adsorption effects, the surface residence times and active site counts were evaluated as a function of total flow rates for both transient scenarios. As shown in Figure 5.9, there is a non-zero slope for all curves under both transient conditions, thus confirming the presence of surface re-adsorption effects. By extrapolating each curve to infinitely fast flowrates (1/F = 0), the intrinsic values for τ_{IPA} and N_{IPA} can be estimated in the absence of re-adsorption effects. Using this methodology, the intrinsic surface residence times ($\tau_{IPA,0}$) for desorption and reactive transients obtained were 1.8 s and 2.2 s, respectively. More importantly, the intrinsic site density ($N_{IPA,0}$) for a desorption transient was determined to be 2.6 μmol/g_{cat}, while that for a reactive transient was found to be 10.7 μmol/g_{cat}. The difference in $N_{IPA,0}$ values confirms that a significant amount of adsorbed intermediates remains on the catalyst surface following removal of the acetone feed, and those intermediates can only be removed by introducing an alternative reactant species to displace them from the platinum surface. Moreover, the intrinsic site density obtained for the reactive transient is in agreement with the active site density determined via CO chemisorption, which suggests full removal of the MARI species from the surface can be achieved following substitution of the reactant ketone. This behavior is in agreement with the Bragg-Williams model discussed in Section 5.3.1, where the surface coverage of the MARI species conducive to the formation of isopropanol remained relatively unchanged under transient conditions induced by desorption but could be completely removed from the catalytic surface by means of a reactive transient.

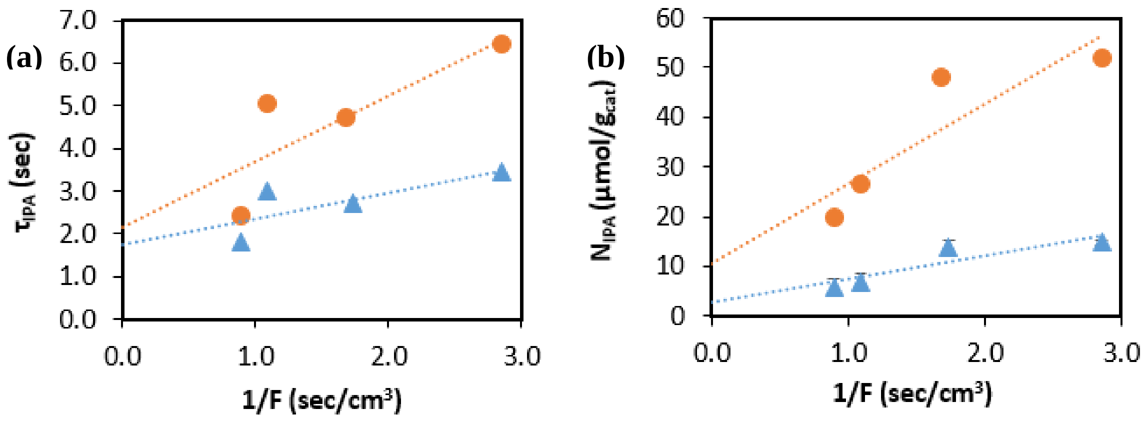

Figure 5.9: (a) IPA surface residence time, τ_{IPA}, and (b) site density, N_{IPA}, as a function of inverse total flow rate for reactive (orange circles) and desorption (blue triangles) transients.

In this manner, we have used transient kinetic studies to show that the acetone hydrogenation reaction over platinum proceeds via a catalytic surface that is highly covered by a reactive hydroxypropyl intermediate species. Importantly, we have provided experimental evidence to support the use of dynamically adjusted coverage-dependent energetic parameters via the Bragg-Williams approximation within theoretical microkinetic models to properly predict the reactivity of platinum catalysts for acetone hydrogenation.

5.4 Conclusions

Transient reaction kinetics studies have been used to characterize the surface of platinum catalysts during the hydrogenation of acetone to isopropanol. Experimental transient responses showed that full removal of the MARI from the catalytic surface could only be achieved following substitution of acetone in the feed by a similarly structured ketone, thus providing evidence for the existence of a highly covered catalytic surface under steady-state conditions. Experimental results validated the importance of surface coverage effects in theoretical models, as only energetic parameters including dynamic surface coverage dependencies via the Bragg-Williams approximation were able to accurately describe the experimental behavior observed.

5.5 References

(1) Grabow, L. C.; Gokhale, A. A.; Evans, S. T.; Dumesic, J. A.; Mavrikakis, M. Mechanism of the Water Gas Shift Reaction on Pt: First Principles, Experiments, and Microkinetic Modeling. *J. Phys. Chem. C* **2008**, *112* (12), 4608–4617.

(2) Tibiletti, D.; Amieiro-Fonseca, A.; Burch, R.; Chen, Y.; Fisher, J. M.; Goguet, A.; Hardacre, C.; Hu, P.; Thompsett, D. DFT and in Situ EXAFS Investigation of Gold/Ceria-Zirconia Low-Temperature Water Gas Shift Catalysts: Identification of the Nature of the Active Form of Gold. *J. Phys. Chem. B* **2005**, *109* (47), 22553–22559.

(3) Zhao, Z. J.; Li, Z.; Cui, Y.; Zhu, H.; Schneider, W. F.; Delgass, W. N.; Ribeiro, F.; Greeley, J. Importance of Metal-Oxide Interfaces in Heterogeneous Catalysis: A Combined DFT, Microkinetic, and Experimental Study of Water-Gas Shift on Au/MgO. *J. Catal.* **2017**, *345*, 157–169.

(4) Yang, Y.; Mims, C. A.; Mei, D. H.; Peden, C. H. F.; Campbell, C. T. Mechanistic Studies of Methanol Synthesis over Cu from CO/CO 2/H2/H2O Mixtures: The Source of C in Methanol and the Role of Water. *J. Catal.* **2013**, *298*, 10–17.

(5) Flaherty, D. W.; Hibbitts, D. D.; Gürbüz, E. I.; Iglesia, E. Theoretical and Kinetic Assessment of the Mechanism of Ethane Hydrogenolysis on Metal Surfaces Saturated with Chemisorbed Hydrogen. *J. Catal.* **2014**, *311*, 350–356.

(6) Ceyrolles, W. J.; Viot, P.; Talbot, J. Kinetics of Heterogeneous Adsorption: Mean-Field Theory and Simulations. *Langmuir* **2002**, *18* (4), 1112–1118.

(7) Lausche, A. C.; Medford, A. J.; Khan, T. S.; Xu, Y.; Bligaard, T.; Abild-Pedersen, F.; Nørskov, J. K.; Studt, F. On the Effect of Coverage-Dependent Adsorbate-Adsorbate Interactions for CO Methanation on Transition Metal Surfaces. *J. Catal.* **2013**, *307*, 275–282.

(8) Grabow, L. C.; Hvolbæk, B.; Nørskov, J. K. Understanding Trends in Catalytic Activity: The Effect of Adsorbate-Adsorbate Interactions for Co Oxidation over Transition Metals. In *Topics in Catalysis*; 2010; Vol. 53, pp 298–310.

(9) Getman, R. B.; Schneider, W. F. DFT-Based Coverage-Dependent Model of Pt-Catalyzed NO Oxidation. *ChemCatChem* **2010**, *2* (11), 1450–1460.

(10) Lu, J.; Behtash, S.; Faheem, M.; Heyden, A. Microkinetic Modeling of the Decarboxylation and Decarbonylation of Propanoic Acid over Pd(1 1 1) Model Surfaces Based on Parameters Obtained from First Principles. *J. Catal.* **2013**, *305*, 56–66.

(11) Kundu, A.; Piccini, G.; Sillar, K.; Sauer, J. Ab Initio Prediction of Adsorption Isotherms for Small Molecules in Metal-Organic Frameworks. *J. Am. Chem. Soc.* **2016**, *138* (42), 14047–14056.

(12) Feng, J.; Lansford, J.; Mironenko, A.; Pourkargar, D. B.; Vlachos, D. G.; Katsoulakis, M. A. Non-Parametric Correlative Uncertainty Quantification and Sensitivity Analysis: Application to a Langmuir Bimolecular Adsorption Model. *AIP Adv.* **2018**, *8* (3), 035021.

(13) Al-Muhtaseb, S. A.; Ritter, J. A. Roles of Surface Heterogeneity and Lateral Interactions

on the Isosteric Heat of Adsorption and Adsorbed Phase Heat Capacity. *J. Phys. Chem. B* **1999**, *103* (13), 2467–2479.

(14) Demir, B.; Kropp, T.; Rivera-Dones, K. R.; Gilcher, E. B.; Huber, G. W.; Mavrikakis, M.; Dumesic, J. A. A Self-Adjusting Platinum Surface for Acetone Hydrogenation. *Proc. Natl. Acad. Sci. U. S. A.* **2020**, *117*, 3446–3450.

(15) Happel, J. Transient Tracing. *Chemical Engineering Science*. 1978.

(16) BENNETT, C. O. Understanding Heterogeneous Catalysis Through the Transient Method; 1982; pp 1–32.

(17) Biloen, P. Transient Kinetic Methods. *J. Mol. Catal.* **1993**, *21* (1–3), 17–24.

(18) McClaine, B. C.; Davis, R. J. Importance of Product Readsorption during Isotopic Transient Analysis of Ammonia Synthesis on Ba-Promoted Ru/BaX Catalyst. *J. Catal.* **2002**, *211* (2), 379–386.

(19) Davis, R. J.; McClaine, B. C. Isotopic Transient Kinetic Analysis of Cs-Promoted Ru/MgO during Ammonia Synthesis. *J. Catal.* **2002**.

(20) Siporin, S. E.; Davis, R. J. Isotopic Transient Analysis of Ammonia Synthesis over Ru/MgO Catalysts Promoted by Cesium, Barium, or Lanthanum. *J. Catal.* **2004**, *222* (2), 315–322.

(21) Nwalor, J. U.; Goodwin, J. G.; Biloen, P. Steady-State Isotopic Transient-Kinetic Analysis of Iron-Catalyzed Ammonia Synthesis. *J. Catal.* **1989**, *117* (1), 121–134.

(22) Calla, J. T.; Davis, R. J. Investigation of Alumina-Supported Au Catalyst for CO Oxidation by Isotopic Transient Analysis and X-Ray Absorption Spectroscopy. *J. Phys. Chem. B* **2005**, *109* (6), 2307–2314.

(23) Krauß, K.; Drochner, A.; Fehlings, M.; Kunert, J.; Vogel, H. Oxygen Exchange at Mo/V Mixed Oxides: A Transient and 18O Isotope Study under Technical Conditions. *J. Mol. Catal. A Chem.* **2002**, *177* (2), 237–245.

(24) Drochner, A.; Kampe, P.; Kunert, J.; Ott, J.; Vogel, H. Steady State Isotopic Transient Kinetic Analysis of the Acrolein Oxidation on Mo-V-W-Mixed Oxide Catalysts. In *Applied Catalysis A: General*; 2005; Vol. 289, pp 74–83.

(25) Chen, B.; Goodwin, J. G. Isotopic Transient Kinetic Analysis of Ethane Hydrogenolysis on Cu Modified Ru/SiO2. *J. Catal.* **1996**, *158* (1), 228–235.

(26) Kim, S. Y.; Lohitharn, N.; Goodwin, J. G.; Olindo, R.; Pinna, F.; Canton, P. The Effect of Al2O3-Promotion of Sulfated Zirconia on n-Butane Isomerization: An Isotopic Transient Kinetic Analysis. *Catal. Commun.* **2006**, *7* (4), 209–213.

(27) Kim, S. Y.; Goodwin, J. G.; Hammache, S.; Auroux, A.; Galloway, D. The Impact of Pt and H2 on N-Butane Isomerization over Sulfated Zirconia: Changes in Intermediates Coverage and Reactivity. *J. Catal.* **2001**, *201* (1), 1–12.

(28) Hanspal, S.; Young, Z. D.; Shou, H.; Davis, R. J. Multiproduct Steady-State Isotopic Transient Kinetic Analysis of the Ethanol Coupling Reaction over Hydroxyapatite and Magnesia. *ACS Catal.* **2015**, *5* (3), 1737–1746.

(29) Vada, S.; Chen, B.; Goodwin, J. G. Isotopic Transient Study of La Promotion of Co/Al2O3or CO Hydrogenation. *J. Catal.* **1995**, *153* (2), 224–231.

(30) Shou, H.; Davis, R. J. Multi-Product Steady-State Isotopic Transient Kinetic Analysis of CO Hydrogenation over Supported Molybdenum Carbide. *J. Catal.* **2013**, *306*, 91–99.

(31) Gao, J.; Mo, X.; Goodwin, J. G. Relationships between Oxygenate and Hydrocarbon Formation during CO Hydrogenation on Rh/SiO2: Use of Multiproduct SSITKA. *J. Catal.* **2010**, *275* (2), 211–217.

(32) Ali, S. H.; Goodwin, J. G. SSITKA Investigation of Palladium Precursor and Support Effects on CO Hydrogenation over Supported Pd Catalysts. *J. Catal.* **1998**, *176* (1), 3–13.

(33) Shannon, S. L.; Goodwin, J. G. Characterization of Catalytic Surfaces by Isotopic-Transient Kinetics during Steady-State Reaction. *Chem. Rev.* **1995**, *95*, 677–695.

(34) Spiewak, B. E.; Shen, J.; Dumesic, J. A. Microcalorimetric Studies of CO and H2 Adsorption on Nickel Powders Promoted with Potassium and Cesium. *J. Phys. Chem.* **1995**, *99* (49), 17640–17644.

(35) Ali, S. H.; Goodwin, J. G. SSITKA Investigation of Palladium Precursor and Support Effects on CO Hydrogenation over Supported Pd Catalysts. *J. Catal.* **1998**, *176* (1), 3–13.

(36) Kammert, J. D.; Xie, J.; Godfrey, I. J.; Unocic, R. R.; Stavitski, E.; Attenkofer, K.; Sankar, G.; Davis, R. J. Reduction of Propionic Acid over a Pd-Promoted ReOx/SiO2 Catalyst Probed by X-Ray Absorption Spectroscopy and Transient Kinetic Analysis. *ACS Sustain. Chem. Eng.* **2018**, *6* (9), 12353–12366.

(37) Kresse, G.; Furthmüller, J. Efficient Iterative Schemes for Ab Initio Total-Energy Calculations Using a Plane-Wave Basis Set. *Phys. Rev. B - Condens. Matter Mater. Phys.* **1996**, *54*, 11169–11186.

(38) Kresse, G.; Furthmüller, J. Efficiency of Ab-Initio Total Energy Calculations for Metals and Semiconductors Using a Plane-Wave Basis Set. *Comput. Mater. Sci.* **1996**, *6*, 15–50.

(39) Grimme, S. Semiempirical GCA-Type Density Functional Constructed with a Long-Range Dispersion Correction. *J. Comput. Chem.* **2006**, *27*, 1787–1799.

(40) Kerber, T.; Sierka, M.; Sauer, J. Application of Semiempirical Long-Range Dispersion Corrections to Periodic Systems in Density Functional Theory. *J. Comput. Chem.* **2008**, *29*, 2088–2097.

(41) Masel, R. I. *Principles of Adsorpion and Reaction on Solid Surfaces*; Wiley, 1996.

(42) Dumesic, J. A.; Rudd, D. F.; Aparicio, L. M.; Rekoske, J. E.; Treviño, A. A. *The Microkinetics of Heterogeneous Catalysis*; American Chemical Society, 1993.

Chapter 6. Research Summary and Future Work

6.1 Dissertation Summary

The work presented in this dissertation explored the use of characterization and kinetic studies to evaluate the physical and chemical properties responsible for the performance of heterogeneous catalysts used in a variety of reactive systems. Understanding the effects of physical and chemical properties on a catalyst's reactivity allows for the rational design of catalytic materials that builds from fundamental knowledge and leads to improved performance in real-world applications.

To this purpose, metal oxide supported catalysts composed primarily of noble metals were synthesized by impregnation, ion exchange, controlled surface reactions and atomic layer deposition for use in coupling, hydrogenation, and syngas conversion reactions. Catalysts were characterized using a variety of common and specialized techniques. Physisorption and chemisorption methods were used to evaluate catalyst surface area, support acidity, as well as active metal site densities and dispersion. Infrared spectroscopy of adsorbed molecules was used to explore the geometric and electronic configurations of the metal species. Electron microscopy was used to evaluate particle size distribution of the metal components and, along with energy dispersive x-ray spectroscopy, the uniformity of multi-metallic catalysts. The latter property was further studied via x-ray absorption spectroscopy, where oxidation states and local coordination environment of the bulk metal species were investigated following various pretreatment conditions. Finally, transient kinetic techniques were used to explore the effects of surface coverage on catalytic surfaces.

In Chapter 2, zeolite-supported platinum and platinum-tin catalysts were studied for the non-oxidative coupling of methane. Pt-Sn/ZSM-5 catalysts demonstrated 4x to 15x higher turnover frequencies for ethylene production than both Pt/ZSM-5 and their mono- and bimetallic SiO_2-supported counterparts. Bimetallic zeolite-supported catalysts have also been shown to have higher selectivity to ethylene and aromatics, particularly benzene, as well as improved resistance to coke formation when compared to the monometallic materials. The effects of support acidity on the catalytic activity were evaluated by varying the SiO_2/Al_2O_3 ratio of the support between 23 and 280, with higher ratios corresponding to lower acidity levels. It was expected that increasing the acidity of the zeolite support would create a bifunctional material in which methane activation and ethylene formation take place on metal sites, followed by ethylene oligomerization to aromatics on acidic support sites. The highest activity towards the production of aromatics, specifically benzene and naphthalene, was obtained over catalysts with SiO_2/Al_2O_3 ratios of 23 and 50, with maximum aromatic formation rates achieved after 15 h and 20 h TOS, respectively. Expectedly, the more acidic catalysts were also prone to higher coke deposition. These catalysts also demonstrated a volcano-shaped activity profile, suggesting the presence of a hydrocarbon pool on the acidic support surface to promote aromatic formation, followed by catalyst deactivation once the maximum formation of ethylene was achieved. Additionally, our best performing Pt-Sn/ZSM-5 catalyst ($SiO_2/Al_2O_3 = 50$) was found to be catalytically comparable to the state-of-the-art Mo/ZSM-5 catalyst under the same reaction conditions.

In Chapter 3, x-ray absorption spectroscopy was used to evaluate the chemical and structural environment of supported multi-metallic catalysts prepared using specialized synthesis techniques. Bimetallic palladium catalysts were synthesized by selective deposition of the Pd species on Ag, Cu, and Au parent catalysts via controlled surface reactions and used in amination, hydrodechlorination, and hydrogenation reactions. XAS studies on AuPd catalysts for the direct amination of 1-hexanol showed that bimetallic homogeneity was achieved in these catalysts, with Pd being well-dispersed on the Au parent surface, as corroborated by CO-FTIR. This homogeneity was partially responsible for the improvements in catalytic activity observed over monometallic catalysts due to electronic and ensemble effects from the Au-Pd alloy. Studies for AgPd catalysts in the hydrodechlorination of 1,2-dicholorethane demonstrated the importance of catalyst support on the extent of bimetallic particle formation. Carbon-supported catalysts were found to have the highest degree of metal segregation between Ag and Pd species, while the homogeneity in SiO_2- and TiO_2- supported materials was not only improved when compared to carbon supported catalysts, but also dependent on the Pd loading. Lower Pd loadings on $AgPd/TiO_2$ catalysts were found to have higher Pd dispersion, and these catalysts were shown to have the highest selectivity to ethylene under reaction conditions when compared to SiO_2- or carbon-supported materials. Similarly, the structure of AgPd and CuPd catalysts used in the selective hydrogenation of acetylene was also found to be dependent on the support used. In this case, the effect of various pretreatment conditions was explored over SiO_2- and TiO_2-supported catalysts, and a significant increase in Pd-Pd coordination was observed for $AgPd/TiO_2$ and $CuPd/TiO_2$ catalysts following a hydrogen reduction or an exposure to the feed mixture at reaction conditions. In contrast, SiO_2-supported materials did not show significant changes in the structural environment following pretreatment for either bimetallic system and were found to be less selective to ethylene generation than their TiO_2 counterparts. Finally, Mo-containing multi-metallic catalysts synthesized via atomic layer deposition and used in the conversion of synthesis gas to higher alcohols were studied using XANES analyses. In combination with temperature-programmed reduction and isotopic H_2-

D_2 experiments, XANES results provided evidence for the existence of hydrogen spillover with the addition of reducible metals onto MoO_x/SiO_2 catalysts.

In Chapter 4, H-ZSM-5, SiO_2-, and Al_2O_3-supported platinum catalysts were used to investigate the effects of catalyst support and pretreatment conditions on acetone hydrogenation. ZSM-5-supported catalysts were found to be 2-3 orders of magnitude more active than the SiO_2- and Al_2O_3-supported catalysts, regardless of calcination or reduction temperature. Higher temperature calcinations followed by lower temperature reductions generally led to Pt/ZSM-5 catalysts with higher activity than those pretreated under lower calcination and higher reduction temperature, likely as a result of morphological changes induced by the surface mobility of platinum under O_2 and H_2 environments. While no significant direct effects from zeolite support acidity on the catalytic activity were observed, a shift to higher frequencies in the Pt-CO band of Pt/ZSM-5 catalysts observed via CO-FTIR suggests that the enhanced catalytic activity observed over these catalysts compared to Pt/SiO_2 could be due to the interaction of Pt species with the three-dimensional structure of the zeolite support. Specifically, the presence of Pt species within the zeolite pores could stabilize the metal particles, making them more resistant to morphological changes following variations in pretreatment, and enhance catalytic activity for acetone hydrogenation due to confinement effects.

In Chapter 5, transient reaction kinetic experiments and microkinetic modeling were combined to probe the importance of surface coverage effects on the catalytic activity of acetone hydrogenation over a platinum catalyst at 350 K. Transient response models based on a steady-state microkinetic analysis of acetone hydrogenation on platinum predicted minimal changes in the surface coverage of the most abundant reactive intermediate (MARI) upon removal of acetone from the reactant feed when the coverage effects dynamically accounted for neighbor-neighbor interactions in energetic parameters via the Bragg-Williams approximation. In contrast, predictions for transients following a substitution of the reactant acetone species with another ketone (e.g., pentanone), as in the case of traditional SSITKA studies, showed that full removal of the MARI from the catalyst surface can be achieved at 350 K. Static coverage dependence models using typical Langmuir isotherms differed from the Bragg-Williams models by predicting full MARI removal from the catalytic surface following both removal and substitution of acetone from the reactant feed. Quantitative analysis of the experimental transient responses highlighted the importance of coverage effects on surface reactivity for this system and the need for dynamic coverage dependence in the microkinetic modeling of acetone hydrogenation over platinum.

6.2 Future Work

Recent work within our group has been focused on the use of transient techniques for the fundamental characterization of heterogeneous catalysts. These techniques can be used to provide further understanding of the intricacies of complex catalytic surfaces used in a variety of reactive systems for which standard characterization techniques are insufficient to explain steady-state kinetic and reactivity trends. Additionally, transient techniques can be used to help elucidate surface reaction mechanisms for systems in which steady-state experiments might not provide the clarity needed.

The ethylene hydrogenation reaction has been extensively studied throughout the years, but its mechanism continues to be a source of debate. It is generally accepted that the reaction follows a Horiuti-Polanyi-type mechanism, in which ethylene adsorbs either in a π- or di-σ configuration and reacts with disassociated surface hydrogen to form an adsorbed ethyl intermediate prior to undergoing a second hydrogenation step to form the alkane.[1,2] However, the inherent nature of the mechanism, specifically of the active site involved, has not been well-defined. Findings throughout the literature suggest that various adsorption models are capable of fitting experimentally obtained kinetic parameters, and these models tend to revolve around the following concepts: (1) competitive adsorption of hydrogen and ethylene, (2) dual-site hydrogen adsorption, where only one site undergoes competitive adsorption with ethylene, and (3) non-competitive adsorption, where hydrogen and ethylene each reversibly adsorb onto independent sites and the reaction occurs at the site boundaries.[3,4]

Additionally, the vast majority of available theoretical data and kinetic models in literature do not account for the interactions of neighboring species on the catalytic surface, thus neglecting the effects of surface coverage on energetics and overall kinetics. Various studies have employed theoretical and experimental approaches in an attempt to introduce coverage dependencies onto kinetic and equilibrium properties. Neurock and coworkers have shown using DFT and Monte Carlo simulations that repulsive interactions weaken the Pd-C and Pd-H bonds and lower hydrogenation barriers at higher surface coverages, which accurately described known experimental results.[2,5] Grönbeck and coworkers have used density functional theory calculations to investigate the hydrogenation of ethylene over palladium nanoclusters in comparison to single crystal surfaces, and found that the higher surface coverages achieved over clusters lead to changes in the preferred adsorption mode of ethylene.[6] Rosch and coworkers investigated the effects of surface coverage between 1/9-1/3 of a monolayer for the conversion of ethylene to an ethylidyne intermediate over Pd (111), and found that the dehydrogenation of ethylene to vinyl was the rate limiting step at all coverages.[7] Work by Tysoe and coworkers has demonstrated the effects of lateral interactions on the kinetic and reactive properties of ethylene over a Pd(111) surface using temperature-programmed desorption (TPD) and reflection absorption infrared spectroscopy (RAIRS) techniques.[8,9] The group found that as the coverage of ethylene increased, the lateral interactions between ethylene molecules led to lower heats of adsorption, which manifested in significant ethylene desorption rates at low temperatures.

In an effort to further elucidate the effects of surface coverage on the ethylene hydrogenation mechanism, preliminary work using transient techniques has been conducted over palladium catalysts at 313 K. Similar to the transient work discussed in Chapter 5 for acetone hydrogenation, the transient profiles of the ethylene and ethane species have been collected via a set of experiments that either removed or substituted the ethylene reactant from the feed stream. As shown in Figure 6.1, the desorption profile for ethane, induced by the removal of ethylene from the feed, appears to show two distinct features throughout the duration of its decay. Interestingly, this behavior was not observed during the reactive transient that followed the substitution of ethylene in the feed with propylene, a similarly structured alkene. From the desorption trend observed, it can be hypothesized that there might be two possible sources of surface species conducive to the formation and desorption of ethane from the palladium surface.

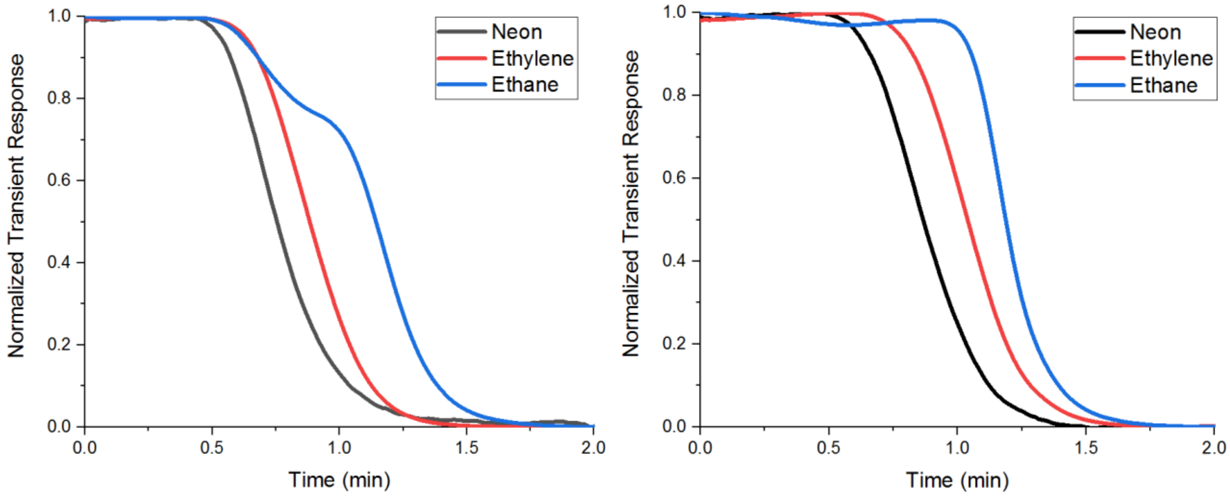

Figure 6.1. Transient response profiles for a neon tracer (black), ethylene (red), and ethane (blue) following the removal (left panel) or substitution (right panel) of ethylene in the feed stream.

Numerous studies have been performed to evaluate the surface reaction mechanism of the ethylene hydrogenation reaction, specifically in an attempt to elucidate the reactive intermediates.

Ethyl, vinyl, ethylidene, and vinylidene species have all been proposed as potential surface intermediates in the formation of ethylidyne from di-σ-bonded ethylene.[10–14] Infrared spectroscopy has been previously used over the Pd catalysts discussed above to demonstrate the adsorption of ethylene bonded primarily in a di-σ configuration over monometallic palladium catalysts. In-situ FTIR has also been used to evaluate the adsorbed surface species that might be present during the selective hydrogenation of acetylene in ethylene-rich streams over these palladium catalysts. A similar approach could be used to evaluate reaction intermediates on the catalytic palladium surface following exposure to an ethylene/hydrogen feed mixture at reaction conditions. Additionally, in-situ IR studies in which a transient is induced by the removal or substitution of the ethylene feed could be used to monitor the time-dependent evolution of surface species conducive to the formation and desorption of ethane.[3] These IR studies, combined with the transient kinetics technique, could be used to experimentally elucidate the hydrogenation mechanism over palladium catalysts. Furthermore, this type of analysis could be expanded to other catalytic materials, including bimetallic Pd-based catalysts, through which the effects of dopant metal or catalyst support on the reaction mechanism and hydrogenation kinetics could be explored.

Moreover, the hydrogenation of ethylene to ethane is known to take place at high surface coverages of intermediate species on the catalytic surface. Theoretical and microkinetic modeling of the ethylene hydrogenation system has traditionally been performed using Langmuir-type adsorption kinetic profiles, which neglect nearest neighbor interactions. Similar to the work we have performed for the acetone hydrogenation system, it could be beneficial to pursue the development of a theoretical model that could be used for both steady-state and transient work and accounts for the effects of those neighbor-neighbor interactions on surface energetics, i.e. via the Brag-Williams approximation.

Transient kinetics studies are of great benefit to other reactive systems for which the elucidation of and any differences in reaction mechanisms could be key to the development and functional understanding of catalytic materials. One such reactive system is the Guerbet coupling of ethanol to higher alcohols, for which extensive work has been performed by current and previous researchers within our group and in numerous literature sources. Ongoing work within our group thrives to understand the fundamental causes behind the apparent trade-off observed between alcohol conversion and selectivity towards linear alcohols. Additionally, control over the extent of product branching is being sought after due to its effect on the overall yields of ethers and olefins in the condensation process. Various catalysts, including calcium hydroxyapatite, magnesium oxide, and magnesia alumina, have been and continue to be explored on the quest to identify materials capable of achieving high single-pass alcohol conversions (>40%) with high selectivity (>80%) to linear alcohols while maintaining catalytic stability over extended reaction times. To this effort, transient kinetics studies can be used to elucidate differences in the reaction mechanism over different catalytic materials in an effort to understand the properties that govern reactivity trends observed at steady state.

6.3 References

(1) Davis, M. E.; Davis, R. J. Microkinetic Analysis of Catalytic Reactions. In *Fundamentals of chemical reaction engineering*; Glandt, E. D., Klein, M. T., Edgar, T. F., Eds.; McGraw-Hill Higher Education: New York, NY, 2003; pp 240–259.

(2) Neurock, M.; Hansen, E.; Mei, D.; Venkataraman, P. S. From First-Principles to Catalytic Turnovers: Ethylene Hydrogenation Over Palladium. In *Reaction Kinetics and the Development and Operation of Catalytic Processes*; Froment, G. F., Waugh, K. C., Eds.; Elsevier Science Publishers B.V.: Amsterdam, Netherlands, 2001; pp 19–40.

(3) Rekoske, J. E.; Cortright, R. D.; Goddard, S. A.; Sharma, S. B.; Dumesic, J. A. Microkinetic Analysis of Diverse Experimental Data for Ethylene Hydrogenation on Platinum. *J. Phys. Chem.* **1992**, *96* (4), 1880–1888.

(4) van Santen, R. A.; Neurock, M. The Reactivity of Transition-Metal Surfaces. In *Molecular Heterogeneous Catalysis: A Conceptual and Computational Approach*; Wiley-VCH: Weinheim, 2006; pp 143–155.

(5) Neurock, M.; Pallassana, V.; Van Santen, R. A. The Importance of Transient States at Higher Coverages in Catalytic Reactions. *J. Am. Chem. Soc.* **2000**, *122* (6), 1150–1153.

(6) Posada-Borbón, A.; Heard, C. J.; Grönbeck, H. Cluster Size Effects in Ethylene Hydrogenation over Palladium. *J. Phys. Chem. C* **2017**, *121* (20), 10870–10875.

(7) Moskaleva, L. V; Chen, Z. X.; Aleksandrov, H. A.; Mohammed, A. B.; Sun, Q.; Rösch, N. Ethylene Conversion to Ethylidyne over Pd(111): Revisiting the Mechanism with First-Principles Calculations. *J. Phys. Chem. C* **2009**, *113* (6), 2512–2520.

(8) Molero, H.; Stacchiola, D.; Tysoe, W. T. The Kinetics of Ethylene Hydrogenation Catalyzed by Metallic Palladium. *Catal. Letters* **2005**, *101* (3–4), 145–149.

(9) Burkholder, L.; Stacchiola, D.; Tysoe, W. T. *KINETIC AND REACTIVE PROPERTIES OF ETHYLENE ON CLEAN AND HYDROGEN-COVERED Pd(111)*; 2003; Vol. 10.

(10) Zaera, F.; Ma, Z. Characterization of Heterogeneous Catalysts. In *Surface and Nanomolecular Catalysis*; Richards, R. M., Ed.; Taylor & Francis (CRC Press), 2006; pp 1–38.

(11) Mcmahon, T. B.; Heinis, T.; Nicol, G.; Hovey, J. K.; Kebarle, P. *The Surface Chemistry of Vinyl Iodide on Pt(l 11)*; 1992; Vol. 114.

(12) Cremer, P.; Stanners, C.; Niemantsverdriet, J. W.; Shen, Y. R.; Somorjai, G. The Conversion of Di-σ Bonded Ethylene to Ethylidyne on Pt(111) Monitored with Sum Frequency Generation: Evidence for an Ethylidene (or Ethyl) Intermediate. *Surf. Sci.* **1995**, *328* (1–2), 111–118.

(13) Windham, R. G.; Koel, B. E. Coadsorptlon of Ethylene and Potassium on Pt(111). 2. Influence of Potassium on the Decomposition of Ethylene. *J. Phys. Chem.* **1990**, *94* (4), 1489–1496.

(14) Carter, E. A.; Koel, B. E. A Method for Estimating Surface Reaction Energetics:

Application to the Mechanism of Ethylene Decomposition on Pt(111). *Surf. Sci.* **1990**, *226* (3), 339–357.